LA--10338-T

DE85 010355

LA-10338-T
Thesis

UC-34C
Issued: February 1985

The Measurement of Pion Double Charge Exchange on Carbon-13, Carbon-14, Magnesium-26, and Iron-56

Peter Anthony Seidl *

*Department of Physics, University of Texas at Austin, Austin, TX 78712.

Los Alamos Los Alamos National Laboratory
Los Alamos, New Mexico 87545

TABLE OF CONTENTS

LIST OF TABLES

LIST OF FIGURES

THE MEASUREMENT OF PION DOUBLE CHARGE EXCHANGE ON CARBON-13, CARBON-14, MAGNESIUM-26 AND IRON-56

by

Peter Anthony Seidl

ABSTRACT

Cross sections for the $^{13,14}C,^{26}Mg,^{56}Fe(\pi^+,\pi^-)^{13,14}O,^{26}Si,^{56}Ni$ reactions were measured with the Energetic Pion Channel and Spectrometer at the Clinton P. Anderson Meson Physics Facility for $120 \leq T_\pi \leq 292$ MeV and $0 \leq \theta \leq 50$. The double isobaric analog states (DIAS) are of primary interest. In addition, cross sections for transitions to $^{14}O(0^+, 5.92$ MeV), $^{14}O(2^+, 7.77$ MeV), $^{56}Ni(gs)$, $^{13}O(gs)$, and $^{13}O(4.21$ MeV) are presented. The $^{13}O(4.21$ MeV) state is postulated to have $J^\pi = 1/2^-$. The data are compared to previously measured double-charge-exchange cross sections on other nuclei, and the systematics of double charge exchange on $T > 1$ target nuclei leading to the DIAS are studied. Near the Δ_{33} resonance, cross sections for the DIAS transitions are in disagreement with calculations in which the reaction is treated as sequential charge exchange through the free pion-nucleon amplitude, while for $T_\pi > 200$ MeV the anomalous features of the 164 MeV data are not apparent. This is evidence for significant higher order contributions to the double-charge-exchange amplitude near the resonance energy. Two theoretical approaches that include two nucleon processes are applied to the DIAS data.

I. INTRODUCTION

Pion charge-exchange reactions leading to isobaric analog states (IAS) provide an attractive method for studying the meson-nucleus interaction and nuclear structure. The fact that isospin is conserved leads to the expectation that the initial and final nuclear states should be closely related -- a relatively simple nuclear situation.

In pion single charge exchange (SCX) leading to the IAS, only one hard interaction is necessary to cause the transition. Thus, the distorted-wave impulse approximation (DWIA) is expected to describe angular-distribution and excitation-function (differential cross section versus pion kinetic energy) data. This expectation is reasonably well founded, the DWIA has been successful in describing many strong inelastic transitions observed in π-nucleus scattering experiments throughout the periodic table [Mo-83]. Thus, the hoped for simplicity of the SCX amplitude, along with the expected sensitivity to neutron density differences motivated early interest in the SCX reaction.

The (π^+,π^-) reaction involves changing two neutrons into protons. Thus, in leading order, the reaction involves two hard interactions. Within the multiple-scattering formalism, this means that the first double-charge-exchange (DCX) term is the product of

two off-diagonal matrix elements, which has led to the expectation that DCX would be sensitive to nucleon correlation effects that might not be apparent in transitions tractable in the lowest order DWIA. In a DCX reaction leading to the double isobaric analog state (DIAS) the coupling to (at least) the intermediate analog state must be present in any lowest order calculation. Consequently, important assumptions must be made about the intermediate states, as well as the propagation of the intermediate π^0 in the nuclear medium. As in the (π^+,π^0) reaction, (π^+,π^-) is also expected to be sensitive to the excess neutron density. Experimental and subsequent theoretical work have shown that large contributions to DCX (and SCX) appear to arise from nuclear structure and two nucleon processes. The exact nature of the latter are as yet uncertain, but some candidates are pion absorption [Li-83], nucleon correlations, Δ_{33}-nucleus interactions [Jo-84], and virtual Δ_{33} components of the nuclear wave function. However, it may be necessary to explain some of the data with the theory of quarks and gluons. Within a quark picture, (π^+,π^-) occurs by changing two down quarks into two up quarks. If two nucleons overlap sufficiently in the nucleus, such an approach, if tractable, would have the attractive feature of using the nucleus to study extended quark systems [Le-84, Mi-84].

The enhancement of SCX cross sections in the Δ_{33}-resonance (J=3/2, T=3/2, E=1232 MeV) region was first observed in experiments which measured the radioactivity of the residual nuclei [Ch-69]. In the past four years SCX cross sections have been measured for transitions to the IAS with high accuracy using the π^0 Spectrometer at

LAMPF [Ba-80,Do-82,Sen-83,Ir-83]. DWIA calculations significantly underestimate the forward angle cross sections for $T \lesssim 200$ MeV, but experiments have confirmed the expectation that $\sigma(\theta) \propto J_0^2(\theta)$. The target mass dependence of $\sigma(0^o)$ varies as a function of energy -- is smoothest for $T \gtrsim 230$ MeV, and deviates most from the power law $A^{-\alpha(E)}$ at 165 and 100 MeV. The puzzling energy dependence of the cross sections has stimulated continued experimental and theoretical work.

The earliest measurements of the small-angle excitation function of (π^+,π^-) double-charge-exchange (DCX) reactions -- reported for the $T = 1$ target nuclei ^{18}O [Bu-78, Gr-79] and ^{26}Mg [Gr-82a] leading to the double-isobaric-analog states (DIAS) $^{18}Ne(gs)$ and $^{26}Si(gs)$ -- exhibit a rapidly varying cross section as a function of pion energy (see Fig. I-1). The energy dependence is that of a peak 60-80 MeV wide centered near 140 MeV and a monotonic increase of the cross section between 200 and 300 MeV. At $T_\pi = 292$ MeV, angular distributions [Gr-82a] for $^{18}O(\pi^+,\pi^-)^{18}Ne(DIAS)$ and $^{26}Mg(\pi^+,\pi^-)^{26}Si(DIAS)$ exhibit diffractive shapes with first minima at momentum transfers that agree with simple DCX models that describe the reaction as sequential charge exchange through the free π-A amplitude. However, at $T_\pi = 164$ MeV the $^{18}O(\pi^+,\pi^-)^{18}Ne(DIAS)$ angular distribution has a minimum at $\theta = 20^o$, which corresponds to an unrealistically large radius within the simpler models (see Eq. I-6). The occurrence of a minimum at a small scattering angle is not explained by any simple [Jo-80,Mi-81] two-step pion-nucleus calculation. Prior to the present work, there was no $T_\pi = 164$ MeV angular distribution for $^{26}Mg(\pi^+,\pi^-)^{26}Si(DIAS)$.

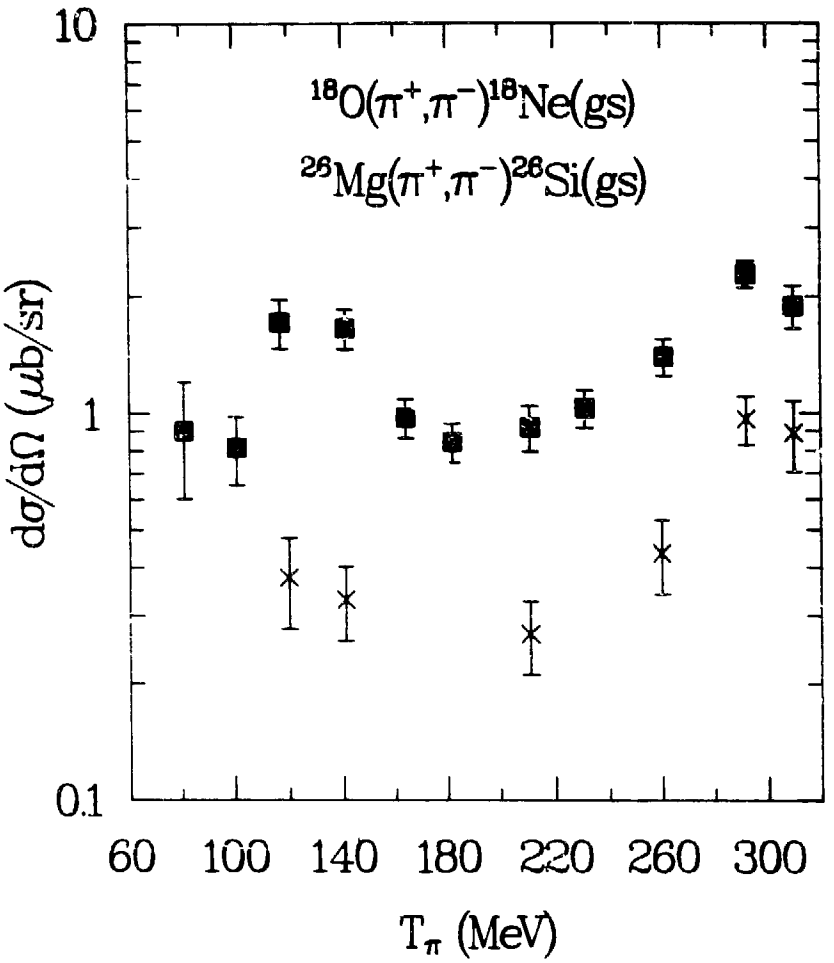

Fig. I-1: Excitation functions measured at $\theta_{lab} = 5^o$ for $^{18}O(\pi^+,\pi^-)^{18}Ne(DIAS)$ (squares), and $^{26}Mg(\pi^+,\pi^-)^{26}Si(DIAS)$ (crosses) from [Gr-82a].

Experimental data have shown the dependence of the forward-angle cross section on target mass to be roughly $A^{-10/3}$ [Mo-80], in agreement with the geometric model of Johnson [Jo-80]. For A = 18, the cross section at $\theta_{lab} = 5^{o}$ and at energies near the peak of the Δ_{33} resonance is about one μb/sr.

In contrast, DCX on T = 0 nuclei (which, of necessity, must be non-analog in character) leading to the ground state of the residual nucleus have exhibited peaked excitation functions with a centroid and width of about 160 MeV and 70 MeV, respectively [Bl-83]. The forward-angle cross section is about 0.5 μb/sr for A = 16 near the maximum of the excitation function and the target mass dependence [Mo-82a] is roughly $A^{-4/3}$. The shapes of the angular distributions are well described by the eikonal expression, $\sigma \propto J_0^2(qR)$, where q is the momentum transfer and R is the strong absorption radius [Bl-83, Gi-84a].

A phenomenological two-amplitude model has been applied to the $^{18}O(\pi^+,\pi^-)^{18}Ne(gs)$ excitation function [Gr-82b], and 164-MeV angular distribution [Gi-84b]. A nonanalog amplitude was inferred from the $^{16}O(\pi^+,\pi^-)^{16}Ne(gs)$ data, and was added to a calculated amplitude that described the ^{18}O reaction as sequential charge exchange through the intermediate analog state. The free parameter was an energy dependent phase between the two amplitudes.

Some features of analog SCX and DCX can be understood by inspecting the SCX amplitude. The lowest order DWIA result for (π^+,π^0) is [Ei-80]

$$\langle \pi^0; a|T|\pi^+; 0\rangle =$$

$$\int \chi_k^{(-)*}(\vec{r})\langle a|\sum_{i=1}^{A}(f_o + f_1\vec{\phi}\cdot\vec{\tau})\delta(\vec{r}-\vec{r}_i)|0\rangle\phi_k^{(+)}(\vec{r})d^3r. \qquad \text{(I-1)}$$

The sum over $(f_o + f_1\vec{\phi}\cdot\vec{\tau})$, the pion-nucleon amplitude, is over all (A) nucleons. $\vec{\phi}$ is the pion isospin operator, and $\vec{\tau}$ is the nucleon isospin operator. $\langle a|$ and $|0\rangle$ are the final (IAS) and initial nuclear states and $\chi_k^{(-)}(\vec{r})$ and $\phi_k^{(+)}(\vec{r})$ are the outgoing and incoming waves for the π^0 and π^+, respectively. The analog of the ground state is obtained by an isospin raising operation,

$$T_+|T,T_z\rangle = \sqrt{2T_z}|T,T_z+1\rangle = \sqrt{N-Z}|T,T_z+1\rangle.$$

so,

$$|a\rangle = \frac{1}{\sqrt{N-Z}}T_+|0\rangle = \frac{1}{\sqrt{N-Z}}\cdot\frac{1}{2}\cdot\sum_{j=1}^{A}(\tau_x + i\tau_y)_j|0\rangle, \qquad \text{(I-2)}$$

where the nucleon isospin raising operator has been written in terms of the Pauli isospin matrices, τ_i, with the convention that $\tau_z|p\rangle = |p\rangle$. Only the isovector part of the π-A amplitude connects the ground state of the target and the IAS. The $\vec{\phi}\cdot\vec{\tau}$ term of the π-A amplitude may be rewritten in terms of the Pauli matrices.

$$\langle \pi^0|\vec{\phi}\cdot\vec{\tau}|\pi^+\rangle = \langle \pi^0|(\phi_+\tau_- + \phi_-\tau_+ + 2\phi_z\tau_z)|\pi^+\rangle,$$

$$= \langle \pi^0|\sqrt{2}\tau_+|\pi^0\rangle = \langle \pi^0|\pi^0\rangle\sqrt{2}\tau_+$$

$$= \frac{\sqrt{2}}{2}(\tau_x + i\tau_y). \qquad \text{(I-3)}$$

Using this we can evaluate

$$\langle a|\frac{\sqrt{2}}{2}\sum_{i=1}^{A}(\tau_x + i\tau_y)_i\delta(\vec{r}-\vec{r}_i)|0\rangle$$

$$= \frac{\sqrt{2}}{2\sqrt{N-Z}}\langle 0|\sum_{ij}^{A}(\tau_x - i\tau_y)_j(\tau_x + i\tau_y)_i\delta(\vec{r}-\vec{r}_i)|0\rangle,$$

$$= \frac{\sqrt{2}}{4\sqrt{N-Z}}\langle 0|\sum_{ij}^{A}(\tau_-)_j(\tau_+)_i\delta(\vec{r}-\vec{r}_i)|0\rangle,$$

$$= \frac{1}{4}\frac{\sqrt{2}}{\sqrt{N-Z}}\langle 0|\sum_{ij}^{A}[(\tau_-)_j,(\tau_+)_i]\delta(\vec{r}-\vec{r}_i)|0\rangle,$$

$$= -\frac{\sqrt{2}}{\sqrt{N-Z}}\langle 0|\sum_{i=1}^{A}(\tau_z)_i\delta(\vec{r}-\vec{r}_i)|0\rangle. \qquad \text{(I-4)}$$

We have made use of $[(\tau_-)_j,(\tau_+)_i] = 0$ (for $i\neq j$), and $[(\tau_-)_i,(\tau_+)_i] = 4(\tau_z)_i$. For i=1,

$$\langle 0|(\tau_z)_1\delta(\vec{r}-\vec{r}_1)|0\rangle$$

$$= \int\psi_A^*(\vec{r}_1,\ldots,\vec{r}_A)\cdot(+1)\cdot\psi_A(\vec{r}_1,\ldots,\vec{r}_A)\delta(\vec{r}-\vec{r}_1)d^3r_1d^3r_2\ldots d^3r_A$$

$$= \int d^3r\delta(\vec{r}-\vec{r}_1)\phi_{p1}^*(\vec{r}_1)\phi_{p1}(\vec{r}_1) = \rho_{p1}(\vec{r}),$$

where ψ_A is the wave function for the A nucleons and ϕ_{p1} is the wave function for proton #1. Evaluating the rest of the terms in the sum of (I-4) is straightforward. Thus,

$$\langle a|\frac{\sqrt{2}}{2}\sum_{i=1}^{A}(\tau_x + i\tau_y)_i\delta(\vec{r}-\vec{r}_i)|0\rangle =$$

$$\frac{\sqrt{2}}{\sqrt{N-Z}}(\rho_{p1}(\vec{r}) + \rho_{p2}(\vec{r}) + \ldots + \rho_{pZ}(\vec{r})$$

$$- \rho_{n_1}(\vec{r}) - \rho_{n_2}(\vec{r}) - \ldots - \rho_{nN}(\vec{r})]$$

$$= \frac{\sqrt{2}}{\sqrt{N-Z}}(N\rho_n(\vec{r}) - Z\rho_p(\vec{r})). \qquad \text{(I-5)}$$

where $\rho_n(\vec{r}) = \rho_{n_1}(\vec{r}) + \rho_{n_2}(\vec{r}) + \ldots + \rho_{nN}(\vec{r})$,

and $\rho_p(\vec{r}) = \rho_{p_1}(\vec{r}) + \rho_{p_2}(\vec{r}) + \ldots + \rho_{pZ}(\vec{r})$.

The normalization of the densities is

$$\int d^3r\rho_n(\vec{r}) = \int d^3r\rho_p(\vec{r}) = 1.$$

Inserting (I-5) into (I-1) gives the result

$$\langle \pi^0; a|T|\pi^+; 0\rangle = \sqrt{2}f_1 \int \chi_k^{(-)*}(\vec{r})\frac{1}{\sqrt{N-Z}}(N\rho_n(\vec{r}) - Z\rho_p(\vec{r}))\psi_k^{(+)}(\vec{r})d^3r.$$

This lowest order result shows the sensitivity of SCX to neutron-proton density differences. The SCX cross-sections are proportional to (N - Z), and applying the isospin-raising operator twice to the target-nucleus wave function shows the N and Z dependence of DCX leading to the DIAS.

$$T_+T_+|T,T_z\rangle = \sqrt{N - Z}T_+|T,T_z+1\rangle$$

$$= \sqrt{2(N - Z)(N - Z - 1)}|T,T_z+2\rangle.$$

Thus, neglecting nuclear structure differences between nuclei, we expect $\sigma_{DCX} \propto (N - Z)(N - Z - 1)$, for transitions to the DIAS.

Assuming that the dominant intermediate state is the IAS of the target nucleus, (which is perhaps only true for $T_\pi > 230$ MeV) the transition amplitude for DCX is

$$\langle \pi^-;a|T|\pi^+;0\rangle =$$

$$\int \chi_k^{(-)*}(\vec{r})\langle b|\sum_{i=1}^{A}(f_1\vec{\phi}\cdot\vec{\tau})\delta(\vec{r}-\vec{r}_i)|a\rangle\chi_k^{(+)}(\vec{r})G(\vec{r}-\vec{r}')\times$$

$$\chi_\kappa^{(-)*}(\vec{r}')\langle a|\sum_{j\neq i}^{A}(f_1\vec{\phi}\cdot\vec{\tau})\delta(\vec{r}'-\vec{r}_j)|0\rangle\psi_k^{(+)}(\vec{r})d^3r'd^3r.$$

$G(\vec{r}-\vec{r}')$ describes the propagation of the intermediate π^0 through the nucleus. The failure of such an amplitude to describe data means that some, or all, of the assumptions concerning nuclear structure, intermediate states, medium effects, or reaction mechanism, are wrong.

Johnson [Jo-80] has calculated analytic expressions for analog SCX and DCX for $\sigma(\theta)$ in the eikonal approximation, assuming isospin invariance. In this geometrical model, the SCX cross section is shown to be proportional to $(\Delta\rho(R)/\rho(R))^2$, while the DCX cross section to $(\Delta\rho(R)/\rho(R))^4$, where R is defined by $\rho(R)/\rho(0) \approx 0.1\text{-}0.2$, and $\Delta\rho$ is the neutron proton density difference, or the density of the excess neutrons. DCX is assumed to proceed in two steps via a matrix element proportional to A^{-1}. Under the assumption that $\Delta\rho(R)/\rho(R) \propto (N - Z)/A$, then

$$\sigma_{SCX} \propto (N - Z)A^{-4/3}, \text{ and}$$

$$\sigma_{DCX} \propto (N - Z)(N - Z - 1)A^{-10/3}.$$

The shapes of the angular distributions are predicted to be given by cylindrical Bessel functions.

$$\sigma_{SCX}(\theta) \propto J_0^2(qR),$$

$$\sigma_{DCX}(\theta) \propto \left(\left(1 - \frac{a}{R}\right)J_0(qR) + aqJ_1(q\bar{R})\right)^2, \qquad \text{(I-6)}$$

where q is the momentum transfer in fm^{-1} and a is the nuclear surface diffuseness parameter.

Almost all theoretical DCX work has concentrated on analog trans tions [Li-83,Jo-83b]. Liu [Li-83] uses a coupled-channels optical potential and includes sequential one-nucleon single-charge-exchange (SCX) processes, with terms proportional to ρ^2 in the potential. True pion absorption and scattering of a pion by two short-range correlated nucleons are the reaction mechanisms considered in the calculation of the ρ^2 terms, though the latter process is estimated to be unimportant at energies below T_π = 180 MeV. In [Li-83], calculations are compared to the measured angular distributions and the excitation function for $^{18}O(\pi^+,\pi^-)^{18}Ne$(DIAS). For these calculations, the effects of core excitation were found to be important. An application of this theory to the $^{14}C(\pi^+,\pi^-)^{14}O$(DIAS) data reported here is presented in Chapter V.

The theoretical work of Johnson and Siciliano [Jo-83a,b] is also based on a coupled-channels optical potential and includes terms proportional to ρ^2. Their theory is constructed in an isospin invariant framework. The parameters of the first order potential are

determined by the free pion-nucleon phase shifts. The elastic, SCX and DCX amplitudes are obtained by taking linear combinations of the pion-nucleus scattering amplitudes in channels of total isospin (nuclear plus pion). The coulomb interaction is not included in their theory. Their second-order potential is constructed with the purpose of obtaining a set of phenomenological parameters to describe elastic scattering, SCX and DCX reactions from a given nucleus at a given energy. Most of these parameters are weakly dependent on target mass, but are strongly energy dependent. DCX reactions that lead to double isobaric analog states were explored within this isobaric multiplet approach of Johnson and Siciliano [Jo-83b]. A systematic analysis of elastic scattering, single charge exchange and double charge exchange leading to analog states was made [Gr-84], and some of the results of that work are presented in Chapter V. The new $^{14}C(\pi^+,\pi^-)$ measurements reported herein are part of a study of pion elastic scattering [Ha-84], SCX [Ir-83], and DCX reactions on a single T = 1 isotope.

This thesis presents angular distributions for $^{14}C,^{26}Mg(\pi^+,\pi^-)^{14}O,^{26}Si(DIAS)$ at T_π = 164 MeV, $^{14}C(\pi^+,\pi^-)^{14}O(DIAS)$ at T_π = 292 MeV, a 5° excitation function for $^{14}C(\pi^+,\pi^-)^{14}O(DIAS)$ ($120 \leq T_\pi \leq 292$ MeV), $^{56}Fe(\pi^+,\pi^-)^{56}Ni(gs)$, and $^{56}Fe(\pi^+,\pi^-)^{56}Ni(DIAS)$ ($140 \leq T_\pi \leq 292$ MeV), and forward angle (θ_{lab} = 5°) differential cross sections at T_π = 120, 164, 180 MeV for $^{26}Mg(\pi^+,\pi^-)^{26}Mg(DIAS)$.

The DIAS of the ^{56}Fe ground state is not the ground state of ^{56}Ni. Previous measurements of $^{58}Ni(p,t)^{56}Ni$ [Na-74] and $^{54}Fe(^3He,n)^{56}Ni$ [Ev-72] are not in good agreement as to the location of the DIAS in ^{56}Ni, but generally find the state at E_x = 9.9 MeV. As

was demonstrated earlier by Morris et al. [Mo-80], pion induced DCX enables the selective excitation of the DIAS in heavy nuclei even when the state is in a region having a relatively large level density in the residual nucleus. In this (π^+,π^-) measurement, the DIAS (T=2) in ^{56}Ni is seen at E_x = 9.6 ± 0.2 MeV. These ^{14}C and ^{56}Fe data are the first observation of the energy dependence of DIAS and nonanalog $0^+ \rightarrow 0^+$ transitions in the same nucleus. Theoretical efforts to address both DIAS and nonanalog transitions simultaneously will be aided in this case by the absence of entrance channel differences for the two reactions.

In addition, a 5° excitation function and an angular distribution at T_π = 164 MeV were extracted for the reaction $^{14}C(\pi^+,\pi^-)^{14}O(0^+, 5.92\ MeV)$. A 5° excitation function and angular distributions at T_π = 164 and 292 MeV for the reaction $^{14}C(\pi^+,\pi^-)^{14}O(2^+, 7.77\ MeV)$ are presented.

It was of interest to measure DCX cross sections on ^{13}C, an odd-A target for which data on the neighboring isotopes ^{12}C and ^{14}C would also be available. Angular distributions for $^{13}C(\pi^+,\pi^-)^{13}O(gs)$ at 164 and 292 MeV, and $^{13}C(\pi^+,\pi^-)^{13}O(4.21\ MeV)$ at 164 MeV are presented. θ = 5° cross sections were measured at T_π = 120 and 180 MeV. Through comparisons to nonanalog DCX systematics for T = 0 target nuclei, the ^{13}O(4.21 MeV) state is postulated to have $J^\pi = 1/2^-$.

This experiment (#558) was performed at the Energetic Pion Channel and Spectrometer (EPICS) at the Clinton P. Anderson Meson Physics Facility (LAMPF). The experimental setup is described in

Chapter II, and the data reduction in Chapter III. Chapter IV presents the results of the experiment and a comparison of the data to previous measurements. The systematics of the DIAS transitions are studied, and are compared to sequential charge exchange calculations.

II. EXPERIMENT

A. EPICS Channel

The A-1 pion production target is a carbon (graphite) wheel that presents a 3 cm thick target to the 800 MeV proton beam. The EPICS channel views this target at 35° with respect to the incident proton beam. Since pion production cross sections increase only as $Z^{1/3}$ [Co-72], low Z targets are desired to maximize the number of pions produced per unit energy loss in the target. The low density and thermal characteristics of carbon make it a good target for heat dissipation considerations, while its relatively low Z helps reduce multiple scattering of the incident proton beam.

The EPICS channel, shown in Fig. II-1, consists of four dipole bending magnets (BM01-4) which select a momentum bite of the pions created at the A-1 target, four sets of horizontal and vertical jaws (FJ01-4) for controlling the phase space and emittance of the pion beam, and three sets of field (quadrupole and sextupole) magnets (FM01-3) to correct for the effective field boundary of the dipole magnets. The energy range of the channel is 80 MeV to 310 MeV, which spans the Δ_{33} resonance. A coordinate system is defined in Fig. II-2a. The channel produces a dispersed beam, that is, the position in the x - direction is correlated with incident momentum (D_{ch} =

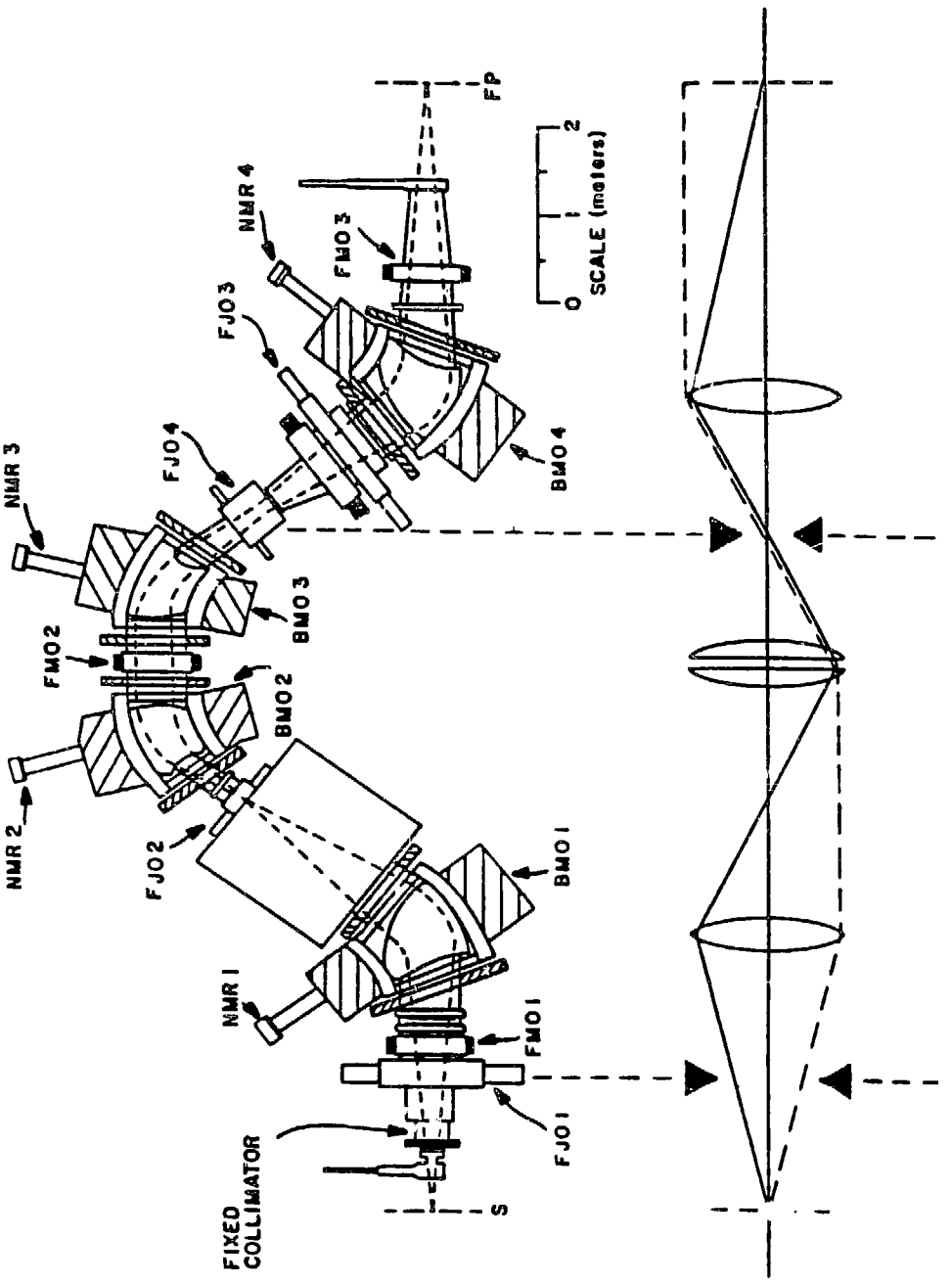

Fig. II-1: Schematic of the EPICS channel. The solid (dashed) line shows the optics in the vertical (horizontal) plane.

0.1%/cm). Although the beam has a 2% FWHM momentum spread, accurate determination of the scattering position at the target allows a final momentum resolution of 2×10^{-4} FWHM, thus permitting a factor of 200 increase in intensity over that of a monochromatic beam. The channel optics are point to point in the vertical plane and point to parallel in the horizontal plane [Th-70].

The relative intensity of the incident pion beam was monitored in two ways: (1) Pulses from 1ACM02, a charge integrating toroidal coil located upstream of the Al target in the proton beam, were scaled in CAMAC scalars. The output is proportional to the flux of pions in the the EPICS channel. (2) "Beam on Target", or BOT, is an ionization chamber in the A-1 target cell. It is also gated by BG and its signal is proportional to the product of the H^+ current and the thickness of the A-1 target. The ratio 1ACM02/BOT did not vary by more than ~2% over the course of the experiment.

B. Spectrometer

Some parameters of EPICS are shown in Table II-1. The momentum bite (±6%) of the spectrometer allows a large (~20 to ~55 MeV) region of excitation energy to be viewed at one spectrometer setting. EPICS operates in the VHV mode: vertical dispersion, horizontal scattering, vertical analysis. Three quadrupole magnets (QM01-3) provide an image of the target at the entrance to the two dipole (BM05,6) magnets. The first-order optics of the quadrupole magnets from the target to the front focus are point-to-point in the

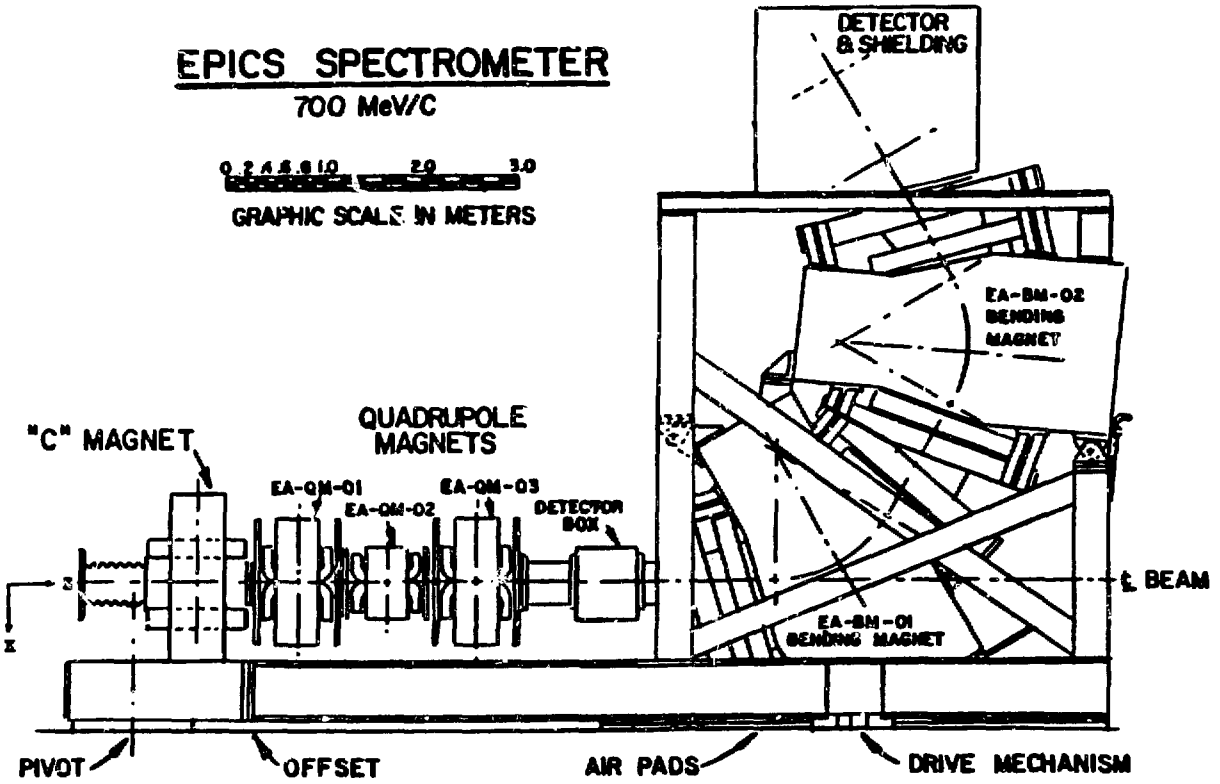

Fig. II-2a: The EPICS spectrometer.

Table II-1: EPICS specifications [MP-80].

Channel		Spectrometer	
energy range	80 to 310 MeV	momentum range	100 to 750 MeV/c
$\Delta p/p$	2% FWHM	solid angle	$\approx$ 10 msr
solid angle	3.4 msr	dispersion	4 cm/%
beam size (H×V)	8×20 cm^2	$\Delta p/p$	$\pm$6% [a]
beam divergence (H)	< 10 mrad	flight path	$\approx$ 12.5 m [b]
beam divergence (V)	100 mrad		

[a] 90 cm focal plane, useful acceptance.
[b] target to rear focal plane.

vertical (x-z) plane and parallel-to-point in the horizontal (y-z) plane, while the optics of the dipole magnets are point to point in the x-z plane and point-to-parallel in the y-z plane. The channel and spectrometer are vacuum coupled and a pressure of $\sim 10^{-4}$ Torr was maintained during the experiment. A block diagram of the EPICS spectrometer is shown in Fig. II-2b.

For DCX a sweep magnet, or "C"-magnet, is installed in front of the spectrometer, and serves to separate π^+ from π^- in the scattered beam by 20^o, in order to keep the front-chamber count rates below their limit of 10^6 Hz. This facilitates measurements at angles less than $\sim 18^o$ for DCX. Details of the field mapping and performance of the sweep magnet have been described by Greene [Gr-81]. When the sweep magnet is installed, the spectrometer is offset ten centimeters towards smaller scattering angles with respect to the pivot. This

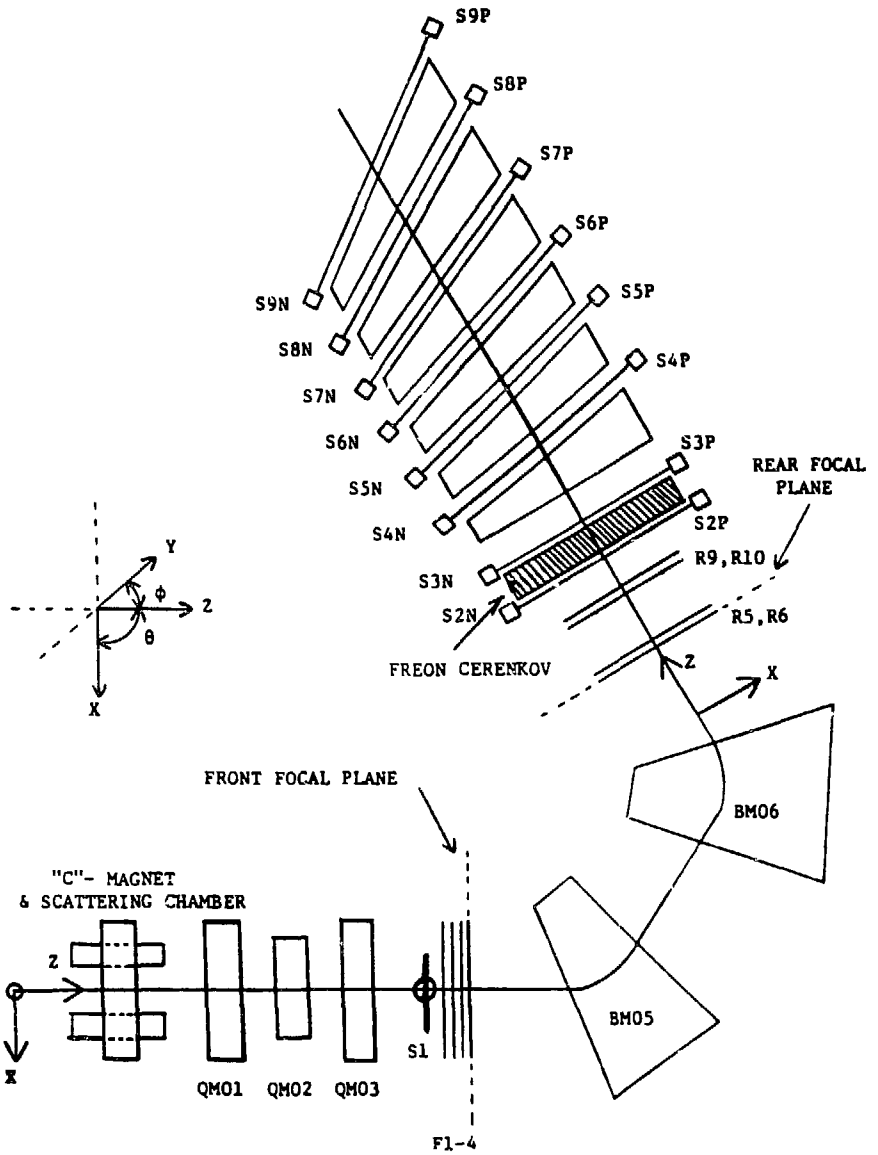

Fig. II-2b: Block diagram of the EPICS spectrometer detection system.

realigns the optic axis of the spectrometer with the beam exiting from the sweep magnet.

The front detectors consist of four (F1-4) delay-line readout drift chambers at the focus of the quadrupoles, and a scintillator (S1) upstream of the front chambers. Each chamber consists of a set of parallel anode and cathode wires in the x and an identical set in the y direction. These four chambers determine the front coordinates: x_f, y_f, θ_f (= dx/dz), and ϕ_f (= dy/dz). The design and operation of the chambers are described in detail by Morris et al. [Mo-82b] and Atencio et al. [At-81]. The drift cell size, or anode (cathode) wire spacing, is 8 mm in each direction. The anode wires are coupled to a 2.5 ns/cm delay line, and alternate field-defining cathode wires are bussed together. The outputs are obtained from both ends of the anode delay line and from both bussed cathode lines. Four pairs of chamber planes are used to unambiguously measure the coordinates. Pairs of planes are separated by 0.95 cm, and an aluminized mylar foil connected to the cathode frame provides a ground plane between wire planes.

Two types of information are obtained from the chamber signals. A time difference from the two ends of the anode delay line,

$$t_d = t_1 - t_2, \qquad \text{(II-1)}$$

is linearly related to anode wire position nearest the position of the ionizing particle (x). (In practice, a third order polynomial, which accounts for signal dispersion and other non-linearities, is used for

position calibrations.) t_d determines which wire has fired, and therefore the position to within ±4 mm. The time sum is independent of x and is proportional to the electron drift distance from the ionizing particle to the wire (20 ns/mm):

$$t_s = t_1 + t_2 + \text{(signal wire length corrections)}$$
$$= 2t_{drift} + \text{constant.} \qquad \text{(II-2)}$$

The remaining ambiguity, the side of the wire on which the pion passed, is determined from the information from adjacent parallel planes, which have their wires offset by half a drift cell size, 4 mm. The chambers operate at +2150 V, with a magic gas mixture of 65% argon, 35% isobutane, 0.1% Freon, and 0.5% isopropyl alcohol at atmospheric pressure. The position resolution of these chambers is 125 μm FWHM [Mo-82b].

The S1 scintillator forms part of the good event trigger, and provides time of flight information over the nine meter flight path to the rear scintillators (S2 and S3). The latter information is particularly valuable in $(\pi^{\pm},\pi^{\mp})$ measurements, where the scattered $\pi^{\mp}$ flux is contaminated by electrons and and muons of similar momenta. Time of flight differences allow efficient rejection of the electron and some of the muon background. S1, which is a ~150 mg/cm^2 thick Pilot B scintillator, contributes roughly 200 keV to missing mass resolution.

The rear detector system consists of four delay line readout drift chambers (R5-6, R9-10) which determine focal plane positions, x_r, y_r, ϕ_r, and θ_r, in the same manner as the front chambers. Two event defining scintillators (S2 and S3) on either side of a Freon-12 gas Cherenkov detector are followed by a stack of graphite blocks and scintillators which are known as the "Muon Rejector". S2 and S3, which are separated by ~50 cm, provide time of flight information and together with S1 and the front chambers compose the event trigger:

$$\text{EVENT} = S1 \cdot (S2 \cdot S3) \cdot \text{FRONT},$$

$$\text{FRONT} = (F1 \text{ or } F2) \cdot (F3 \text{ or } F4). \qquad \text{(II-3)}$$

Electrons passing through the EPICS spectrometer have a velocity βc greater than the Cherenkov threshold velocity in the Freon-12 gas ($\beta_t = .999$) of the Cherenkov detector, and thus emit Cherenkov radiation. Pions (and muons), which move too slowly at the same momentum to emit Cherenkov radiation, are distinguished from background electrons.

Many muons may be tagged by the "muon rejector", the design of which [Mo-84] is based on two properties: At a given momentum muons have a ≈20% greater range in matter ($-dE/dX \approx 1.5$ MeV·cm^2/gm at 300 MeV/c). Also pions are absorbed by nuclear interactions while muons are not. The thickness of graphite before each scintillator is optimized for a particular particle momentum (see Fig. II-2b). For example, most pions of kinetic energy $T_\pi \approx 100$ MeV are stopped in the graphite block before S4, while muons trigger S4 and can be vetoed.

S5 through S9 serve the same purpose for pions of kinetic energies 140, 180, 220, 260, and 300 MeV. Carbon was chosen as the absorbing material because of its relatively long radiation length (due to its low Z), large nuclear cross section (equal for π^+ and π^-), and low cost. Four percent of the pions are incorrectly identified when 96% of the muons are being rejected.

C. Electronics and Data Acquisition

Fast NIM electronics are used to amplify and discriminate mean timed scintillator signals, delay-line readout drift chamber signals, and the gas Cherenkov counter pulse height sums. Times and amplitudes are digitized by TDC's and ADC's after which about 55 data words are written directly to magnetic tape and, if sufficient computer time exists, are analyzed online by the PDP 11/45.

During part of this experiment background electrons (generated partly by the energetic knock-on process, and partly by pair production at the target) were hardware vetoed by discriminating a sum of the linear signals from the PMT's of the Cherenkov counter and using the output of an LRS 623 discriminator (threshold ~250 mV) as the input to the event trigger module. The vetoed electron events were not written to tape and increased the ratio

$$\frac{\pi + \mu \text{ events}}{e^- \text{ events}}$$

by a factor of four to five. Remaining electrons were easily eliminated from missing mass spectra via a software gate on Cherenkov pulse height.

A schematic of the EPICS electronics setup is shown in Fig. II-3. The EVENT trigger (Eq. II-3) causes the PDP-11/45 to read and then clear the CAMAC registers. Peripheral devices attached to the 11/45 were two RK05 disk drives, two Tektronix 4010 terminals, two nine-track 75 IPS 800/1600 BPI Kennedy tape drives, two 40 MB DIVA disk drives and a VERSATEC plotter and printer. A microprogrammable branch driver (MBD) is the interface between the CAMAC branch highway and the 11/45. The operating system was RSX-11/D, and the data acquisition was a modified version of the LAMPF standard data acquisition system, Q.2 [Am-79].

The software was divided into three sections: (1) An ANALYZER calculates coordinates, trajectories and momenta for each good scattering event that passes a crude particle identification test (PID). Necessary user input, such as reaction kinematics, was varied by a set of commands and data blocks. (2) The ALLTEST package tests raw data words and data words calculated in the ANALYZER. Tests on single data words are called MICROTESTS and consist of bit pattern tests, limits, and gates. MACROTESTS are logical combinations of MICROTESTS, namely AND's and OR's. (3) Updating and storing core histograms was handled by the standard LAMPF display package, which, together with DSP -- the user interface to the display package -- was used to set gates on and display any of the ~260 data words in the form of histograms or two dimensional scatter plots.

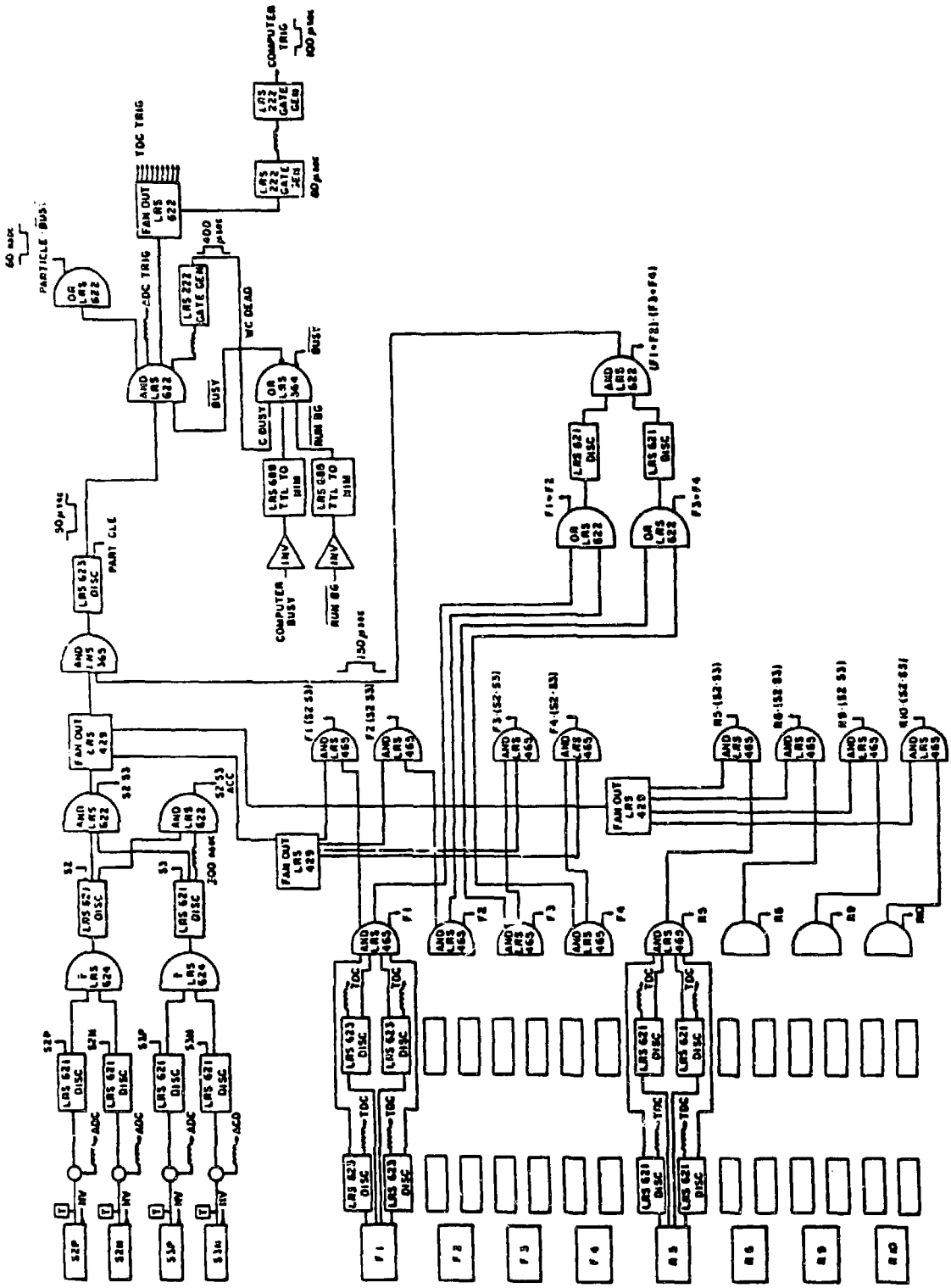

Fig. II-3: Block diagram of the EPICS electronics setup.

The ultimate quantity of interest is missing mass. Two body relativistic kinematics are calculated by the CALKIN subroutine of the ANALYZER. For a reaction $m_1(m_2,m_3)m_4$ (m_i are rest masses) with corresponding momenta and total energies p_i and $E_i = \sqrt{p_i^2 + m_i^2}$ we have

$$(Q + m_4)^2 + p_4^2 = (E_m + m_4)^2. \qquad \text{(II-4)}$$

Q is the missing mass. Missing energy, E_m, is calculated from

$$E_m = m_1 + E_2 - E_3 - m_4. \qquad \text{(II-5)}$$

E_2, m_1, m_2, m_3, and m_4 are user input to the kinematics calculations. E_3, or p_3, is determined from the front and rear wire chamber information, together with the spectrometer magnetic field settings.

D. Targets

For the purposes of this and subsequent experiments, new target cells were designed and manufactured for the ^{14}C. Previously, the ~9 gm of ^{14}C (~40 Ci) was contained in six target cells of 3 mm stainless steel picture frame construction with 25 μm steel windows. New cells were constructed of nickel, and the cell walls were 13 μm thick, or 11.3 mg/cm^2. A schematic of the new cells is shown in Fig. II-4. Nickel was electroplated onto an aluminum mandril of the desired cell size. Then the aluminum was etched out in a bath of sodium hydroxide, leaving the nickel cells behind. The carbon powder

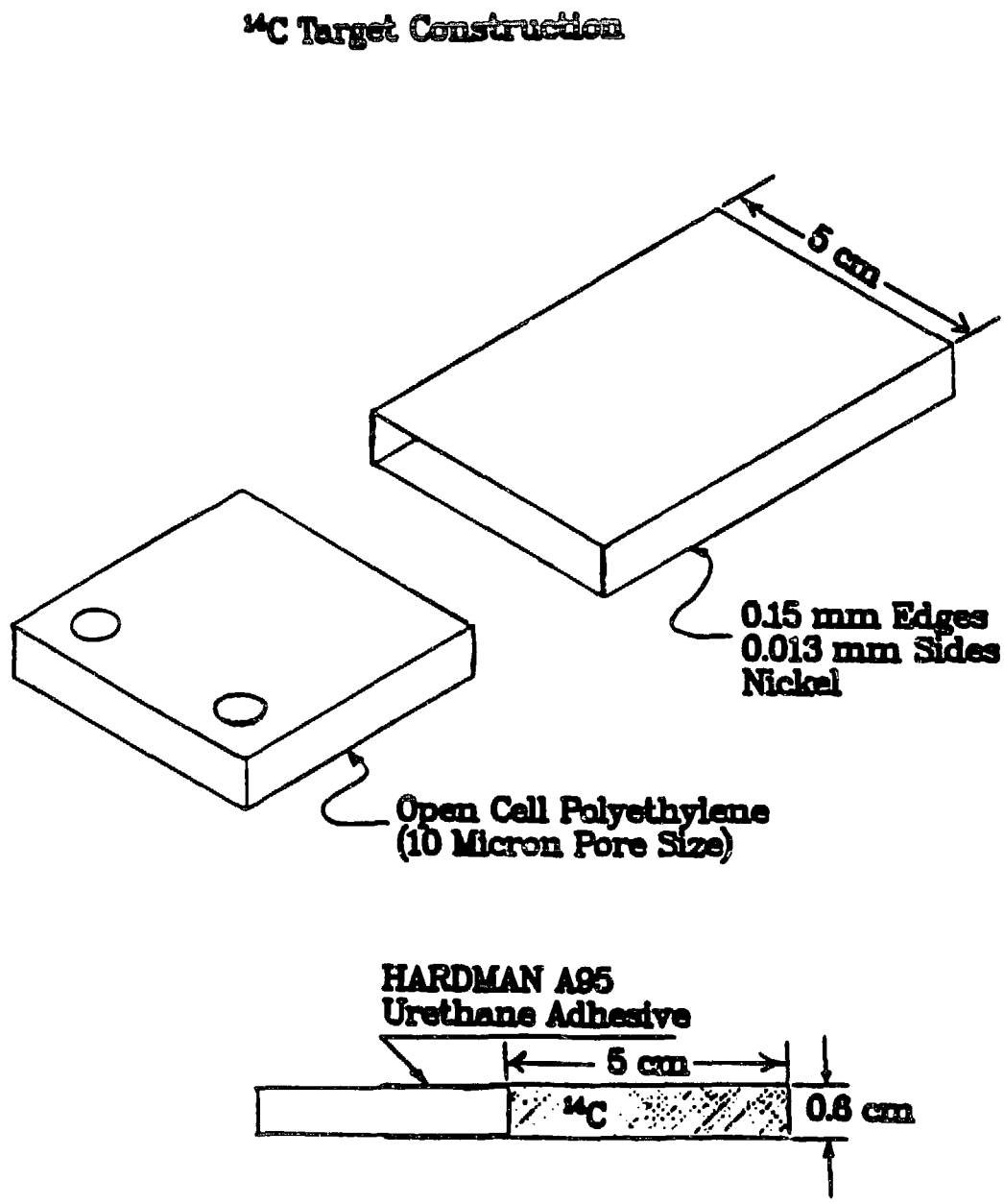

Fig. II-4: New ^{14}C target cell design.

Table II-2: ^{14}C target properties. "impurities" (mostly oxygen and magnesium) constituted 9.0 ± 3.7% of the total mass. Oak Ridge National Laboratory measurements of the atom ratio give $n(^{14}C)/n(^{12}C) = 4.6 \pm 0.4$.

	Area (cm^2)	$^{14}C + ^{12}C$ + impurities (grams)	$\rho t(^{14}C)$ (mg/cm^2)
Cell #1	5.0 × 5.3	4.49	130 ± 6
Cell #2	5.0 × 5.1	4.68	141 ± 6

was removed from the six old cells, weighed and packed into two new cells (see Table II-2). The new cells were sealed with porous polyethylene plugs (10 micron pore size) which allowed the cells to be depressurized safely and rapidly in the EPICS scattering chamber. Vacuum tests showed that the cells could be pumped down to 0.05 Atm in less than thirty seconds and exhibit no evidence of leakage when the outer surface was later swipe tested for contamination. The two new cells, instead of the old six cells, required fewer software target gates. Also, the ratio

$$\frac{\rho t(\text{carbon powder})}{\rho t(\text{cell walls})}$$

increased from 1.8 for the old design to 8.0 for the new cells. This was a great advantage for the (π^+,π^-) measurement, (and subsequent (π^-,π^+) measurements) where the optimum missing mass resolution did not need to be realized ($\lesssim$ 120 keV), but background from the target cells was desired to be at a minimum.

The isotopic thickness of the ^{14}C target assumed in this work, $\rho t(^{14}C) = 136 \pm 6$ mg/cm^2, is based on the detailed contaminant analysis of Harvey et al. [Ha-84]. Their three methods of target impurity analysis give 84.8 ± 11.9%, 75.2 ± 5.1% and 76.8 ± 5.0%, ^{14}C by weight. As in [Ha-84], the latter value is used in this work to calculate cross sections. None of the contaminants or nickel cells contributed background to the ground state region of the ^{14}O spectra due to their much more negative Q values (see Table II-3).

Two ^{13}C targets of 90% isotopic purity were used. The thick target (1340 mg/cm^2) was used for all of the new measurements reported. The thin target (635 mg/cm^2) was included for the measurements at T_π = 292 MeV and was analyzed separately from the thick target data. The cross sections at 292 MeV are weighted averages of yields from the thick and thin targets. Resolutions of

Table II-3: Nuclear g.s. Q values for double-charge-exchange reactions occurring in the ^{14}C target (top six) and for the ^{13}C, ^{26}Mg, and ^{56}Fe targets.

Reaction	Q Value (MeV)
$^{14}C(\pi^+,\pi^-)^{14}O$(DIAS)	-3.967 ± 0.009
$^{12}C(\pi^+,\pi^-)^{12}O$	-31.96 ± 0.05
$^{16}O(\pi^+,\pi^-)^{16}Ne$	-28.38 ± 0.05
$^{58}Ni(\pi^+,\pi^-)^{58}Zn$	-16.94 ± 1.00
$^{60}Ni(\pi^+,\pi^-)^{60}Zn$	-9.26 ± 0.01
$^{62}Ni(\pi^+,\pi^-)^{62}Zn$	-5.58 ± 0.01
$^{13}C(\pi^+,\pi^-)^{13}O$	-18.959 ± 0.013
$^{26}Mg(\pi^+,\pi^-)^{26}Si$(DIAS)	-8.045 ± 0.011
$^{56}Fe(\pi^+,\pi^-)^{56}Ni$	-5.679 ± 0.014

missing mass spectra for the thick and thin targets are 0.9 and 0.5 MeV, respectively.

A summary of the ^{13}C, ^{26}Mg, ^{56}Fe, and ^{1}H target properties is given in Table II-4, and a schematic of the arrangement of these targets in the scattering chamber is shown in Fig. II-5. Table II-3 shows that the Q values for the ^{13}C, ^{26}Mg, and ^{56}Fe DCX reactions allowed all of the states of interest for a given target configuration to be measured simultaneously, consistent with the useful acceptance range of the spectrometer. It should be noted that these new $^{14}C(\pi^+,\pi^-)^{14}O$ measurements are also reported in [Se-84], where $\rho t(^{14}C) = 144$ mg/cm^2 was assumed. Thus the $^{14}C(\pi^+,\pi^-)^{14}O$ cross sections quoted in this dissertation are 6% larger than those in [Se-84].

Table II-4: ^{13}C, ^{26}Mg, ^{56}Fe, and ^{1}H target properties.

Target Isotope	Chemical Composition	Isotopic Purity (%)	Isotopic Thickness (gm/cm^2)	Dimensions (cm)
^{13}C	C	90	1.340	9.2 x 10.0[a]
			0.635	10.2 x 11.3[b]
^{26}Mg	Mg	100	0.815	7.5 x 8.0
^{56}Fe	carbon steel	90.1	2.07	5.8 x 12.7[c]
				9. x 12.7[d]
^{1}H	CH_2	--	0.0105	10. x 20.

[a] Configuration a and c of Fig. II-5.
[b] Configuration c (top) of Fig. II-5.
[c] Top of configuration b of Fig. II-5.
[d] Bottom of configuration b of Fig. II-5.

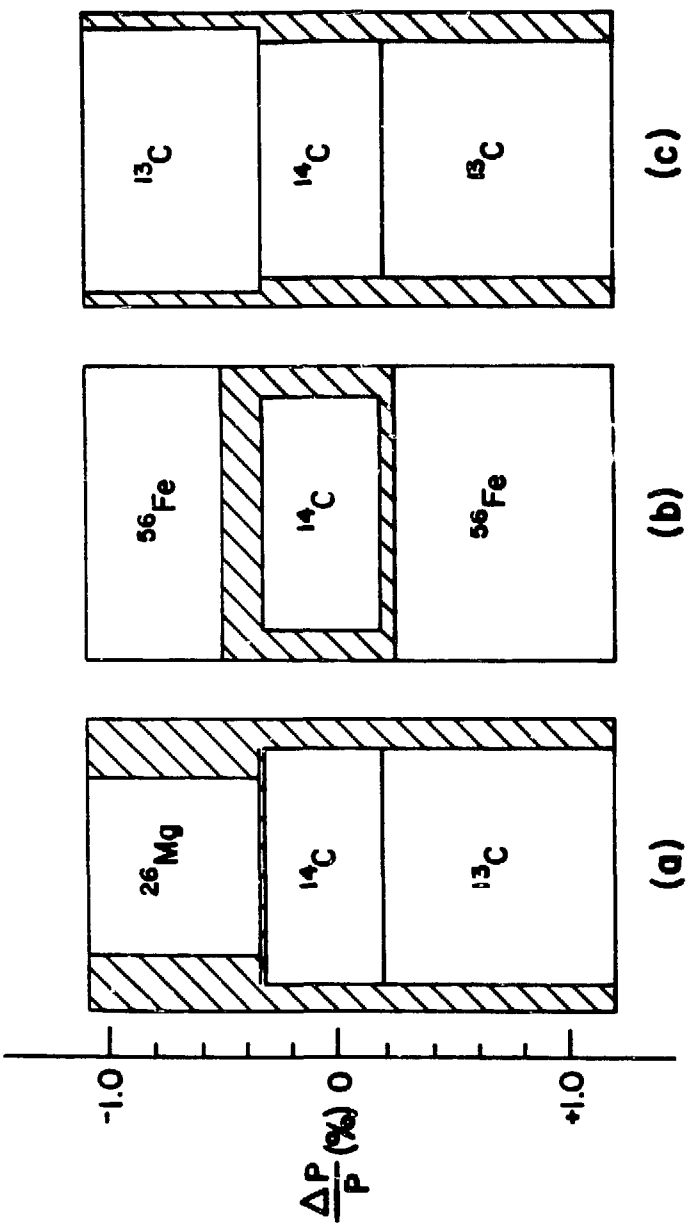

Fig. II-5. Schematic of the target arrangement in the EPICS momentum dispersed pion beam.

III. DATA REDUCTION

Gates on the data words x_{tgt}, y_{tgt}, ϕ_{tgt}, and θ_{tgt}, the target coordinates, provide some of the background rejection. An x_{tgt} histogram is shown in Fig. III-1, where background electrons have not been rejected from the histogram, and make up ~80% of the counts. Due to the differing Z and areal densities of the ^{13}C, ^{14}C (including nickel cells), and ^{26}Mg targets, the edges of the targets are well defined. Gates were placed on each of the three targets, and their corresponding missing mass spectra were separately histogrammed.

In order to eliminate events that scattered from the spectrometer beam pipe, gates were placed on calculated radii at two points between the spectrometer entrance and the front chambers. These "flange cuts" rejected less than 2% of the events.

Muons passing through the focal plane arise from either in-flight decay of pions in the spectrometer or elastic scattering of incident beam muons. Most muon events corresponding to pion decays between the front and rear chambers are vetoed by gating the data words θ_{ch} and ϕ_{ch}. θ_{ch} (ϕ_{ch}) is calculated from an empirically determined polynomial [Bo-79] with dependent variables x_f, θ_f, and δ_{sp} (y_f, ϕ_f, and δ_{sp}). The polynomial represents the difference between the rear angle θ_r (ϕ_r) and a calculated rear angle based on θ_f and x_f (ϕ_f and y_f) front chamber measurements. Good pion events have θ_{ch} and

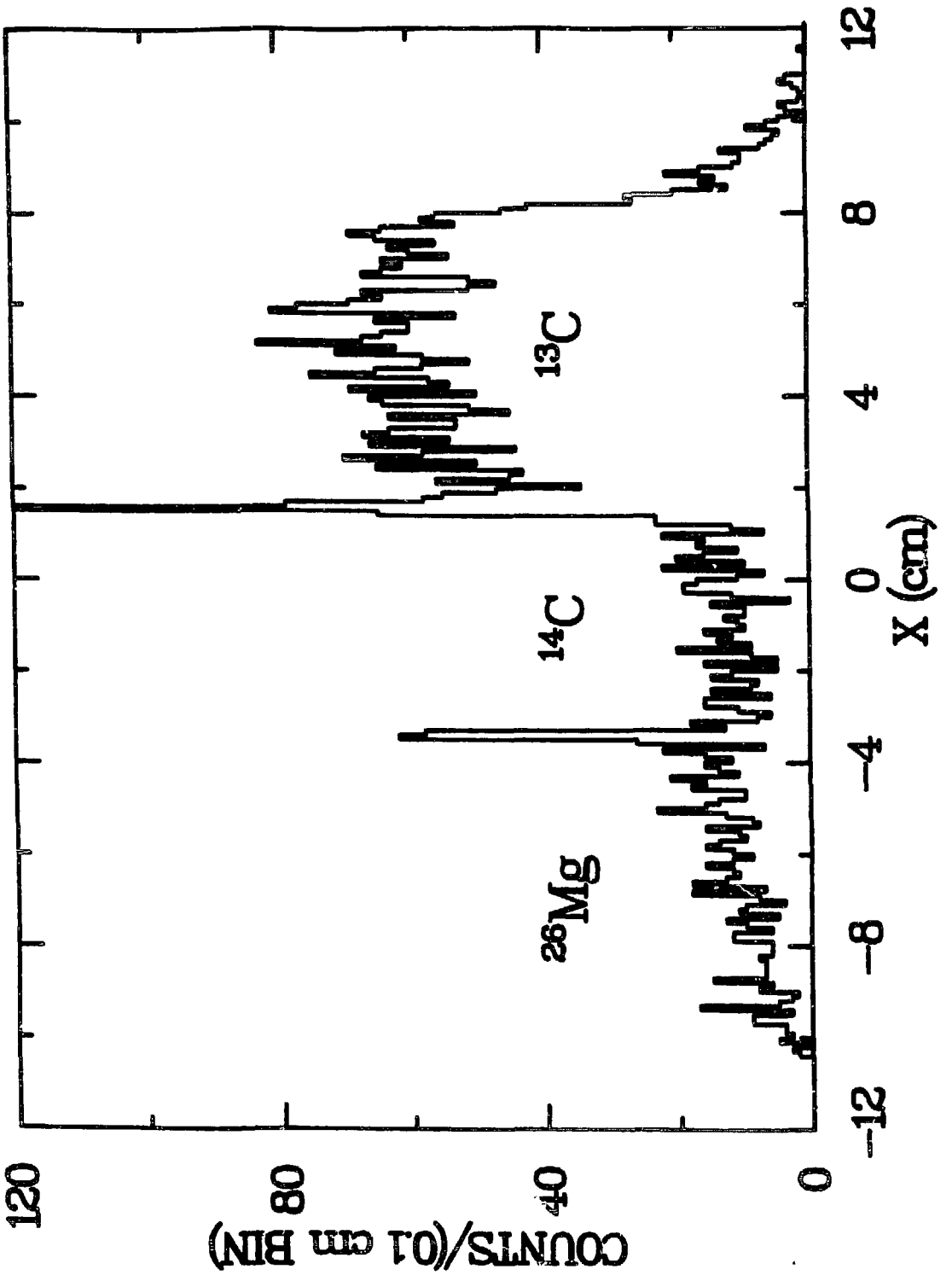

Fig. III-1: Histogram of x_{tgt}. ^{26}Mg, ^{14}C, and ^{13}C are the targets, from left to right.

ϕ_{ch} distributions no wider than 20 mrad, while the $\pi \rightarrow \mu + \nu$ decay cone has an opening angle of ~550 mrad at T_π = 120 MeV and ~230 mrad at T_π = 292 MeV. Thus, events falling outside the 20 mrad gate are assumed to be muon events, and at least 95% of muon events are rejected in this fashion.

The 9 m flight path between S1 and (S2•S3) provides a complimentary method to the muon rejector for rejecting scattered beam muons. Fig. III-2 shows that muons are well separated in time from pions at lower energies. The fact that they are less well resolved at higher energies is compensated for by their relatively lower fraction of scattered beam composition [Se-81].

Initial particle identification (PID) was obtained from the S2 to S3 time of flight and the geometrical mean of the S2 and S3 pulse heights. EVENTS were required to pass gates on both words simultaneously (BOX test). If a trigger did not pass the PID test the analyzer was interrupted and proceeded to process the next event. This BOX test, shown in Fig. III-3, was unable to distinguish background electrons and muons from pions. Much remaining background was rejected by placing a BOX test on the data words: "Corrected S1 Time of Flight" (CTOF) and "Cherenkov Pulse Height Sum" (CPH). CTOF is the S1 to (S2•S3) time of flight, corrected for path length differences of different particle trajectories. A dot plot of these two data words is shown in Fig. III-4. Electrons with non-zero CPH are distinguished from the much more massive pions and muons along the vertical axis. Some muons with shorter S1 times of flight than pions

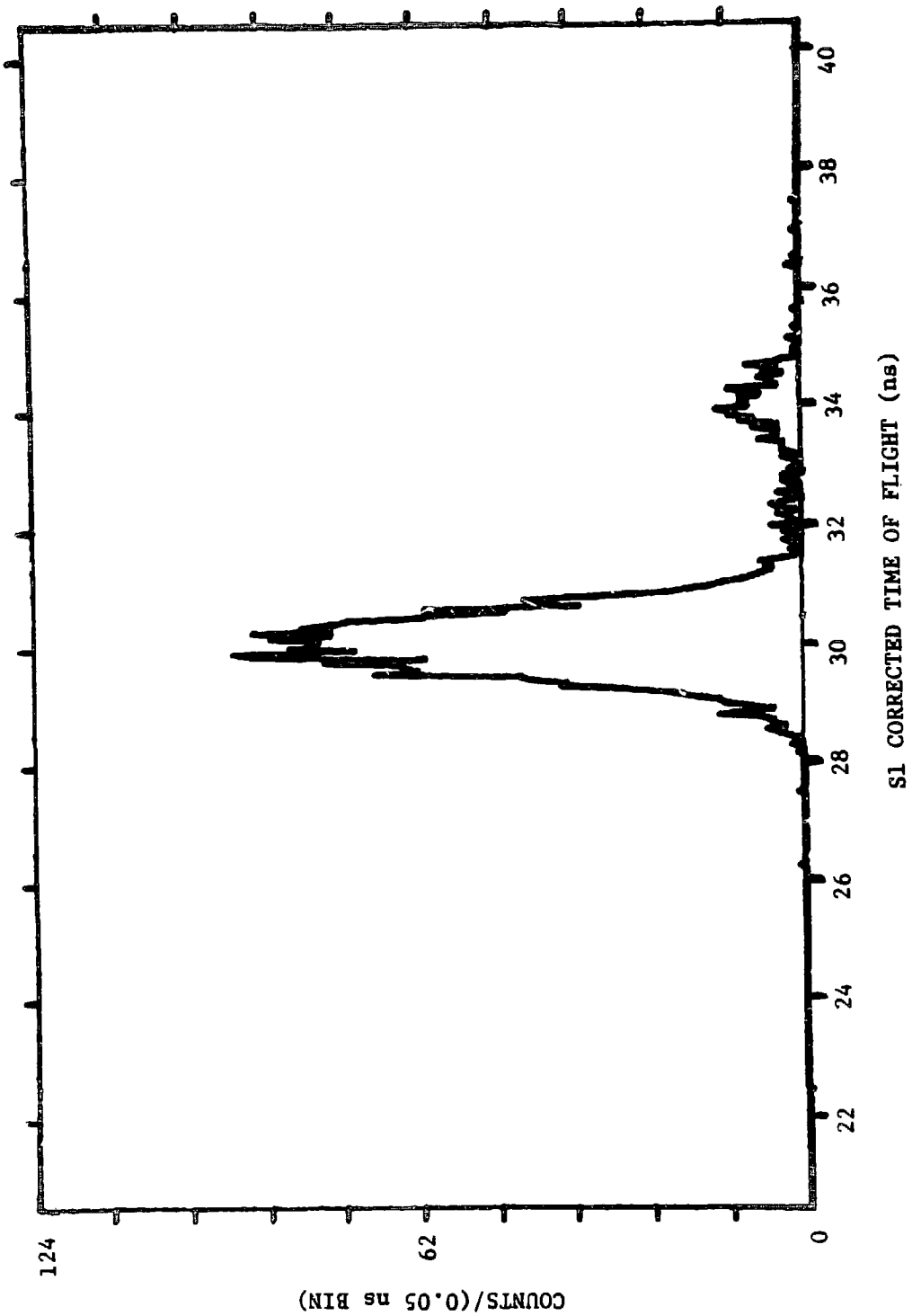

Fig. III-2: S1 to (S2•S3) time of flight spectrum at T_π = 164 MeV.

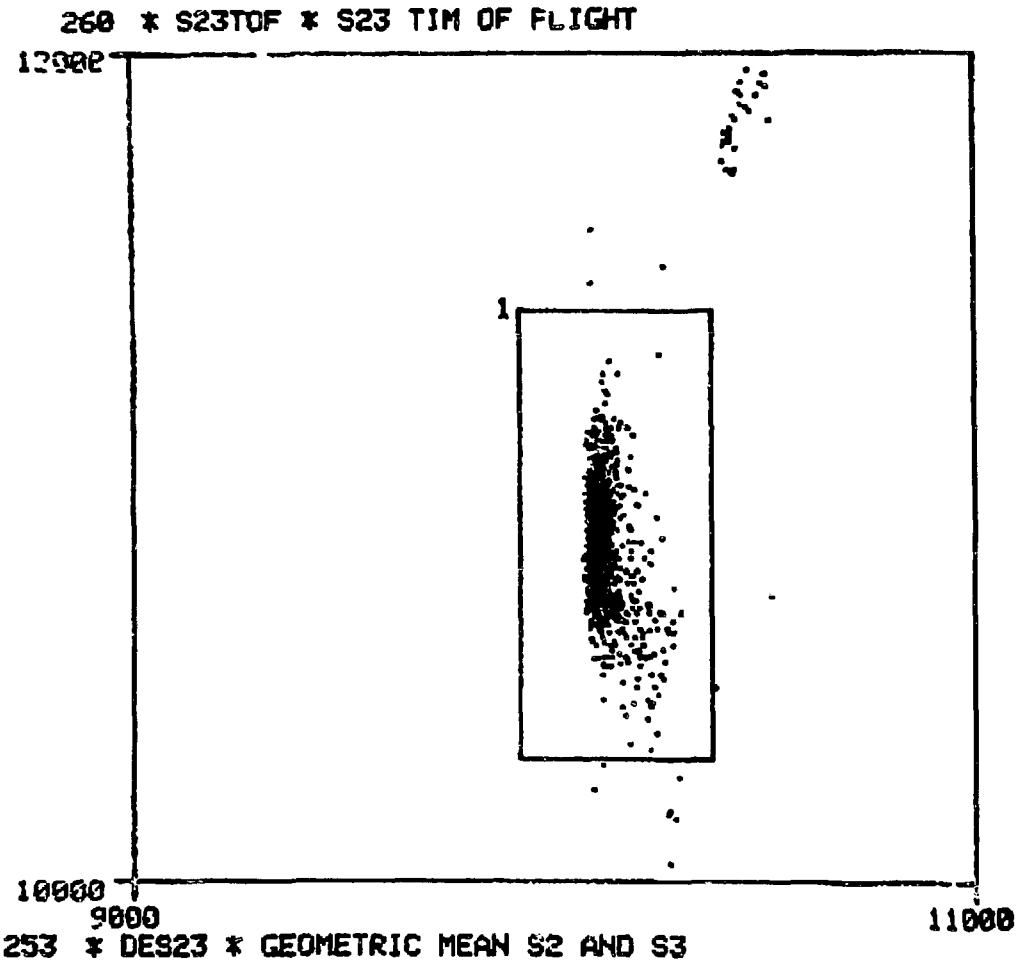

Fig. III-3: S2 to S3 time of flight versus the geometric mean of the S2 and S3 pulse heights for $^{1}H(\pi^{+},\pi^{+})$ at T_{π} = 292 MeV.

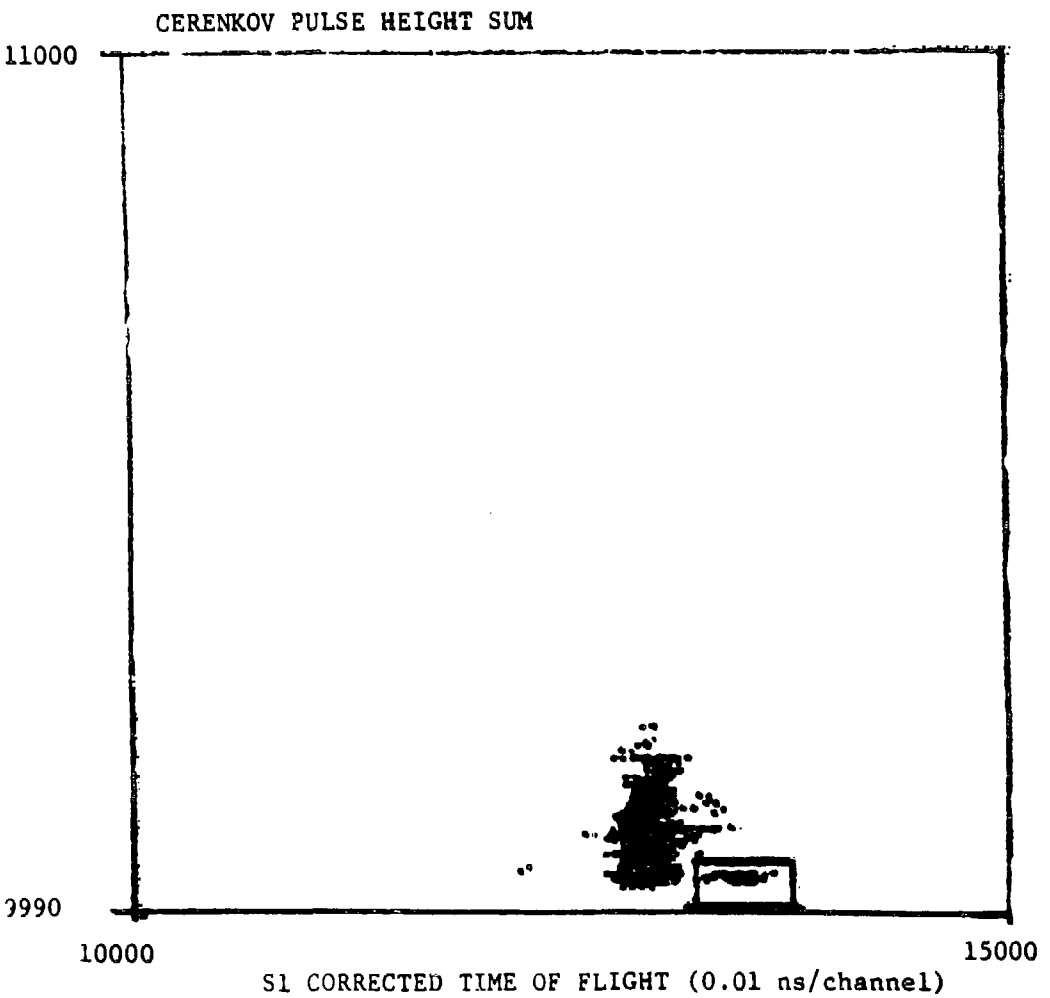

Fig. III-4: Cherenkov Pulse Height Sum versus S1 Corrected Time of Flight. Electrons with large pulse height sums were hardware rejected.

were included in the BOX, but were rejected by a gate in the CTOF spectrum (Fig. III-2).

The fractional deviation of pion momentum from the momentum of the central trajectory through the spectrometer is denoted δ_{sp},

$$\delta_{sp} = \frac{p_\pi - p_{sp}}{p_{sp}}. \qquad \text{(III-1)}$$

The varying spectrometer acceptance as a function of scattered particle momentum is measured by the yield as a function of δ_{sp}. This is done by varying the spectrometer magnet settings, and effectively moving the peak of ^{1}H$(\pi^+,\pi^+)^{1}$H across the focal plane of the spectrometer. The resulting acceptance scans are shown in Fig. III-5. Because strip target configurations were used, and the acceptance of the spectrometer varies as a function of x_{tgt}, the acceptance had to be determined for each of the three different DCX target positions. Target configurations in the incident beam are shown in Fig. II-5.

Missing mass spectra for ^{13}C, ^{14}C, ^{26}Mg are shown in Fig. III-6. The peaks for the DIAS are well separated in energy from the other low-lying states of the residual nuclei. An indication of the efficiency of background rejection is evidenced by the near absence of counts between the ^{14}O(gs) and the first excited state at 5.17 MeV ($J^\pi = 1^-$). The background in this region is on the order of 30 nb/sr/MeV, while the cross section for the transition to the ground state is ~1 μb/sr. The energies of the excited 0^+, 3^-, and 2^+ states of ^{14}O are 5.92 MeV, 6.27 MeV, and 6.59 MeV respectively (see Fig.

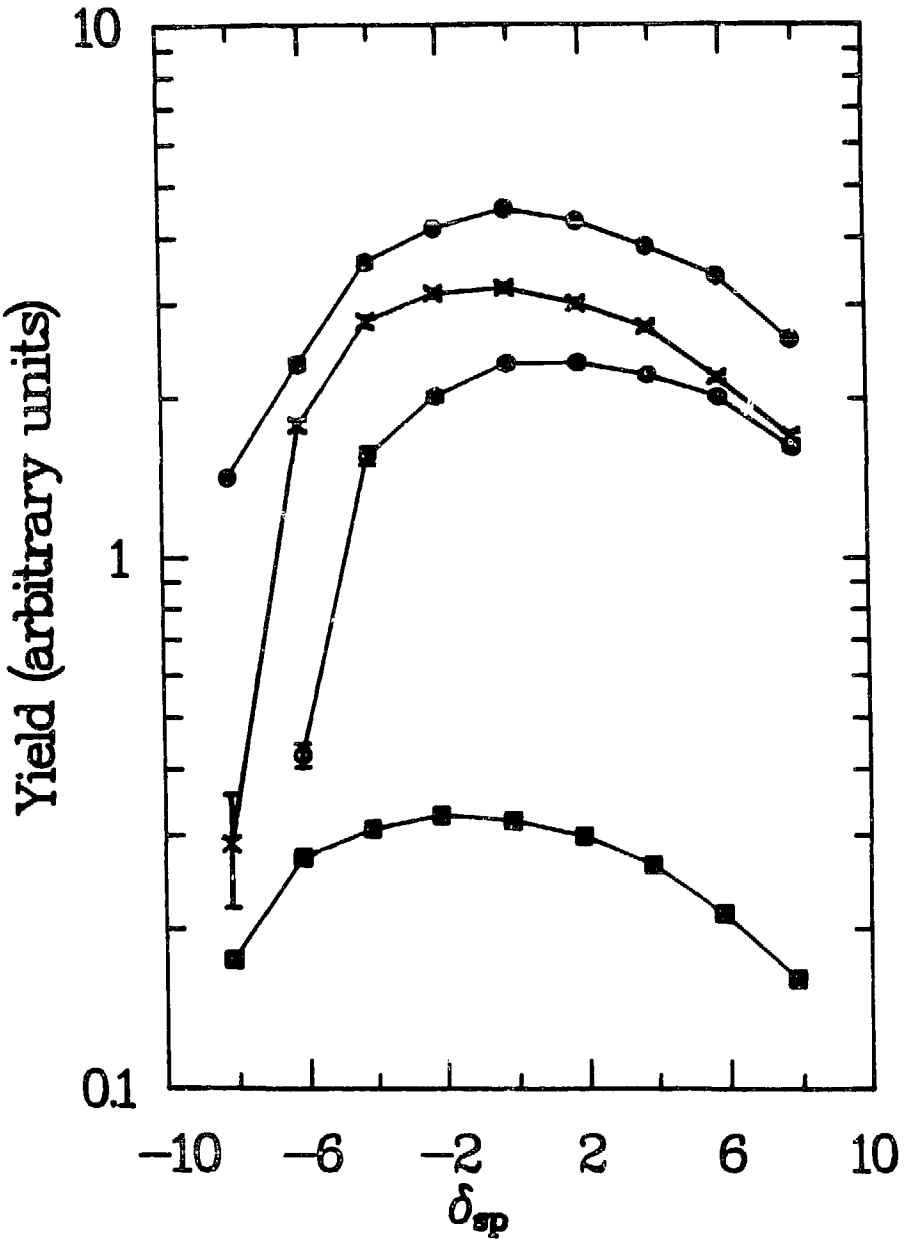

Fig. III-5: Spectrometer acceptance for ^{56}Fe (solid circles), ^{14}C (crosses), ^{26}Mg (open circles), and ^{13}C (squares). Yields were measured for $^{1}H(\pi^{+},\pi^{+})^{1}H$ at $\theta = 40^{o}$ and $T_{\pi} = 164$ MeV with a CH_2 target of areal density 152 mg/cm^2.

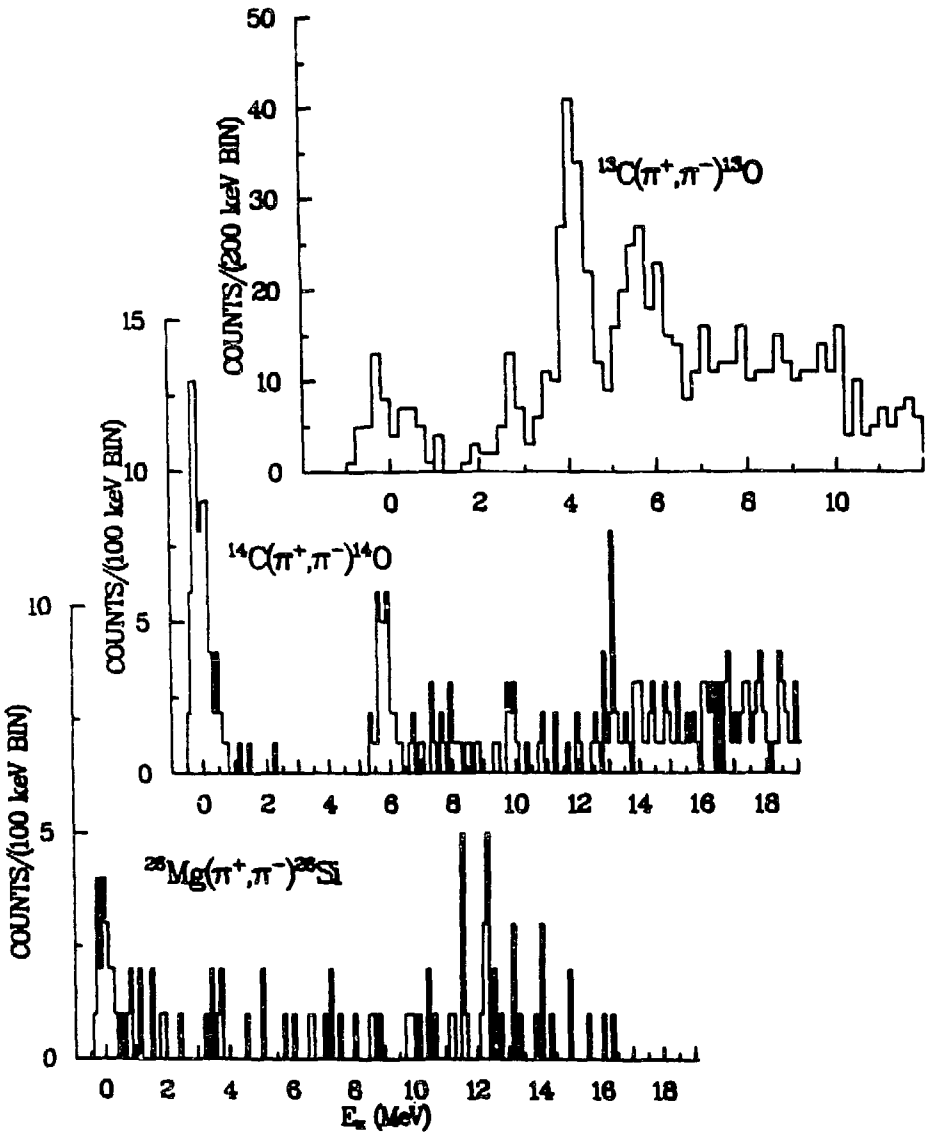

Fig. III-6: Missing mass spectra for $^{13}C,^{14}C,^{26}Mg(\pi^+,\pi^-)^{13}O,^{14}O,^{26}Si$ at T_π = 164 MeV, $\theta = 5^o$.

III-8). The FWHM energy resolution for the spectrum is 400 - 500 keV, making reliable extraction of cross sections difficult for these states. The regions to the left of the ground states of ^{56}Ni, ^{26}Si, and ^{13}O show little or no evidence of DCX counts originating from targets of more positive Q value, lending credence to the ability to resolve target boundaries well in the x_{tgt} spectra.

The number of counts in the peaks were determined by using the PEKFIT routine [S1-76]. For the transitions to the ground states of ^{13}O, ^{14}O, ^{26}Mg, and ^{56}Ni the determination of the peak areas was straightforward: Based on the peak-free regions to the left and right of the ground states, the number of background counts was estimated and was subtracted from the total number of counts in the peak region. The same method was employed for the ^{14}O(0^+_2, 5.92 MeV) state, but the fits were hampered by the unresolved 6.27 MeV, 3^- state. For the fits to the ^{56}Ni(T = 2, 9.6 MeV) state, (spectra are shown in Fig. III-7), a region of excitation energy was fit with a constant background. The position and width (0.56 MeV FWHM) of the peak were determined from a sum of the excitation function data.

The differential cross section is related to the peak area by:

$$\frac{d\sigma}{d\Omega} = \frac{\text{peak area} \times A}{\rho t \times N_o \times (I\Delta\Omega)} \times \frac{1}{EFF} \times \frac{1}{\cos\theta_{tgt}}. \qquad \text{(III-2)}$$

A = mass number of target nucleus.

ρt = areal density of target.

$N_o = 6.02 \times 10^{23}$ nucleons/gram.

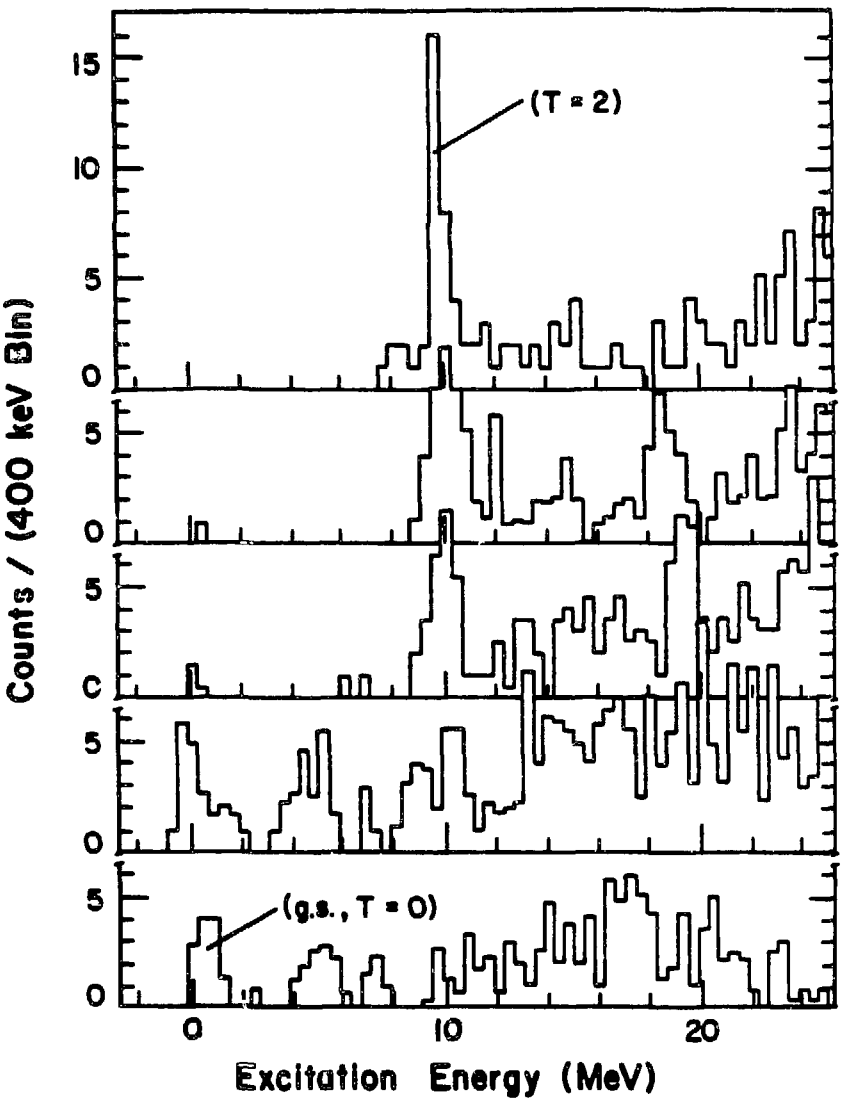

Fig. III-7: Comparison of spectra for the $^{56}Fe(\pi^+,\pi^-)^{56}Ni$ reaction at T_π = 140, 164, 220, 260, 292 MeV (from bottom to top).

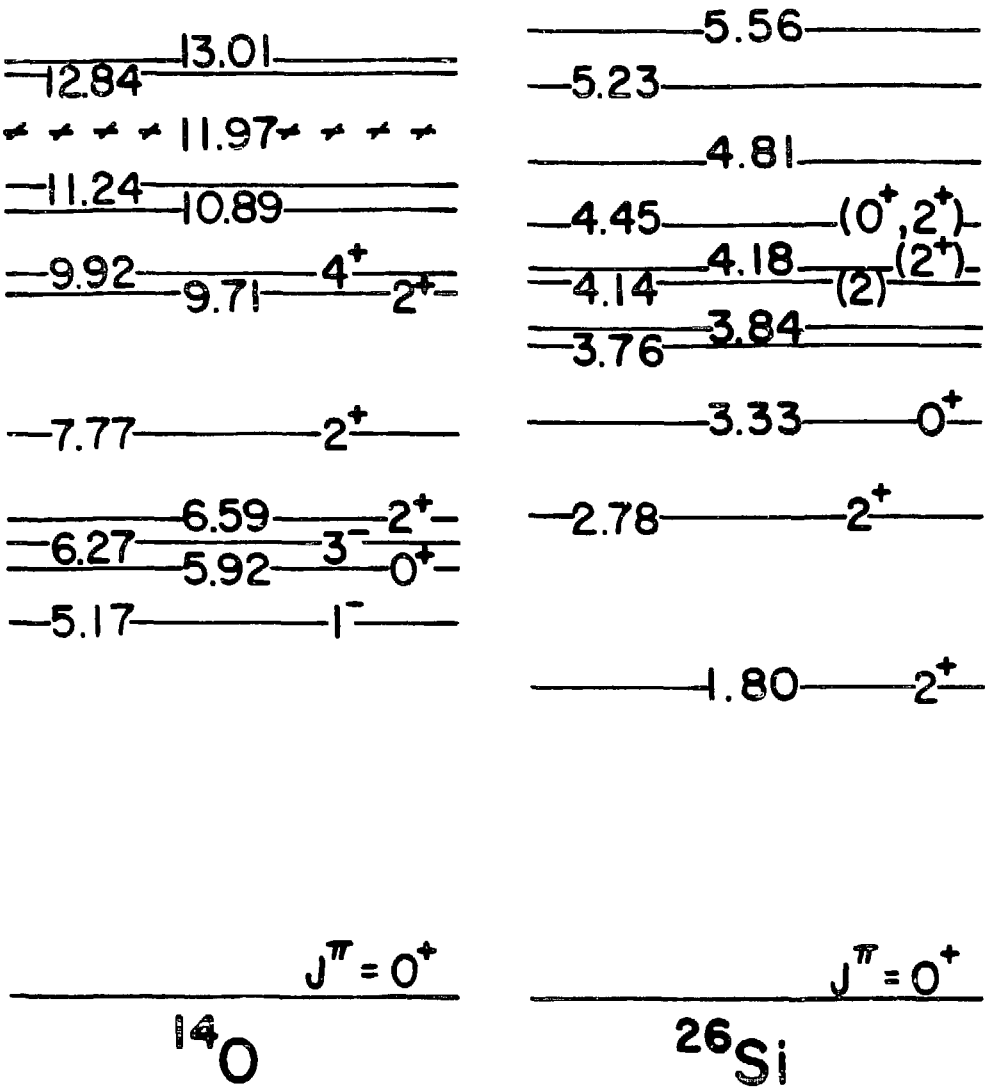

Fig. III-8: Energy level diagrams of ^{14}O and ^{26}Si. Excitation energies are in units of MeV.

I = # pions/sec incident on target.

$\Delta\Omega$ = solid angle of spectrometer.

EFF = efficiency of detection system.

= SF×CEFF×DEFF×LT.

I is proportional to 1ACM02 (and BOT), and $\Delta\Omega$ ($\approx$10 msr) is not absolutely known. Thus, normalization runs were done to calibrate I$\Delta\Omega$. Yields for $^{1}H(\pi^{+},\pi^{+})^{1}H$ were measured at each energy for which data were taken ($\theta = 50^{o}$) with a full sized (10 cm × 20 cm) CH_2 target of areal density 73.5 mg/cm^2. x_{tgt} gates consistent with those placed on the DCX targets were used to determine the π-p yields for each of the target positions in the incident beam.

For the $^{14}C,^{26}Mg,^{56}Fe(\pi^{+},\pi^{-})$ data absolute normalization factors were determined by comparing these yields to cross sections calculated from the π-p phase-shift fits of Rowe, Salomon and Landau (RSL) [Ro-78, Bu-n.d.]. Normalization factors for the $^{13}C(\pi^{+},\pi^{-})$ contain π-p cross sections calculated from the phase shift analysis of Carter, Bugg, and Carter (CBC) [Ca-73, Wa-79], which differed from RSL cross sections by $\leq$1%, except for T_{π} = 120 MeV, where σ_H calculated from RSL was 4% higher than that calculated from CBC. The cross section is then expressed as:

$$\frac{d\sigma}{d\Omega} = \frac{2}{14} \times \frac{\text{yield(DCX)}\times A(\text{DCX})}{\rho t(\text{DCX})} \times \frac{\sigma_H \times \rho t(CH_2)}{\text{yield(H)}} \times G$$

$$\text{yield} = \frac{\text{peak area} \times \cos\theta_{tgt}}{\text{EFF} \times \text{1ACM02} \times \text{DOMEGA}}. \qquad \text{(III-3)}$$

DOMEGA is the relative yield as a function of δ_{sp}, and is obtained from the acceptance scans (Fig. III-5). θ_{tgt}, the angle subtended by the incident beam and a line normal to the target, is 30^{o} less than the spectrometer angle (20^{o} less than the true scattering angle). G is the lab to center-of-mass frame jacobian. All of the new and previously measured cross sections in this work are in the center-of-mass frame. The errors quoted for the cross sections (tabulated in Appendix A) include only the statistical uncertainty of the DCX and $^{1}H(\pi^{+},\pi^{+})$ peak areas.

The survival fraction, SF, corrects for pions that decay between the target and the focal plane of the spectrometer. This is given by:

$$SF = \exp(-m_{\pi}D/p_{\pi}c\tau_{o}), \quad \text{where} \qquad \text{(III-4)}$$

$c\tau_{o} = 7.804$ meters $\qquad p_{\pi}$ = pion momentum

m_{π} = pion rest mass $\qquad D = 12.28 - 0.035\delta_{sp}$ meters (flight path).

The chamber efficiency is a product of the efficiencies of the eight anode and eight cathode wire planes:

$$\text{CEFF} = \prod_{i=1}^{N} \frac{\text{All OK}}{\text{All but i OK}} \approx 0.95. \qquad \text{(III-5)}$$

The drift efficiency, DEFF (≈ 0.8), is the ratio of events which do not pass drift time differences tests between adjacent paired planes (i.e., calculated trajectories are required to agree with all of the chamber positions to within 1.6 mm), but register good signals in all wire planes. The computer live-time, LT (≈ 1.0 in DCX experiments), is calculated from the ratio EVENTS•$\overline{\text{BUSY}}$/EVENTS, and corrects for trigger events occurring while the 11/45 was reading from CAMAC and writing to tape a previous event.

There are systematic uncertainties associated with the extraction of these cross sections. DCX target thicknesses (including impurities), ρt(DCX), are known to within 2%, while the CH_2 target thickness is known to 0.6%. The isotopic purity for each of the ^{13}C, ^{26}Mg, and ^{56}Fe targets is known to within 1%, while the ^{14}C target isotopic purity has an uncertainty of 6% [Ha-84]. The uncertainty in the calculation of the π-p cross sections from the programs CROSS [Bu-n.d.] or SCATPI [Wa-79] is 3%. CEFF, beam monitoring, DOMEGA, and SF have respective uncertainties of 3%, 3%, 2%, and 3%. The uncertainty in the placement of target gates in the x_{tgt} spectra for DCX and $^1H(\pi^+,\pi^-)$ is ±4%. The sum of all of these effects in quadrature gives an overall systematic uncertainty in the data of ≤±10%.

A weld between the sweep magnet and the scattering chamber, which helps maintain the alignment between the scattering chamber, sweep magnet and spectrometer, was discovered broken at the end of the experiment. This resulted in a ~1 cm scattering chamber misalignment in the horizontal plane. Comparisons of π^+-p yields measured at

different times during the experiment indicate that this could have had a ±5% effect on the DCX cross sections. However, the time at which the weld broke is not known, and could not be inferred from any of the histogrammed coordinates. Therefore, no corrections have been made to any subset of the data to account for the possible loss of flux arising from the misalignment.

In addition to the $\theta = 5^{o}$ overlap point, $^{26}Mg(\pi^{+},\pi^{-})^{26}Si(DIAS)$ at $T_{\pi} = 120$ MeV, which agrees well with the result of Greene [Gr-81] (see Fig. IV-1), another normalization check was measured by Gilman et al. in September 1983 [Gi-83]. Their determination of the $^{14}C(\pi^{+},\pi^{-})^{14}O(DIAS)$, $T_{\pi} = 292$ MeV cross section of $d\sigma/d\Omega = 4.62 \pm 0.54$ μb/sr is in good agreement with with the cross section reported here, $d\sigma/d\Omega = 4.51 \pm 0.59$ μb/sr. Good agreement was found for the $^{13}C(\pi^{+},\pi^{-})^{13}O(gs)$ measurement at $T_{\pi} = 180$ MeV: the new measurement is $d\sigma/d\Omega(5^{o}) = 83 \pm 19$ nb/sr, compared to $d\sigma/d\Omega(5^{o}) = 94 \pm 28$ nb/sr.

IV. RESULTS

A. Transitions to the DIAS

1. Excitation functions

The new data are shown in Fig. IV-1. The new datum for $^{26}Mg(\pi^+,\pi^-)^{26}Si(gs)$ at T_π = 120 MeV agrees with the previous measurement [Gr-82a], and the new data at 164 and 180 MeV make clear the similarity of the excitation functions for ^{18}O and ^{26}Mg. Both are peaked at $T_\pi \approx 140$ MeV, have a minimum near $T_\pi \approx 170$ MeV and increase towards the maximum measured energy of 292 MeV. In Fig. IV-2, the new excitation functions are compared to analog DCX for five other target nuclei. The energy dependence of $^{42}Ca(\pi^+,\pi^-)^{42}Ti(gs)$ [Ka-83] is consistent with the above description for that of ^{18}O and ^{26}Mg.

On the other hand, the excitation functions for $^{14}C(\pi^+,\pi^-)^{14}O(gs)$ and $^{56}Fe(\pi^+,\pi^-)^{56}Ni(DIAS,\ 9.6\ MeV)$ increase monotonically over the energy range measured. The $^{48}Ti(\pi^+,\pi^-)$(DIAS, 8.75 MeV) excitation-function data [Ka-83] strongly resembles the ^{56}Fe data, and it is interesting to speculate that the ^{14}C, ^{48}Ti, and ^{56}Fe reactions might possess local maxima for $T_\pi < 140$ MeV, analogous to those observed in the ^{18}O and ^{26}Mg data at $T_\pi \approx 140$ MeV. It is difficult to say whether the $^{48}Ca(\pi^+,\pi^-)^{48}Ti(DIAS,\ 17.38\ MeV)$ data [Ka-83]

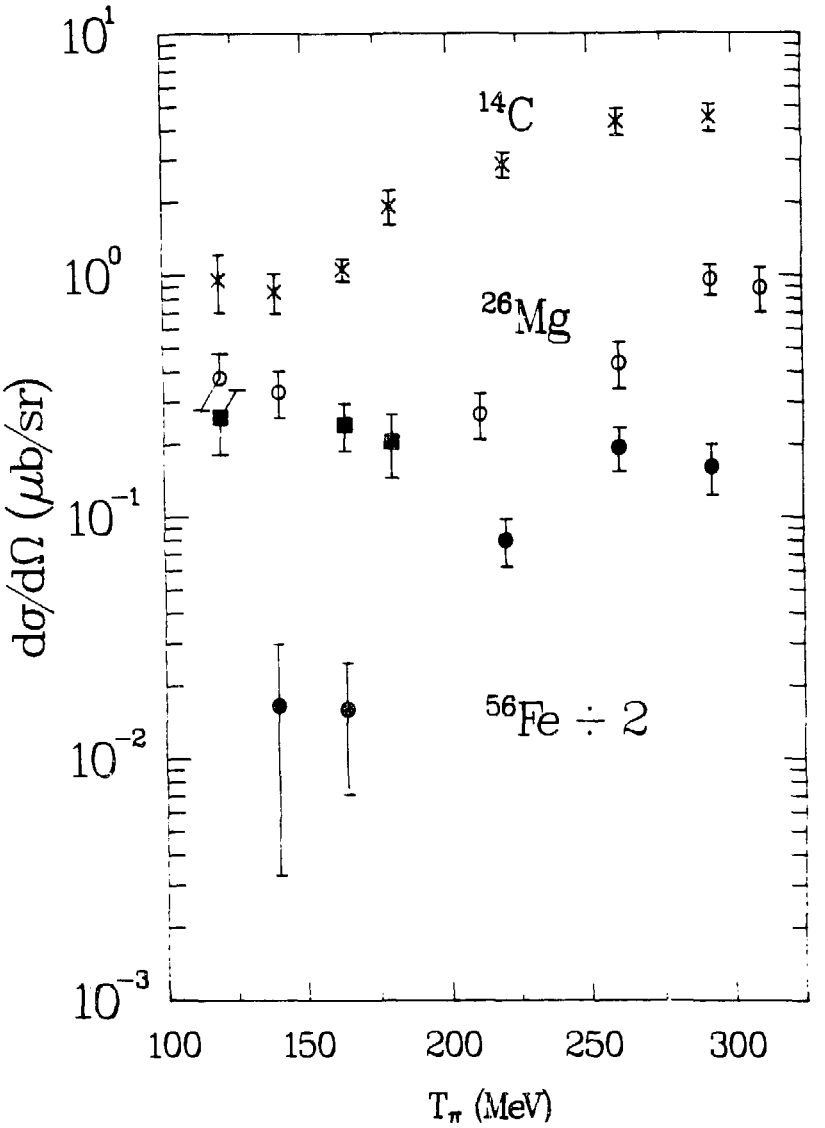

Fig. IV-1: New DIAS excitation function data for $^{14}C(\pi^+,\pi^-)^{14}O$ (crosses) and $^{26}Mg(\pi^+,\pi^-)^{26}Si$ (squares for this work and open circles from [Gr-82a]). The closed circles are $(d\sigma/d\Omega)/2$ for $^{56}Fe(\pi^+,\pi^-)^{56}Ni$(DIAS, 9.6 MeV).

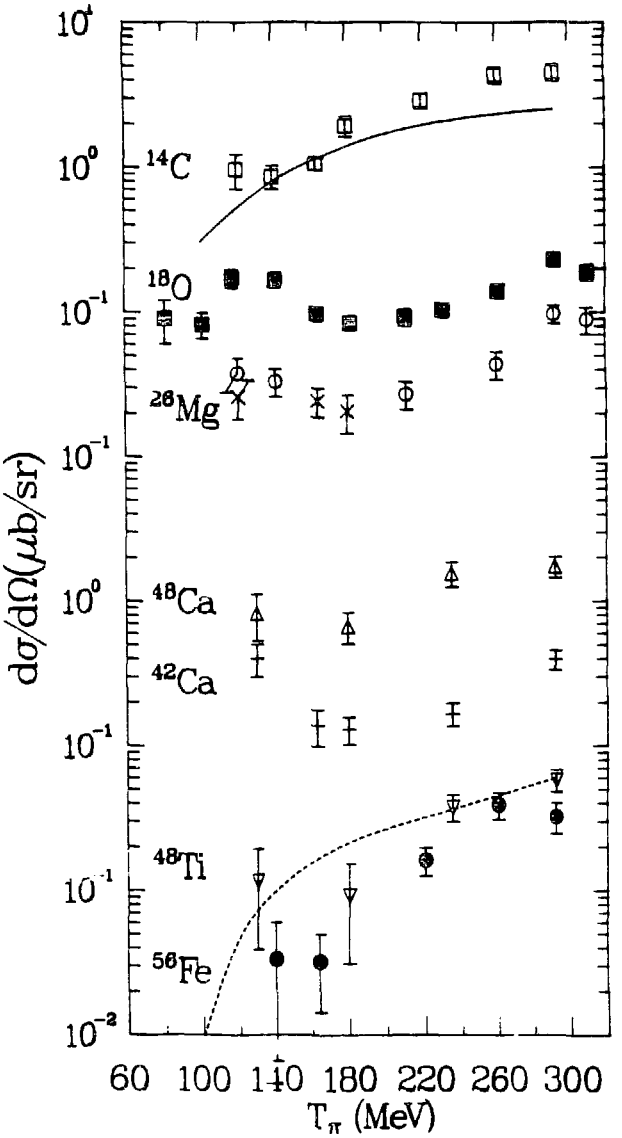

Fig. IV-2: Excitation functions for $A(\pi^+,\pi^-)A'(DIAS)$. The ^{26}Mg data represented by circles and the ^{18}O data are from [Gr-82]. The data for ^{42}Ca, ^{48}Ca, and ^{48}Ti are from [Ka-83]. The solid and dashed curves are lowest-order PIESDEX [Jo-83b] calculations for $^{14}C(\pi^+,\pi^-)^{14}O(gs)$ and $^{56}Fe(\pi^+,\pi^-)^{56}Ni(DIAS, 9.6\ MeV)$, respectively.

most resembles the ^{18}O and ^{26}Mg excitation functions, or the monotonic shape of the ^{14}C, ^{48}Ti and ^{56}Fe excitation functions. Across the Δ_{33} resonance, and for a wide range of target nuclei, a monotonically increasing DIAS excitation function is a common feature of DCX calculations that treat the process as sequential charge exchange through the free π-nucleon amplitude. Optical-potential calculations have been performed with the computer program PIESDEX for some of the isospin conserving reactions discussed. (See [Jo-83b], and Chapter V. No second-order isoscalar (ρ^2), isovector ($\rho\Delta\rho$), or isotensor ($\Delta\rho^2$) terms have been included in the calculations presented in this chapter.) The shapes of the excitation functions for ^{14}C and ^{56}Fe are in rough agreement with these lowest-order optical potential calculations. For $T_\pi \leq 200$ MeV, the $^{18}O(\pi^+,\pi^-)^{18}Ne(gs)$ excitation function has been shown to be in strong disagreement with a similar (sequential charge exchange through the isobaric analog state in ^{18}F) calculation [Mi-81]. These results suggest that in the case of ^{14}C and ^{56}Fe, for $T_\pi > 140$ MeV, charge exchange through the intermediate analog state dominates the reaction amplitude, while for ^{18}O, more interesting physics must be invoked to explain the data.

2. Angular distributions

The new angular distributions for $^{14}C,^{26}Mg(\pi^+,\pi^-)^{14}O,^{26}Si(gs)$ at T_π = 164 MeV are compared with that for ^{18}O in Fig. IV-3. At T_π = 164 MeV the ^{18}O and ^{26}Mg angular distributions have first minima occurring at small momentum transfers. The $^{14}C(\pi^+,\pi^-)^{14}O(gs)$ angular distribution does not possess a well defined minimum, perhaps due to nuclear structure effects peculiar to ^{14}C. However, the decrease in cross section between 0° and 20° is consistent with a shallow minimum near $\theta \approx 20^\circ$. The ratios of the first maximum to the second maximum in the three angular distributions are a smooth function of A: 5.1 ± 1.7, 4.0 ± 0.9, and 1.5 ± 0.5 for $^{14}C,^{18}O,^{26}Mg(\pi^+,\pi^-)^{14}O,^{18}Ne,^{26}Si(gs)$, respectively.

The three angular distributions at T_π = 292 MeV (Fig. IV-3) are similar in that they exhibit deep minima at momentum transfers consistent with sequential charge exchange calculations. Data are lacking in the region of the second maximum, making a comparison of the cross sections at the first and second maxima impossible at this energy.

PIESDEX [Jo-83a] calculations are compared with the angular-distributio.. data in Fig. IV-3. The failure of the angular-distribution calculations at T_π = 164 MeV and the partial success of the calculations at T_π = 292 MeV indicate the complexity of the DCX reaction mechanism near the Δ_{33} resonance energy and suggests the need for a second amplitude in the reaction.

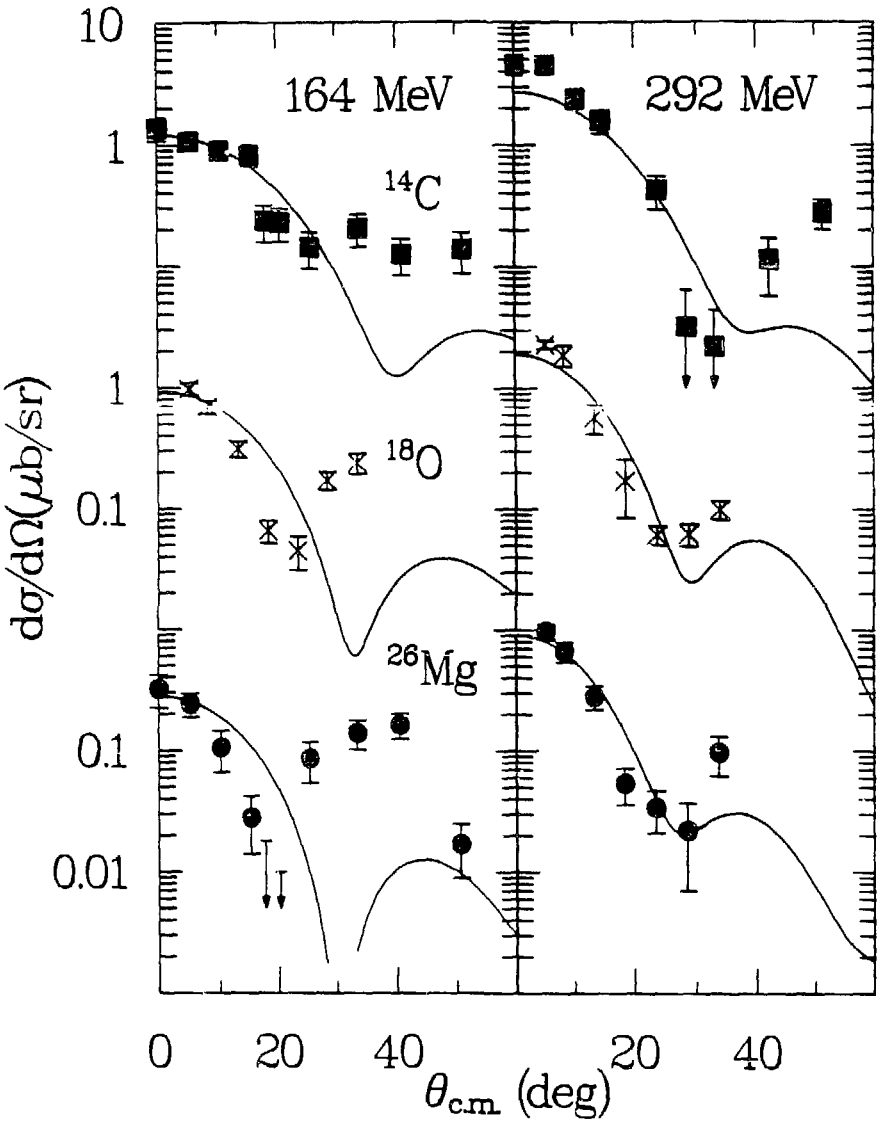

Fig. IV-3: Angular distributions at T_π = 164 and 292 MeV for the reactions: $^{14}C(\pi^+,\pi^-)^{14}O(gs)$, (squares) $^{18}O(\pi^+,\pi^-)^{18}Ne(gs)$ (crosses, from [Gr-82a]), and $^{26}Mg(\pi^+,\pi^-)^{26}Si(gs)$ (circles). The data for the latter at T_π = 292 MeV are from [Gr-82a]. The curves are lowest order optical potential calculations from the theory of [Jo-83b].

The six angular distributions are plotted as a function of qR in Fig. IV-4, where q is the momentum transfer and R is a suitable strong absorption radius for the target nuclei. Values of R for ^{14}C, ^{18}O and ^{26}Mg are 3.18, 3.46 and 3.91 fm, respectively, calculated from $R = 1.32\ A^{1/3}$. These radii correspond to $\rho(R)/\rho(0) \approx 0.2$ for the Hartree-Fock (Skyrme-III effective interaction [Be-75]) nuclear densities that were used for the PIESDEX calculations. At $T_\pi = 164$ MeV, the angular distributions exhibit minima at $qR \approx 1.7$, whereas at $T_\pi = 292$ MeV the minima appear at $qR \approx 3.5$.

3. A dependence

Forward angle cross sections for transitions to double isobaric analog states as a function of target mass are shown in Fig. IV-5, with straight lines corresponding to an $(N-Z)(N-Z-1)A^{-7/3}$ mass dependence, and $(N-Z)(N-Z-1)A^{-10/3}$ for comparison. The $A^{-7/3}$ expression better describes the data for $T = 1$ target nuclei at both energies and the agreement with the curve is better at 292 MeV than at 164 MeV. There is no known fundamental significance of this observed mass dependence; however, Johnson and Siciliano have shown that the geometric $(N-Z)(N-Z-1)A^{-10/3}$ dependence is violated when an isotensor term is included in the pion-nucleus optical potential [Jo-83b]. The addition of ρ^2 dependent terms to the pion-nucleus optical potential can describe much existing 164 MeV SCX and $T > 1$ DCX data for transitions to isobaric analog states (see Chapter V). It should be

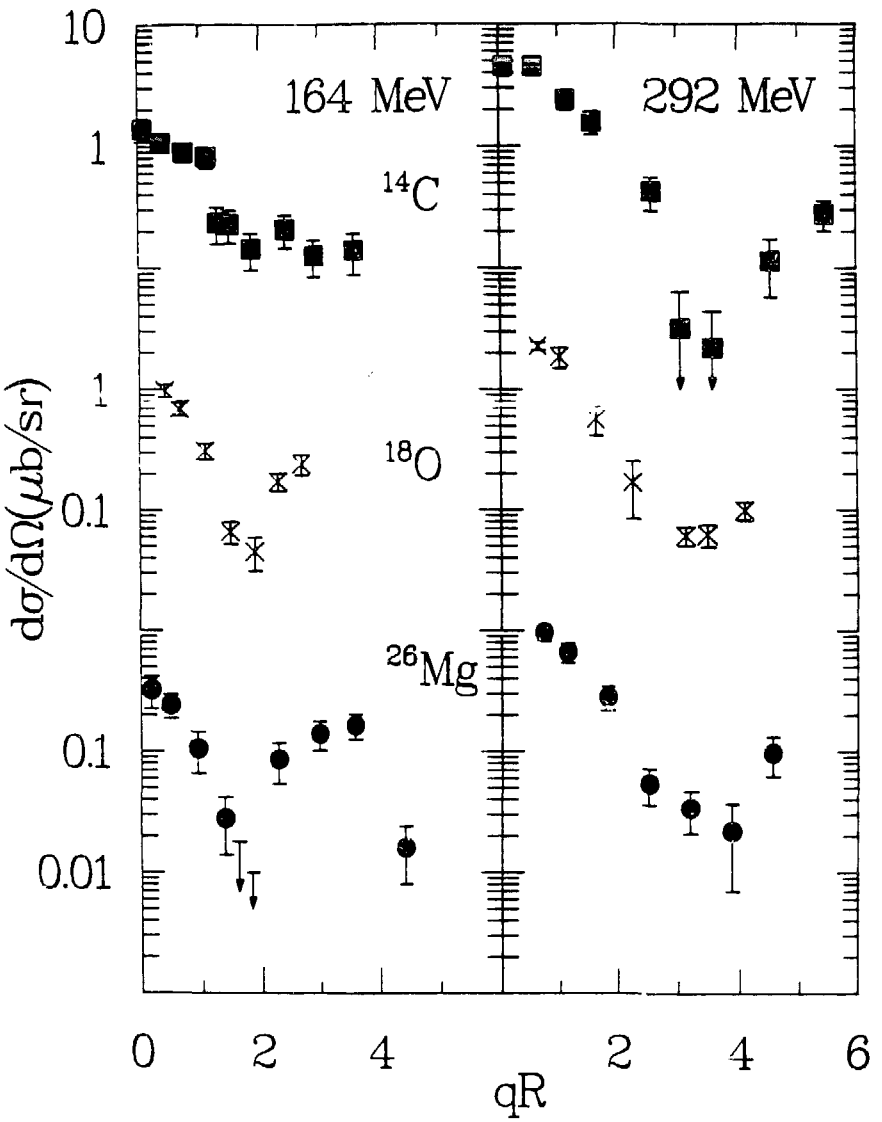

Fig. IV-4: The same data as in Fig. IV-3 plotted versus qR.

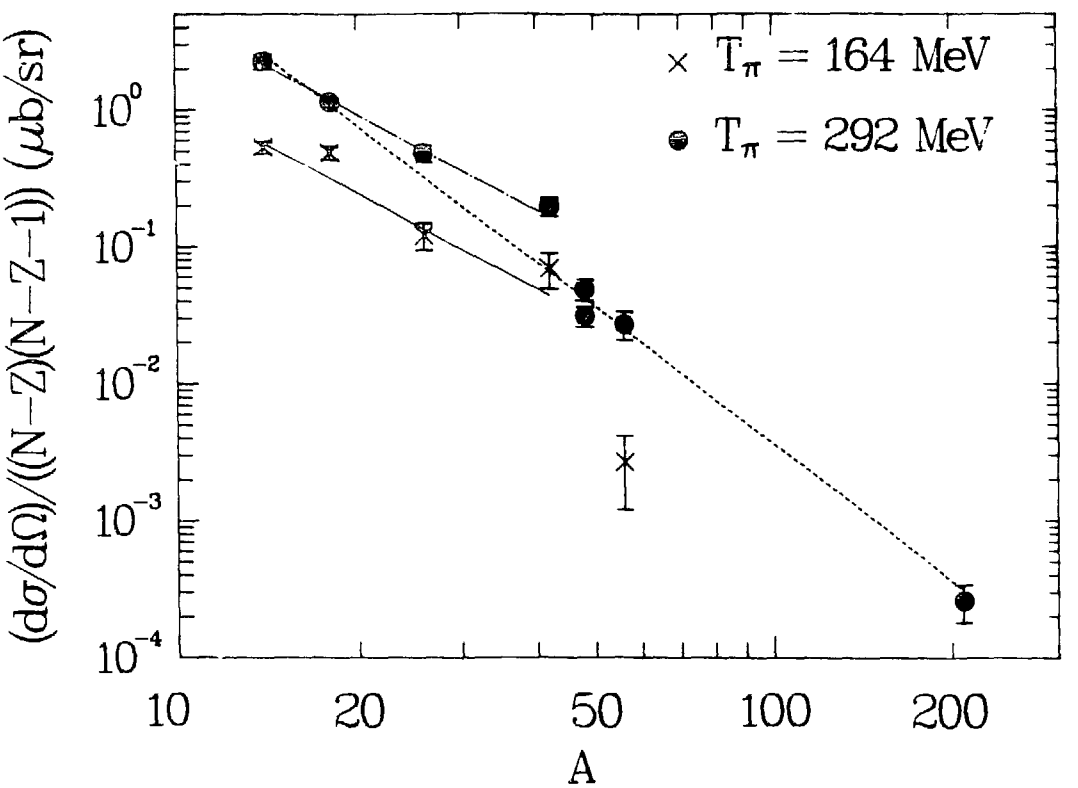

Fig. IV-5: Forward angle cross sections as a function of target mass for T_π = 164 MeV and 292 MeV. ^{18}O was measured by Greene et al. [Gr-82a]. ^{26}Mg at 292 MeV was measured by Greene et al., and ^{42}Ca is from [Ka-83]. The dot-dash and solid lines are an $A^{-7/3}$ mass dependence at 292 and 164 MeV, respectively. The dashed line is an $A^{-10/3}$ mass dependence.

noted that when $T > 1$ data are included, the forward angle DCX data are fit better by $(N - Z)(N - Z - 1)A^{-10/3}$.

The transition to a smoother $(N - Z)(N - Z - 1)A^{-10/3}$ dependence is shown in Fig. IV-6, where the ^{14}C and ^{26}Mg data have been multiplied by ratios of $A^{10/3}$, and emphasize that the transition to an irregular mass dependence occurs for $T_\pi \leq 200$ MeV.

A varying A dependence as a function of energy for the analog (π^+,π^o) 0^o differential cross section has been noted by Sennhauser et al. [Sen-83]. Based on fits to SCX data for $7 \leq A \leq 208$, the mass dependence changes from about $A^{-1.4}$ at $T_\pi = 100$ MeV to $A^{-1.1}$ at $T_\pi = 295$ MeV. There is no subset of analog DCX data for which a similar trend is observed.

B. Nonanalog transitions

1. $0^+ \rightarrow 0^+$ transitions

The transition to the $^{56}Ni(gs)$ does not suffer from the the same identification problem as the DIAS since it is well separated from the first excited state of ^{56}Ni. The spectra comparison of Fig. III-7 exhibits the difference of the energy dependence of the nonanalog transition (to the $^{56}Ni(gs)$) and the transition to the DIAS at $E_x = 9.6$ MeV. At lower energies, the excitation of the $^{56}Ni(gs)$ is clearly seen, whereas there are no ground state events at $T_\pi = 292$ MeV. The spectrum at 292 MeV is dominated by the DIAS whereas at $T_\pi = 140$ MeV no clear signal appears for this state.

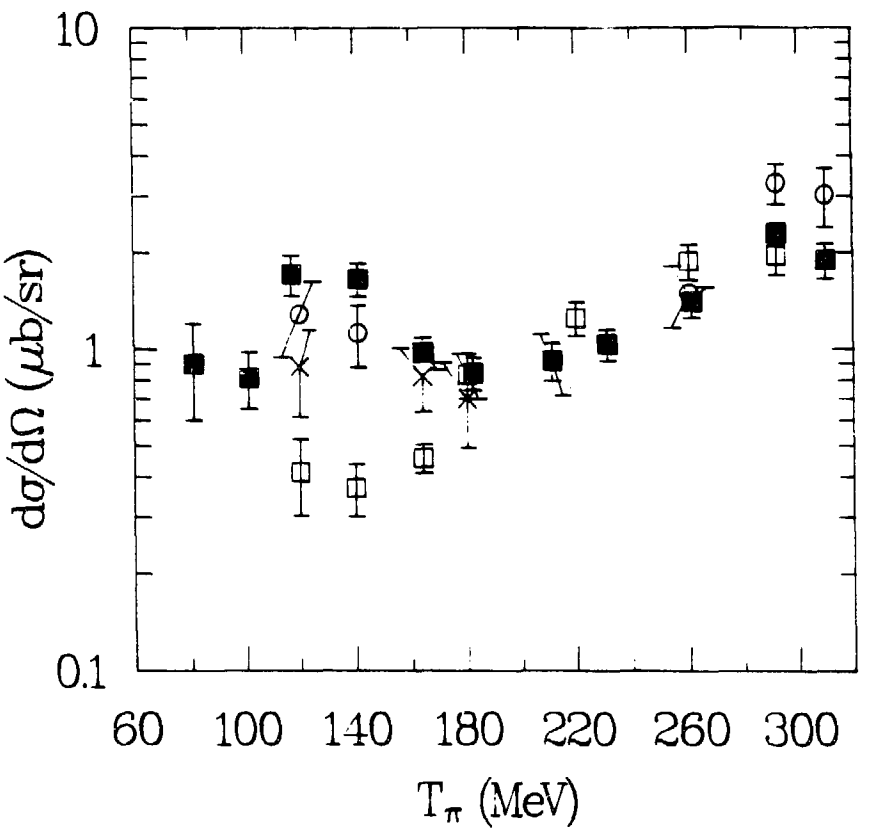

Fig. IV-6: DIAS excitation functions of $^{14}C(\pi^+,\pi^-)^{14}O$ (open squares), $^{18}O(\pi^+,\pi^-)^{18}Ne$ (solid squares, from [Gr-82a]) and $^{26}Mg(\pi^+,\pi^-)^{26}Si$ (crosses are new data, open circles are from [Gr-82a]). By multiplying by ratios of $A^{-10/3}$, the data for ^{14}C and ^{26}Mg are displayed on the scale of the ^{18}O data.

The excitation function for a region 0.5 MeV wide centered about the position of the $^{14}O(0^+, 5.92\ MeV)$ state is shown in Fig. IV-7, along with that for the $^{56}Fe(\pi^+,\pi^-)^{56}Ni(g.s.)$ reaction. Both decrease with increasing pion kinetic energy, a feature also seen in other $\Delta J = 0$ non-analog DCX reactions [B1-83]. The data are compared with curves obtained from a Breit-Wigner expression for the cross section,

$$\sigma_{BW}(T_\pi) = \frac{N\Gamma^2}{4k^2\left((T_\pi - T_{res})^2 + \Gamma^2/4\right)},$$

plus a background proportional to the PIESDEX cross sections (Fig. IV-7) to account for the less dominant analog reaction mechanism. In [B1-83], Breit-Wigner expressions were used to extract peak positions and widths for the excitation functions on T = 0 target nuclei. For the non-analog transitions shown in Fig. IV-7 the widths have been fixed to be 70 MeV (an average value from [B1-83]) and the data have been fit to obtain peak positions of 148 MeV and 149 MeV for $^{14}C(\pi^+,\pi^-)^{14}O(0^+, 5.92\ MeV)$ and $^{56}Fe(\pi^+,\pi^-)^{56}Ni(g.s.)$, respectively. These peak positions are 10 to 20 MeV lower than those reported for the reactions studied in [B1-83].

The angular distribution for $^{14}C(\pi^+,\pi^-)^{14}O(0^+, 5.92\ MeV)$ is shown in Fig. IV-8. Poor statistics prevent making meaningful comparisons with the known characteristics of non-analog DCX reactions, but the data are consistent with the presence of a minimum near 30^o.

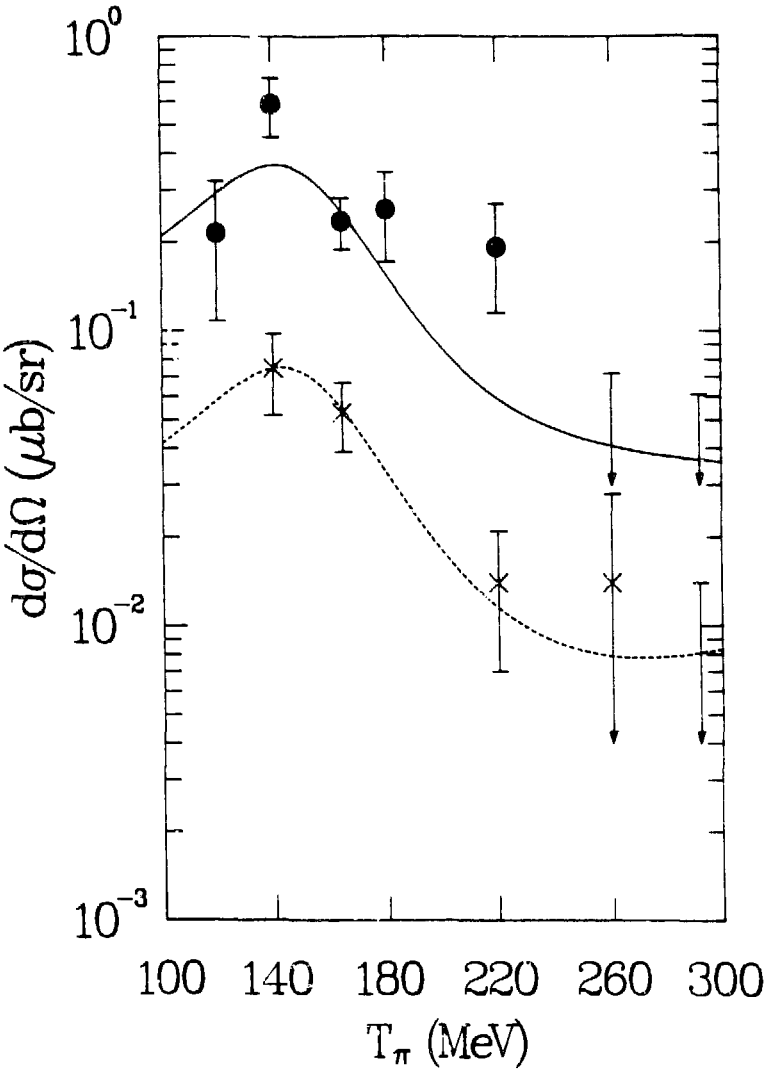

Fig. IV-7: Excitation functions for $^{14}C(\pi^+,\pi^-)^{14}O(0^+,$ 5.92 MeV) (circles) and $^{56}Fe(\pi^+,\pi^-)^{56}Ni(g.s.)$ (crosses). The curves are obtained from a Breit-Wigner expression, plus a background term.

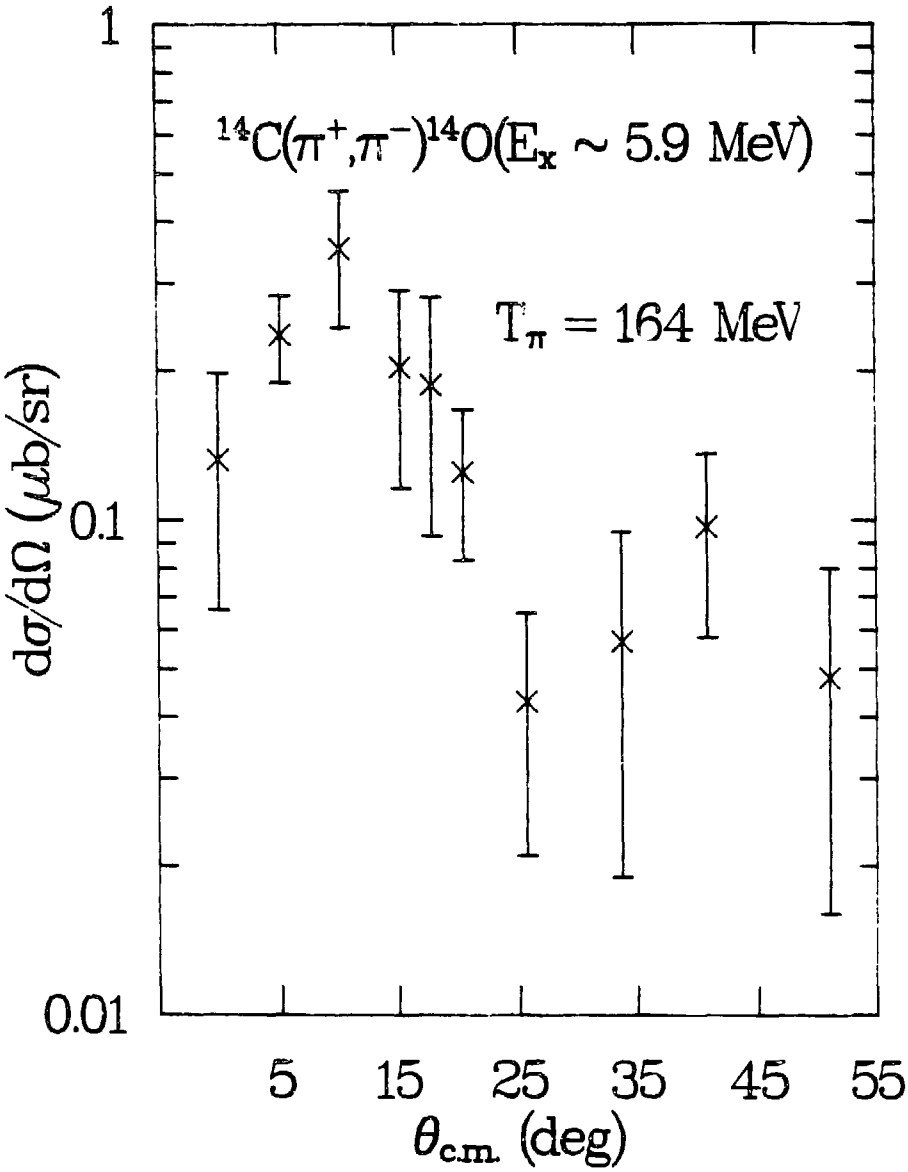

Fig. IV-8: Angular distribution for a 0.5-MeV region centered about the $^{14}O(0^+, 5.92$ MeV) state.

2. $^{14}C(\pi^+,\pi^-)^{14}O(2^+, 7.77\ MeV)$

The $^{14}C(\pi^+,\pi^-)^{14}O(2^+, 7.77\ MeV)$ excitation function is compared to that for the $^{18}O(\pi^+,\pi^-)^{18}Ne(2^+, 1.89\ MeV)$ reaction in Fig. IV-9. Both reactions exhibit a minimum near $T_\pi = 150$ MeV, and are otherwise constant over the energy range measured. The angular distribution at $T_\pi = 292$ MeV (see Fig. IV-10) is flat, and consistent with the expectation that the shape should be determined by a linear combination of $J_0(qR)$ and $J_2(qR)$. The suppression of the cross section near 150 MeV may be connected to the dynamics that create the anomalous 164 MeV angular distributions for the DIAS transitions (see Fig. IV-3), as well as the peaking of nonanalog $0^+ \rightarrow 0^+$ cross sections in that energy region. Unfortunately, the statistical uncertainty of the $^{14}C(\pi^+,\pi^-)^{14}O(2^+)$, 164-MeV angular-distribution data prevent the determination of a forward angle minimum.

3. $^{13}C(\pi^+,\pi^-)^{13}O$

Two spectra, containing all data collected with the thick target at $T_\pi = 164$ and 292 MeV, are shown in Fig. IV-11. The onset of particle instability -- $^{12}N + p$ and $^{11}C + 2p$ above $E_x = 1.53$ and 2.12 MeV, respectively -- is evident in the spectra. Little else is known about the nuclear structure of ^{13}O. The $T_\pi = 164$ MeV spectrum shows evidence for an excited state at $E_x = 2.75 \pm 0.04$ MeV, in agreement with the ^{13}O spectrum measured with the $^{12}C(p,\pi^-)^{13}O$ reaction [Co-78], where a state has been observed at 2.82 ± 0.04 MeV.

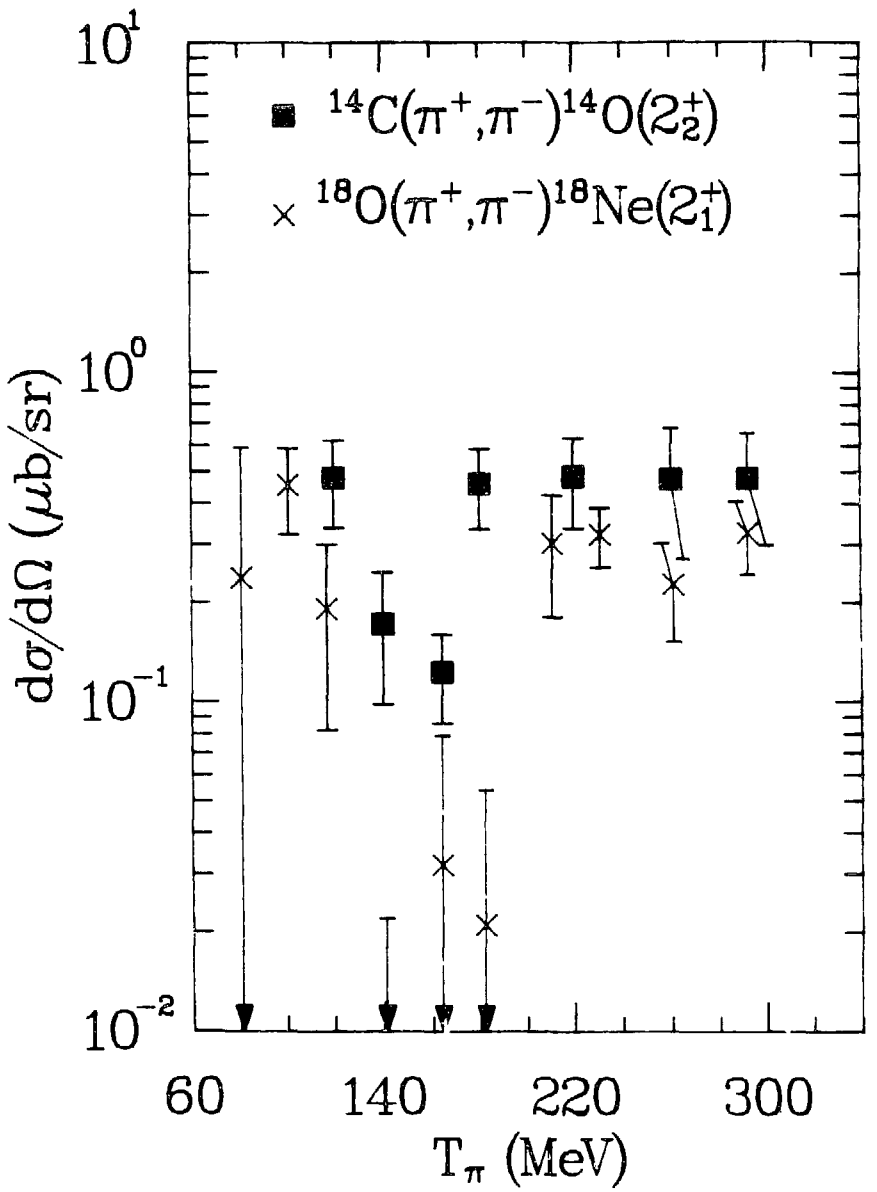

Fig. IV-9: Excitation function for $^{14}C(\pi^+,\pi^-)^{14}O(2^+, 7.77\ MeV)$ is compared to that for the $^{18}O(\pi^+,\pi^-)^{18}Ne(2^+, 1.89\ MeV)$ reaction [Gr-82a].

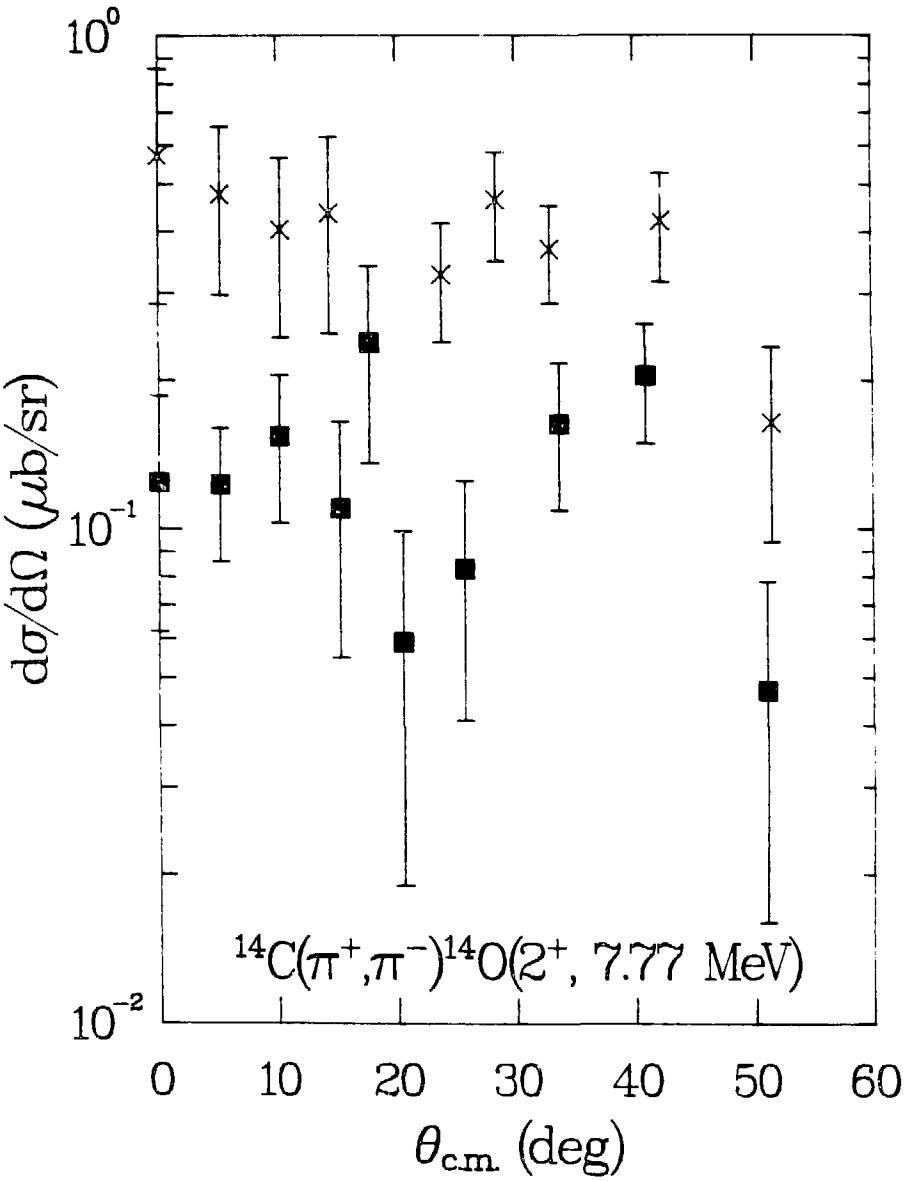

Fig. IV-10: Angular distribution for $^{14}C(\pi^+,\pi^-)^{14}O(2^+, 7.77$ MeV) at T_π = 292 MeV (crosses) and 164 MeV (squares).

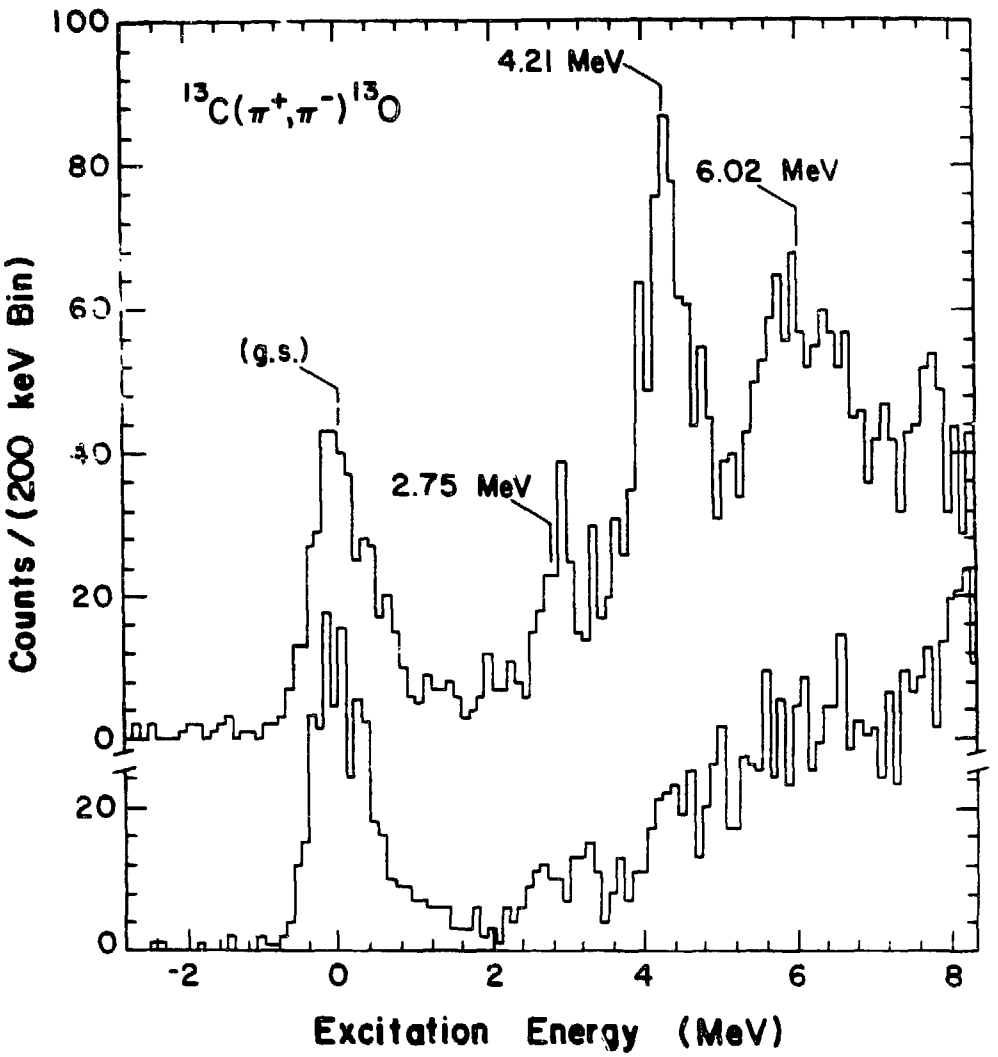

Fig. IV-11: Missing mass spectra for $^{13}C(\pi^+,\pi^-)^{13}O$ at T_π = 164 MeV (top) and 292 MeV (bottom), measured with the target of areal density 1489 mg/cm^2. The spectra are the raw number of counts summed over all angles for which data were taken and are not corrected for spectrometer acceptance as a function of outgoing pion momentum.

The (π^+,π^-) 164 MeV spectrum shows an enhancement at 6.02 ± 0.08 MeV, with a FWHM of 1.2 MeV and may be due to the excitation of more than one state. A state at 4.21 ±0.05 MeV is the only one to have a large enough cross section and a sufficiently narrow width to facilitate the extraction of an angular distribution -- the existence of the continuum background prevents a reliable determination of peak areas for the more weakly excited states. There is no evidence for any of these excited states in the 292 MeV spectrum.

The excitation functions for $^{13}C(\pi^+,\pi^-)^{13}O(gs)$, and $^{13}C(\pi^+,\pi^-)^{13}O(4.21\ MeV)$ are shown in Fig. IV-12. The $^{13}O(g.s.)$ excitation function decreases by a factor of 2.5 between 119 and 180 MeV and the new datum at 180 MeV agrees well with the previous measurement of [Bu-80]. The cross sections at T_π = 164 and 292 MeV are roughly equal, in contrast to the excitation function for the only other nonanalog DCX measurement on a T = 1/2 target [Bu-80, Se-80], $^9Be(\pi^+,\pi^-)^9C(g.s.)$, which monotonically decreases by a factor of 8 between T_π = 140 and 295 MeV. In a simple shell model, the $^9Be(\pi^+,\pi^-)^9C(g.s.)$ reaction can proceed via $\nu(p_{3/2})^3\pi(p_{3/2})^2 \rightarrow \nu(p_{3/2})^1\pi(p_{3/2})^4$, while the $^{13}C(\pi^+,\pi^-)^{13}O(g.s.)$ reaction must necessarily change the orbits of nucleons. In the latter reaction the relatively large cross section at T_π = 292 MeV is a feature common to the nonanalog ΔJ = 2 DCX excitation functions discussed above, while the $^9Be(\pi^+,\pi^-)^9C(g.s.)$ excitation function resembles those for (ground state) to (ground state), ΔJ = 0, nonanalog DCX on T = 0 targets. These features of the data are indicative of interesting nuclear structure or momentum dependence effects.

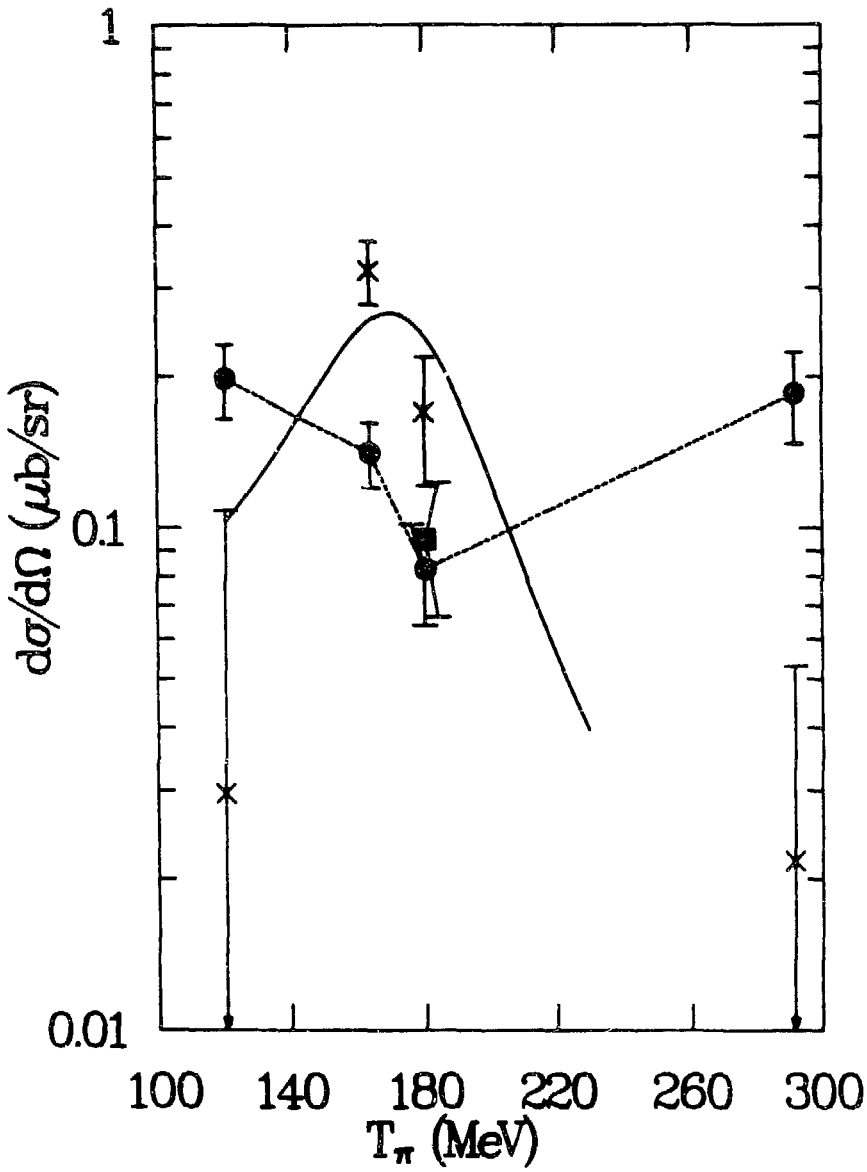

Fig. IV-12: Excitation function for $^{13}C(\pi^+,\pi^-)^{13}O(gs)$ for which the square is from [Bu-80] and circles are from this work. The dashed line serves to guide the eye. The crosses are for $^{13}C(\pi^+,\pi^-)^{13}O(4.21\ MeV)$. The solid line is a Breit-Wigner parameterization of the $^{12}C(\pi^+,\pi^-)^{12}O(gs)$ excitation function [Bl-83], with a width and peak position of 60 MeV and 178 MeV, respectively. The curve has been scaled down to the $^{13}C(\pi^+,\pi^-)^{13}O(4.21\ MeV)$ excitation function.

The excitation function for the E_x = 4.21 MeV state gives only upper limits for the cross sections at 119 and 292 MeV and at 164 MeV exhibits cross sections about twice as large as that of the transition to the ground state. The energy dependence is similar to that measured for $^{12}C(\pi^+,\pi^-)^{12}O$(g.s.) [B1-83] as shown in Fig. IV-12, and $^{14}C(\pi^+,\pi^-)^{14}O(0^+$, 5.92 MeV) (Fig. IV-7).

The 4.21 MeV state cross section at T_π= 164 MeV does not agree with the experimental $A^{-4/3}$ mass dependence of nonanalog DCX on self conjugate targets: $\sigma(5^o)$ for the ^{13}O(4.21 MeV) is 0.50 ± 0.07 times lower than the best fit $A^{-4/3}$ parameterization of the data in [B1-83].

Fig. IV-13 shows the angular distributions for $^{13}C(\pi^+,\pi^-)^{13}O$(g.s.). At 164 MeV, the 0^o and 50^o cross section are roughly a factor of two lower than cross sections for $5^o \leq \theta \leq 40^o$. Other than this feature there is no strong angular dependence. At 292 MeV, $d\sigma/d\Omega$ is roughly constant for $0^o \leq \theta \leq 41^o$, and is decreased at 50^o. We note that for the (ground state) to (ground state) transition, $J_i^\pi = 1/2^-$ and $J_f^\pi = 3/2^-$, which allows for the contribution of ΔJ = 1 and 2 processes in this transition. More than one multipole can also contribute to the $^9Be(\pi^+,\pi^-)^9C$(g.s.) reaction [Se-80], for which the angular distribution at T_π = 162 MeV is slowly varying for $5^o \leq \theta \leq 36^o$, and has a shallow minimum near 22^o. Since the ground state angular distributions for both ^9Be and ^{13}C are not forward peaked, and the excitation functions differ, comparison to 0^+ to 0^+ nonanalog DCX reactions is difficult. Comparisons should be made through angle-integrated cross sections, but existing nonanalog data are limited to $0^o \leq \theta \leq 50^o$.

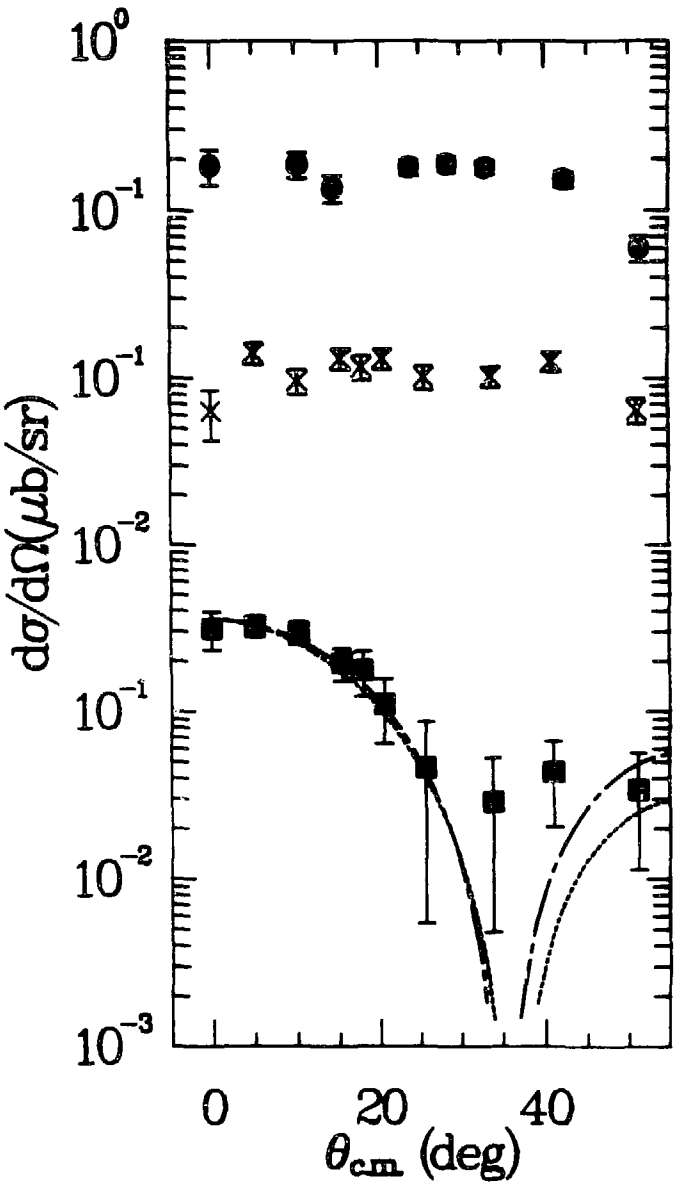

Fig. IV-13: Angular distributions for $^{13}C(\pi^+,\pi^-)^{13}O(gs)$ are similar in shape and magnitude at both 164 (crosses) and 292 MeV (circles). The curves are $\sigma(\theta) = NJ_0^2(qR)e^{-qd}$, fit to the $^{13}C(\pi^+,\pi^-)^{13}O(4.21\ MeV)$ data (squares). The long dashed curve is a best fit to the data: R = 3.0 ± 0.8 fm, d = 0.1 ± 1.1 fm, χ^2 = 0.77, and N = 0.39 μb/sr. The short dashed curve has R = 2.95 fm, d = 0.61 fm, calculated from the two thirds density point of a harmonic oscillator electron scattering parameterization [de-74] of the charge distribution.

The angular distribution (see Fig. IV-13) for the E_x = 4.21 MeV state is clearly forward peaked. The decrease in $d\sigma/d\Omega$ between 0^o and 30^o is similar to that observed for the $^{12}C(\pi^+,\pi^-)^{12}O$(g.s.) reaction [Bl-83] at 164 MeV. The data can be represented by the eikonal form [Am-80] $J_0^2(qR)e^{-qd}$, where q is the momentum transfer, R is a strong absorption radius, and d is the nuclear surface diffuseness. Fig. IV-13 shows curves of damped Bessel functions, one with R and d chosen to best fit the data, the other with R and d ($d = \rho/\rho'$) evaluated at the 2/10 density point of the ^{13}C charge density, calculated from an electron scattering parameterization [de-74]. All nonanalog DCX transitions on T = 0 target nuclei have the transition to the ground state being the strongest transition in the spectrum at forward angles. In the case of $^{13}C(\pi^+,\pi^-)^{13}O$ at 164 MeV, the transition to the 4.21 MeV state dominates at forward angles -- in angular and energy (but not mass) dependence it fits in with nonanalog DCX on self-conjugate target nuclei. The similarities of the $^{12}C(\pi^+,\pi^-)^{12}O$(g.s.), $^{13}C(\pi^+,\pi^-)^{13}O$(4.21 MeV), and $^{14}C(\pi^+,\pi^-)^{14}O$(5.9 MeV) reactions cause us to speculate that the ^{13}O(4.21 MeV) state has $J^\pi = 1/2^-$, thus allowing the reaction to proceed via a $\Delta J = 0$ process. Shell model calculations [Ra-83] using a Cohen-Kurath p-shell effective interaction [Co-65] predict the existence of a $1/2^-$ state at E_x = 4.0 MeV.

V. ANALYSIS OF THE DIAS TRANSITIONS

A. Second Order Optical Potential Phenomenology

This section describes the application of the isobaric-invariant pion-nucleus optical model of Johnson and Siciliano [Jo-83a,b] to T_π = 164 MeV DCX data, and 165 MeV SCX data. Other details of an analysis of elastic, single-, and double-charge-exchange scattering may be found in [Gr-84].

The general form for the π-A optical potential for scattering from T > 1 nuclei is

$$U = U_0 + U_1(\vec{\phi}\cdot\vec{T}) + U_2(\vec{\phi}\cdot\vec{T})^2, \qquad \text{(V-1)}$$

where $\vec{\phi}$ is the isospin operator of the pion and $\vec{T}$ is the isospin operator of the nucleus. U_0, U_1 and U_2 are known as the isoscalar, isovector, and isotensor parts of the optical potential, respectively. The s- and p-wave parts of the interaction may be separated by writing

$$U = -\vec{\nabla}\cdot\xi(\vec{r})\vec{\nabla} + k^2\bar{\xi}(\vec{r}), \qquad \text{(V-2)}$$

where the barred and unbarred quantities, $\bar{\xi}$ and ξ, refer to s- and p-waves, respectively.

$$\xi(\vec{r}) = \xi_0(\vec{r}) + \xi_1(\vec{r})(\vec{\phi}\cdot\vec{T}) + \xi_2(\vec{r})(\vec{\phi}\cdot\vec{T})^2,$$

and similarly for s-waves. By defining

$$\xi^{(j)} \equiv \langle \pi^j;\ T,\ T_z=-T|\xi|\pi^j;\ T,\ T_z=-T\rangle \qquad \text{(V-4)}$$

where T is the nuclear isospin and (j) is the charge state of the pion (+,0,-), the isospin dependence of the lowest order optical potential may be derived. The isovector and isotensor operators can be expressed in terms of isospin raising and lowering operators:

$$(\vec{\phi}\cdot\vec{T}) = \frac{1}{2}(\phi_+T_- + \phi_-T_+ + 2\phi_zT_z)$$

$$(\vec{\phi}\cdot\vec{T})^2 = \frac{1}{4}(\phi_+T_- + \phi_-T_+ + 2\phi_zT_z)^2$$

$$\phi_+\phi_-|\pi^-\rangle = 0, \qquad \phi_+\phi_-|\pi^0\rangle = 2|\pi^0\rangle$$

$$\phi_+\phi_-|\pi^+\rangle = 2|\pi^+\rangle$$

For $(\vec{\phi}\cdot\vec{T})$ only ϕ_zT_z gives non-zero $\xi^{(j)}$, and for $(\vec{\phi}\cdot\vec{T})^2$ only $(\phi_zT_z)^2$ and $(\phi_+T_-\phi_-T_+)$ contribute. Thus one obtains:

$$\xi^{(+)} = \xi_0 - \xi_1T + \xi_2(T^2 + T)$$

$$\xi^{(0)} = \xi_0 + \xi_2T$$

$$\xi^{(-)} = \xi_0 + \xi_1T + \xi_2T^2. \qquad \text{(V-5)}$$

Inverting these equations gives:

$$\xi_2 = \frac{1}{T(2T-1)}(\xi^{(+)} + \xi^{(-)} - 2\xi^{(0)})$$

$$\xi_0 = \xi^{(0)} - \xi_2 T \qquad \text{(V-6)}$$

$$\xi_1 = \frac{1}{T}(\xi^{(0)} - \xi^{(+)}) + \xi_2 T$$

The potential terms may be written in a general way in terms of the neutron and proton densities:

$$\xi^{(i)} = a_n^{(i)}\rho_n(r) + a_p^{(i)}\rho_p(r).$$

ρ_n and ρ_p are normalized to N and Z. Near $T_\pi = 180$ MeV, where the Δ_{33} resonance dominates the π-N scattering amplitude, π-N cross sections are related in a simple way by isospin:

$$\frac{d\sigma}{d\Omega}(\pi^+p\to\pi^+p) = 9\frac{d\sigma}{d\Omega}(\pi^-p\to\pi^-p) = 4\frac{d\sigma}{d\Omega}(\pi^0n\to\pi^0n) = \frac{d\sigma}{d\Omega}(\pi^-n\to\pi^-n). \qquad \text{(V-7)}$$

which implies that $a_n^{(+)} = a_p^{(-)}$ and $a_n^{(-)} = a_p^{(+)}$. Also, since pion scattering from a $T = 0$ nucleus must be independent of the nuclear isospin:

$$a_n^{(-)} + a_p^{(-)} = a_n^{(+)} + a_p^{(+)} = a_n^{(0)} + a_p^{(0)},$$

$$\text{so that } a_n^{(0)} = a_p^{(0)} \equiv \lambda_0^{(1)}. \qquad \text{(V-8)}$$

The isotensor term vanishes in lowest order:

$$\xi_2 = \frac{1}{T(T-1)}(a_n^{(+)}\rho_n + a_p^{(+)}\rho_p + a_p^{(-)}\rho_p$$

$$- 2(a_n^{(0)}\rho_n + a_p^{(0)}\rho_p)) = 0 \qquad \text{(V-9a)}$$

Using Eq. V-8, the isoscalar and isovector p-wave terms become:

$$\xi_0 = \lambda_0^{(1)}\rho(r), \quad \rho(r) \equiv \rho_n(r) + \rho_p(r),$$

$$\xi_1 = \frac{1}{2T}\lambda_1^{(1)}\Delta\rho, \quad \Delta\rho(r) \equiv \rho_n(r) - \rho_p(r). \qquad \text{(V-9b)}$$

So that in lowest order:

$$\xi(r) = \xi_0 + \xi_1(\vec{\phi}\cdot\vec{T}). \qquad \text{(V-9c)}$$

$\lambda_0^{(1)}$ and $\lambda_1^{(1)}$ are expressed in terms of the free π-N scattering amplitudes, $\alpha^{\ell}_{2T,2J}$:

$$\lambda_0^{(1)} = \frac{4\pi}{3\kappa^3 p_1}(4\alpha^1_{33} + 2\alpha^1_{31} + 2\alpha^1_{13} + \alpha^1_{11}) \qquad \text{(V-10a)}$$

$$\lambda_1^{(1)} = \frac{8\pi}{3\kappa^3 p_1}(2\alpha^1_{33} + \alpha^1_{31} - 2\alpha^1_{13} - \alpha^1_{11}). \qquad \text{(V-10b)}$$

The results for the s-wave part of the lowest order optical potential are:

$$\overline{\lambda}_0^{(1)} = \frac{4\pi}{3k\kappa^2} p_1 (a_{31}^0 + a_{11}^0)$$

$$\overline{\lambda}_1^{(1)} = \frac{8\pi}{3k\kappa^2} p_1 (a_{31}^0 - a_{11}^0).$$

$$\overline{\xi}_2(r) = 0$$

κ is the relative π-N center-of-mass momentum, and k is the relative π-A center-of-mass momentum. The π-N amplitudes, $a^{\ell}_{2T,2J}$, are evaluated at the center of mass energy equal to the center-of-mass π-A energy. Thus, s- and p-wave parts have the same form, ie: $\overline{\xi} = \overline{\xi}_0 + \overline{\xi}_1(\vec{\phi}\cdot\vec{T})$. p_1 is a kinematic factor arising from the transformation from the π-N center-of-mass frame to the π-A center-of-mass frame, given by

$$p_1 = \frac{1 + \epsilon}{1 + \epsilon/A}, \quad \epsilon = \omega/M$$

$$\omega = (k^2 + m_\pi^2)^{1/2}$$

and M is the nucleon mass.

In order to accommodate an energy shift in the Δ_{33} channel a^i_{33} is replaced by Ωa^i_{33}, where

$$\Omega = \frac{\omega - \omega_r + i\Gamma}{\omega - (\omega_r + \Delta E_1) + i(\Gamma + \Delta E_2)}$$

$$\omega_r = 1232 \text{ MeV} - (\kappa^2 + M^2)^{1/2}$$

$$\Gamma = \frac{4}{3} \frac{0.08\kappa^3 \omega_r}{m_\pi^2(\kappa^2 + m_\pi^2)^{1/2}}$$

ΔE_1 and ΔE_2 are empirically determined real and imaginary energy shifts obtained by fitting elastic scattering data.

Johnson and Siciliano have derived a form for the isospin and density dependence of the π-A optical potential to second order in density [Jo-83a]. Their result, quadratic in $\Delta\rho$ and ρ, is characterized by five complex parameters that contain the reaction dynamics information of the second order terms. The isospin dependence of the second order terms resembles that of the first order terms. The full optical potential is:

$$U = -\vec{\nabla}\cdot(\xi(r) + \Delta\xi(r))\vec{\nabla} - k^2(\bar{\xi}(r) + \Delta\bar{\xi}(r)).$$

$$- \frac{1}{2}(p_1 - 1)\nabla^2\xi(r) - \frac{1}{2}(p_2 - 1)\nabla^2\Delta\xi(r). \qquad \text{(V-12)}$$

$\Delta\xi(r)$ $(\Delta\bar{\xi}(r))$ are the second order terms. p_2 is a frame transformation factor:

$$p_2 = \frac{1 + \varepsilon/2}{1 + \varepsilon/A}.$$

It is assumed that in the region of $T_\pi = 164$ MeV s-wave contributions to the second order potential are negligible, and thus have been ignored in this analysis. For p-waves the second order terms are:

$$\Delta\xi_0 = \lambda_0^{(2)}\frac{\rho^2(r)}{\rho_0} - \frac{1}{2T-1}\lambda_2^{(2)}\frac{\Delta\rho^2(r)}{\rho_0}. \qquad \text{(V-13a)}$$

$$\Delta\xi_1 = \frac{\lambda_1^{(2)}}{2T}\frac{\rho(r)\Delta\rho(r)}{\rho_0} + \frac{\lambda_2^{(2)}}{2T(2T-1)}\frac{\Delta\rho^2(r)}{\rho_0}. \qquad \text{(V-13b)}$$

$$\Delta\xi_2 = \frac{\lambda_2^{(2)}}{T(2T-1)}\frac{\Delta\rho^2(r)}{\rho_0} + \frac{\lambda_4^{(2)}}{T^2}\frac{\Delta\rho^2(r)}{\rho_0}. \qquad \text{(V-13c)}$$

A similar expression holds for s-waves. $\rho_0 = 0.16\ \text{fm}^{-3}$ is present so that the first and second order parameters have the same (fm^3) units. In [Jo-83a] it is shown that the $\lambda_i^{(2)}$ are weakly dependent on N, Z, and A. However, they are expected to have a strong energy dependence. For the fits to elastic, single and double charge exchange it was assumed that the $\lambda_i^{(2)}$ were independent of N, Z, and A. Since total isospin ($\vec{T} = \vec{T} + \vec{\phi}$) is conserved to a high degree in the strong interaction, the elastic and charge exchange cross sections may be expressed in terms of the scattering amplitudes in the channels $T = T + 1$, $T = T$, and $T = T - 1$. In this scheme the Klein-Gordon equations describing elastic and charge exchange scattering become uncoupled:

$$\begin{aligned}
(-\nabla^2 + U_{T-1})\Psi_{T-1} &= k^2\Psi_{T-1}, \\
(-\nabla^2 + U_T)\Psi_T &= k^2\Psi_T, \\
(-\nabla^2 + U_{T+1})\Psi_{T+1} &= k^2\Psi_{T+1}.
\end{aligned} \qquad \text{(V-14)}$$

The U_T are calculated from

$$(\vec{\phi}\cdot\vec{T}) = \frac{1}{2}(T(T+1) - T(T+1) - 2)$$

$$\text{so for } T = T \qquad \vec{\phi}\cdot\vec{T} = -1,$$

$$\text{and for } T = T+1 \qquad \vec{\phi}\cdot\vec{T} = T, \tag{V-15}$$

$$\text{and for } T = T-1 \qquad \vec{\phi}\cdot\vec{T} = -(T+1).$$

By evaluating U in eq. V-1 between states of total isospin, T, the optical potential in the three isospin channels becomes:

$$U_T = U_0 - U_1 + U_2,$$

$$U_{T+1} = U_0 + TU_1 + T^2U_2, \tag{V-16}$$

$$U_{T-1} = U_0 - (T+1)U_1 + (T+1)^2U_2.$$

The computer code PIESDEX [Jo-83b] is a modification of the elastic scattering code PIRK [Ei-74]. Elastic scattering amplitudes in channels of T are calculated, and linear combinations of these are used to form the $(\pi^{\pm},\pi^{\pm})$, (π^{+},π^{-}), and (π^{+},π^{0}) cross sections. The coulomb interaction is not included in the calculation of the charge exchange amplitudes, but is included for the $\pi^{\pm}$-A elastic amplitudes. PIESDEX is linked to the MINUIT χ^2 optimizing program [Ja-75], which allows the best fit $\lambda_1^{(2)}$, and $\Delta E = \Delta E_1 + i\Delta E_2$ values to be found.

In Eq. V-13c the dynamics of the second order isotensor part of the optical potential is described by two parameters, $\lambda_2^{(2)}$ and $\lambda_4^{(2)}$. $\lambda_2^{(2)}$ contains the sequential scattering of the pion by two correlated nucleons through all non-analog intermediate states and the single analog intermediate state. The latter, however, is already included in the iteration of the lowest order optical potential (Eq. V-9d). To prevent double counting of two sequential charge exchanges through the intermediate single analog state, the $\lambda_4^{(2)}$ term subtracts this channel from the $\lambda_2^{(2)}$ term. $\lambda_4^{(2)}$ is calculated theoretically for a given energy shift ΔE from Eq. 5.37 of [Jo-83a].

The fitting procedure was as follows: ρ and $\Delta\rho$ (the valence neutron density) are Hartree-Fock densities of the Skyrme III effective interaction [Be-75], and contain the nuclear structure information. The energy shift and second order isoscalar parameter $\lambda_0^{(2)}$ were obtained by fitting elastic scattering data for ^{16}O [In-78], ^{28}Si [Ol-80], and ^{40}Ca [In-78]. The results of fitting the elastic scattering data are:

$$\Delta E = 35.0 + 0.3i \text{ MeV}$$

$$\lambda_0^{(2)} = 0.75 + 3.67i \text{ fm}^3. \qquad \text{(V-17)}$$

The total reduced $\chi^2 = 20$. The calculated value of $\lambda_4^{(2)}$ is

$$\lambda_4^{(2)} = 2.89 - 1.13i \text{ fm}^3. \qquad \text{(V-18)}$$

The energy shift raises the resonance by 35 MeV and broadens it slightly.

$\lambda_1^{(2)}$ and $\lambda_2^{(2)}$ were determined by simultaneously fitting the 0^o SCX and 5^o DCX data in Table V-1. The results of fitting this forward angle data with the values of ΔE, $\lambda_0^{(2)}$, and $\lambda_4^{(2)}$ above are

$$\lambda_1^{(2)} = 7.71(\pm 1.96) + 15.51(\pm 0.89)\ \text{fm}^3,$$
$$\lambda_2^{(2)} = 1.66(\pm 2.12) + 10.8(\pm 0.5)\ \text{fm}^3, \qquad \text{(V-19)}$$

Table V-1: DCX and SCX [Sen-83] center-of-mass cross sections input to the PIESDEX fits.

(π^+,π^-), T_π = 164 MeV Target	$d\sigma/d\Omega(5^o)$ (μb/sr)	(π^+,π^o), T_π = 165 MeV Target	$d\sigma/d\Omega(0^o)$ (mb/sr)
^{14}C	1.00 ± 0.10[a]	^{7}Li	4.03 ± 0.60
^{18}O	0.976 ± 0.112[b]	^{13}C	1.80 ± 0.33
^{26}Mg	0.242 ± 0.097	^{14}C	2.37 ± 0.36
^{42}Ca	0.138 ± 0.039[c]	^{15}N	1.20 ± 0.40
^{48}Ca	0.635 ± 0.182[d]	^{18}O	1.91 ± 0.42
^{56}Fe	0.032 ± 0.018	^{60}Ni	0.87 ± 0.09
		^{90}Zr	0.89 ± 0.09
		^{120}Sn	1.87 ± 0.14
		^{140}Ce	1.33 ± 0.15
		^{208}Pb	1.80 ± 0.48

a As reported in [Se-84].
b [Gr-81].
c [Mi-81].
d Interpolated from the data in [Ka-84].

with reduced $\chi^2 = 3.3$. The errors correspond to an increase of the total χ^2 of one. For the purposes of comparing to the phenomenologically determined second second order parameters, the first order parameters are

$$\lambda_0^{(1)} = 4.64 + 5.43i \text{ fm}^3,$$

$$\lambda_1^{(1)} = 5.12 + 5.41i \text{ fm}^3,$$

for ^{18}O at $T_\pi = 164$ MeV. Note that $\lambda_0^{(2)}$, $\lambda_1^{(2)}$, and $\lambda_2^{(2)}$ are roughly the same size as the single scattering terms and thus significantly alter the SCX and DCX amplitudes from the lowest order results.

To show how the $\lambda_1^{(2)}$ contribute to the scattering amplitude, the lowest order scattering amplitude $F(\theta)$ ($\lambda_1^{(2)} = 0$, $\Delta E = 0$), is shown in Fig. V-1a for $^{26}Mg(\pi^+,\pi^-)^{26}Si(DIAS)$, and the contributions, $F^{(2)}(\theta)$, made to the scattering amplitude by the $\lambda_1^{(2)}$ are shown in Fig. V-1b. The task presented to the second order order theory is that the forward angle DCX data are described fairly well by the lowest order calculations, but the forward angle SCX data are underestimated by a factor of two to four in lowest order calculations. SCX cross sections are most sensitive to $\lambda_1^{(2)}$, while DCX cross sections are sensitive to both $\lambda_1^{(2)}$ and $\lambda_2^{(2)}$. The effect of $\lambda_1^{(2)}$ is to add coherently to the lowest order amplitude for SCX and thus reproduces the trend of the A-dependence in Fig. V-2. In the case of DCX at forward angles, the effect of $\lambda_1^{(2)}$ and $\lambda_2^{(2)}$ cancel each other, and the forward angle data are well reproduced in Fig. V-3. Angular distributions calculated with the phenomenologically

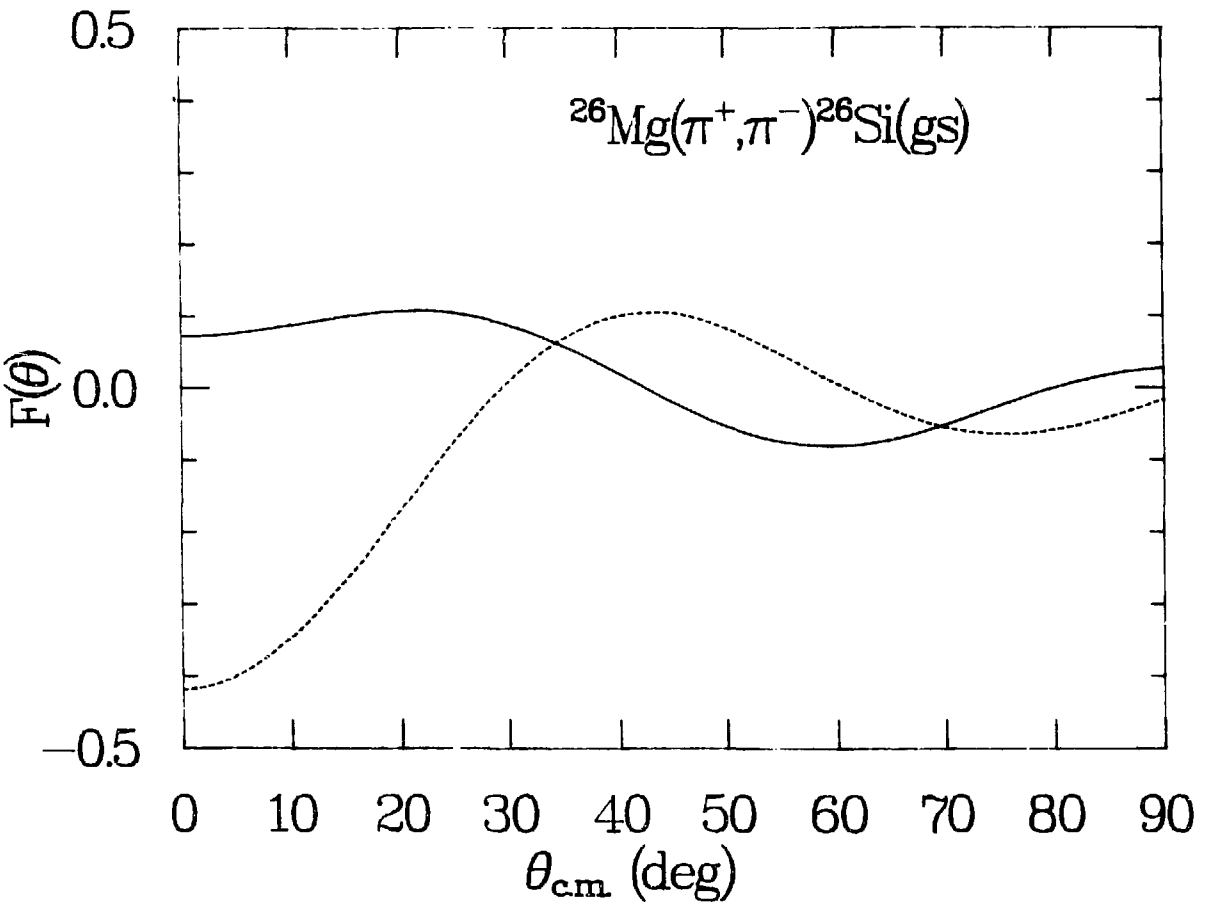

Fig. V-1a: Real (solid line) and imaginary (dashed line) parts of the lowest order ($\lambda_2^{(2)}$ = 0, ΔE = 35.0 + 0.3 MeV) scattering amplitude for $^{26}Mg(\pi^+,\pi^-)^{26}Si$(DIAS), in $\sqrt{\mu b/sr}$.

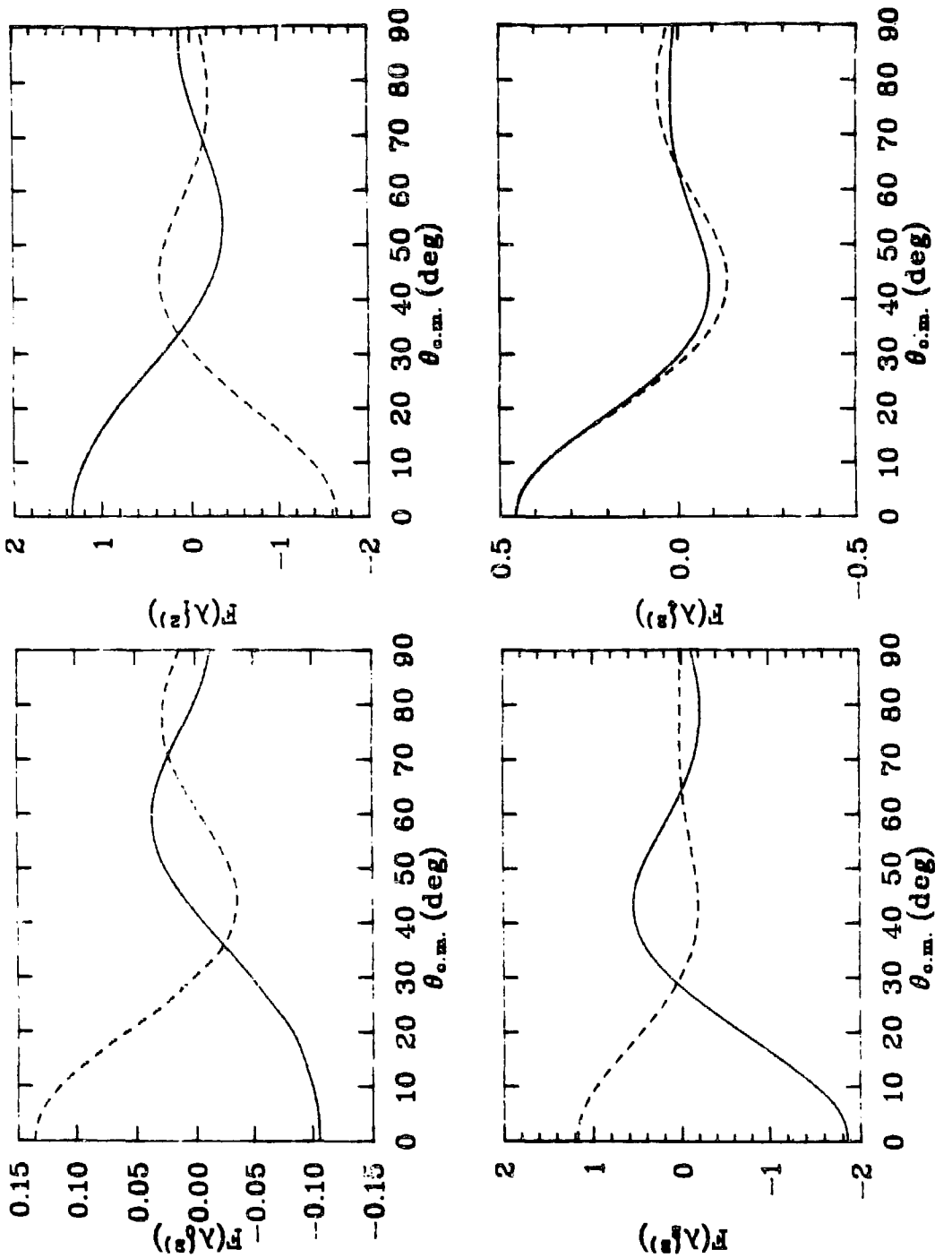

Fig. V-1b: Real (solid lines) and imaginary (dashed lines) contributions to the scattering amplitude from the $\lambda_i^{(2)}$ terms of Eq. V-17,18,19, in $\sqrt{\mu b/sr}$.

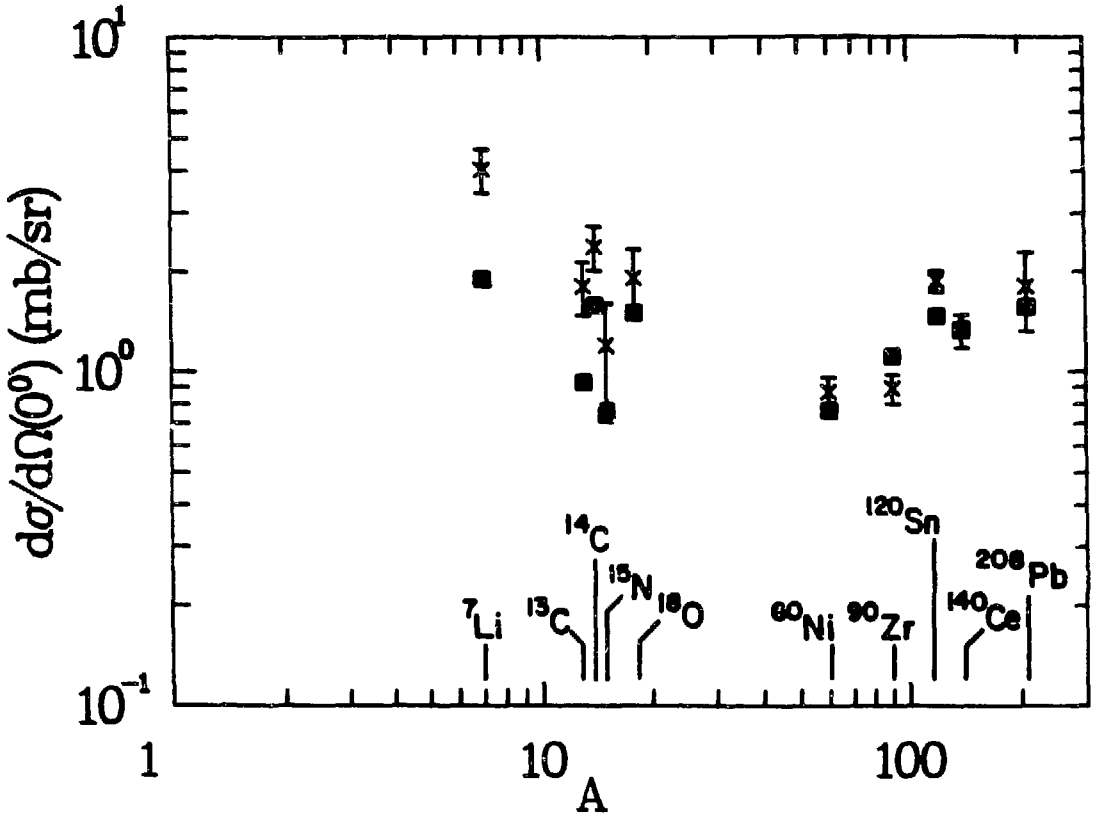

Fig. V-2: Comparison of forward angle SCX differential cross sections (crosses) to the PIESDEX results (squares).

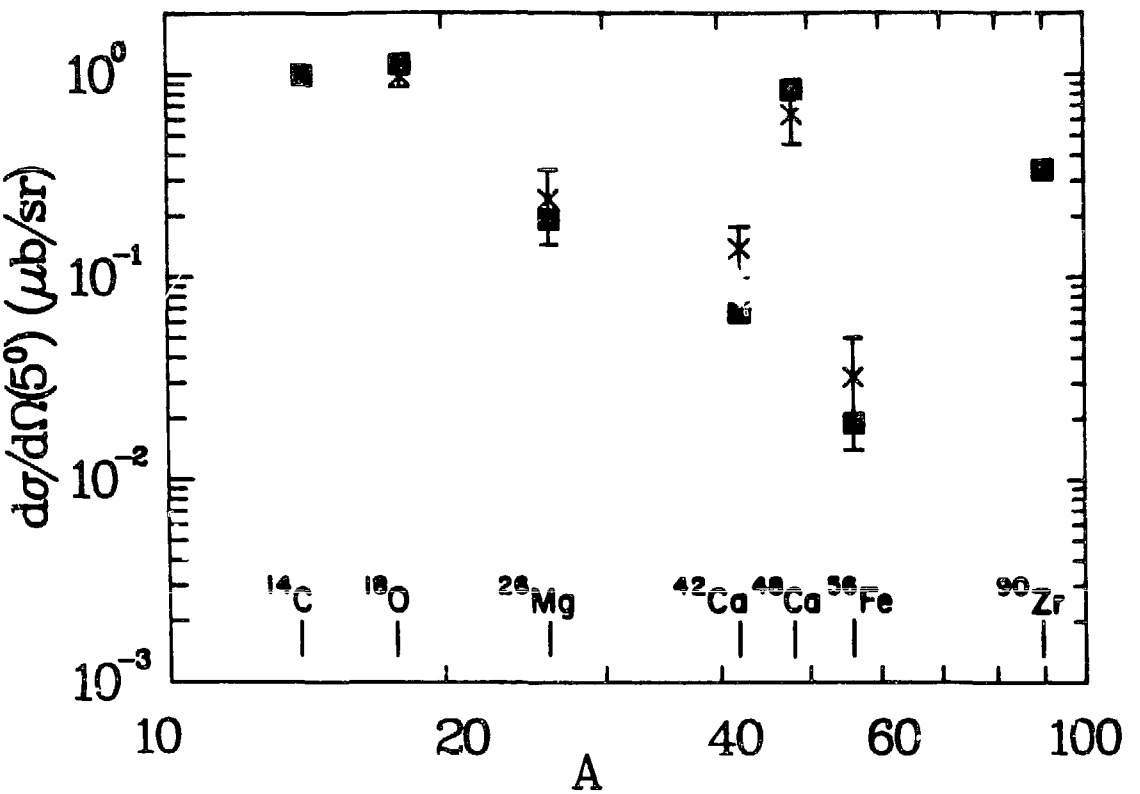

Fig. V-3: Comparison of forward angle DCX differential cross sections (crosses) to the PIESDEX results (squares). The ^{90}Zr point is a prediction.

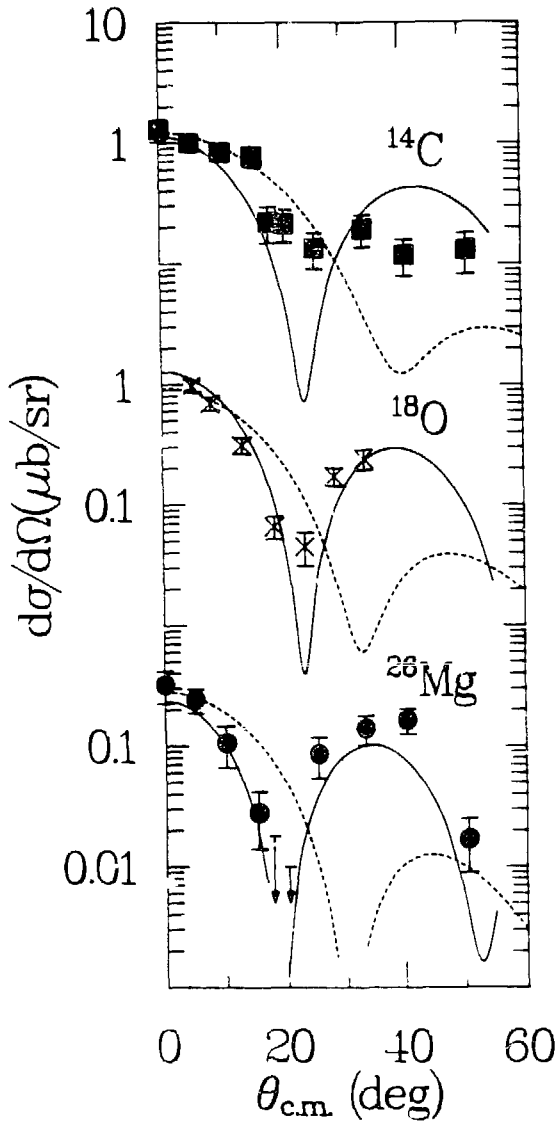

Fig. V-4: Comparison of DCX data at T_π = 164 MeV to the isobaric invariant model PIESDEX calculations. The dashed curve is the lowest order result ($\lambda_1^{(2)}$ = 0, ΔE = 0). The solid curve is the result of fitting only forward angle SCX, DCX data and elastic scattering angular distributions for ^{16}O, ^{28}Si, and ^{40}Ca.

determined parameters for the second order potential are shown in Fig. V-4. For the DCX angular distributions the effect of $\lambda_2^{(2)}$ is to move the minimum predicted in the lowest order calculation from qR = 2.7 to qR = 1.7 fm^{-1}, in agreement with the ^{18}O and ^{26}Mg data. In the case of ^{14}C, the shallow minimum at 164 MeV remains enigmatic.

The dependence of the charge exchange angular distributions on the particular form of the densities used is shown in Fig. V-5 for ^{13}C and ^{15}N SCX data at 165 MeV [Do-82], and for DCX on ^{14}C in Fig. V-6. The fact that the valence neutron density at the ~0.1 density point is larger for DME densities than for Skyrme III densities is reflected in a proportional increase in the cross sections at forward angles, since SCX cross sections are roughly proportional to $(\Delta\rho/\rho)^2$, while DCX cross sections are proportional to $(\Delta\rho/\rho)^4$. This strong density dependence shows the need to correctly describe the nuclear structure in ρ and $\Delta\rho$, in order to successfully separate it from the reaction dynamics information contained in the $\lambda_1^{(2)}$. It is stressed that the success of this rests on the assumption that Skyrme-III Hartree-Fock densities adequately describe nuclear structure for the purposes of (π^+,π^-) and (π^+,π^0) calculations.

The effect of π-Δ_{33} and ρ-Δ_{33} interactions on the $^{18}O(\pi^+,\pi^-)^{18}Ne$(DIAS) excitation function have been investigated in [Jo-84]. In that work, the authors found large contributions to the cross sections for the sequence of processes: $\pi^+n \rightarrow \Delta^+$, $\Delta^+n \rightarrow \Delta^0p$, $\Delta^0 \rightarrow \pi^-p$. The calculated DCX cross section, however, is generally too large and reproduces the excitation function only for $T_\pi \lesssim 100$ MeV.

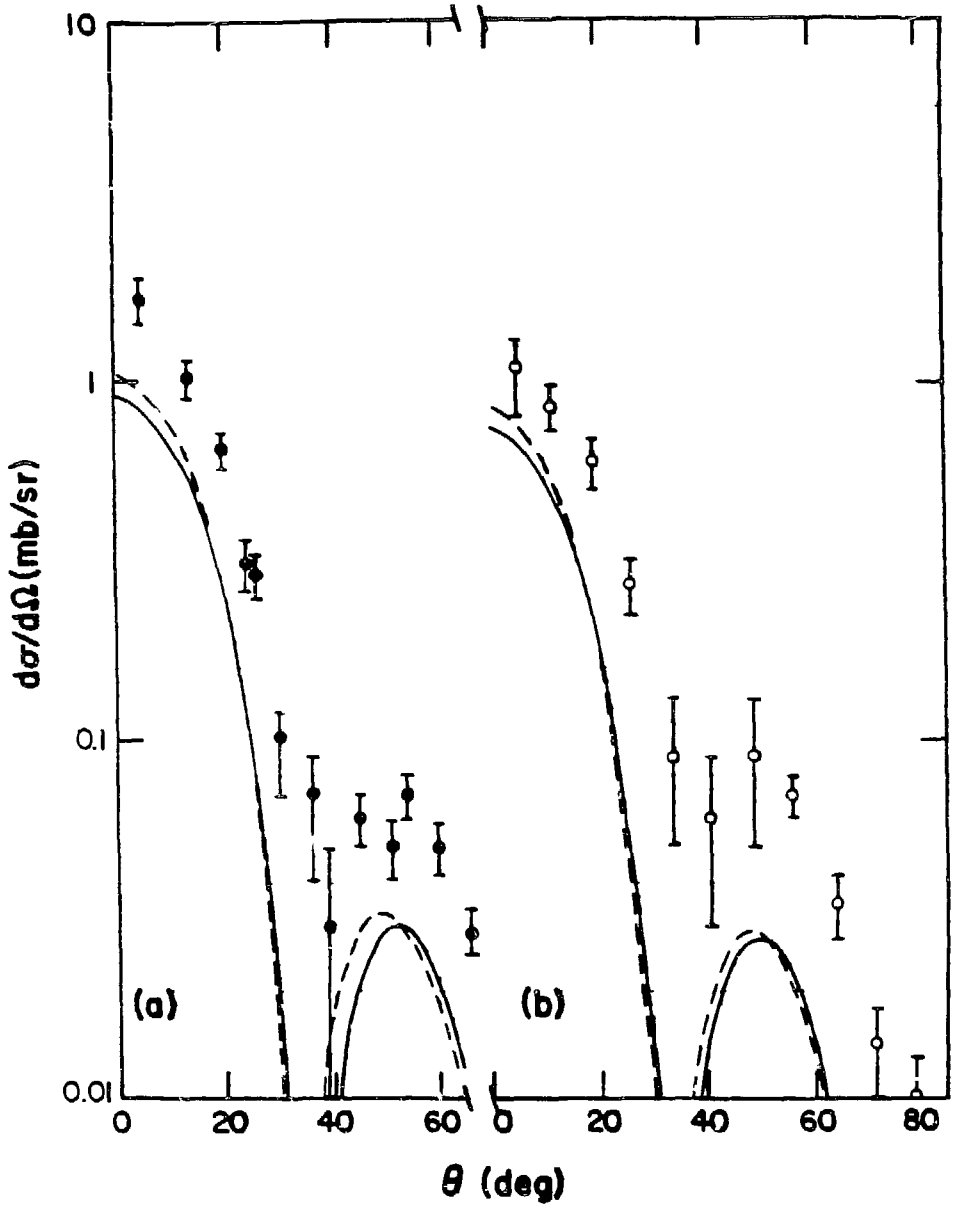

Fig. V-5: Calculations for (a): $^{13}C(\pi^+,\pi^0)^{13}N$, and (b): $^{15}N(\pi^+,\pi^0)^{15}O$ data with $\lambda_1^{(2)}$ and ΔE from Eq. V-17, 18, 19. The dashed lines are for Skyrme-III Hartree-Fock densities and the solid lines are for Negele-Vautherin DME densities [Ne-72].

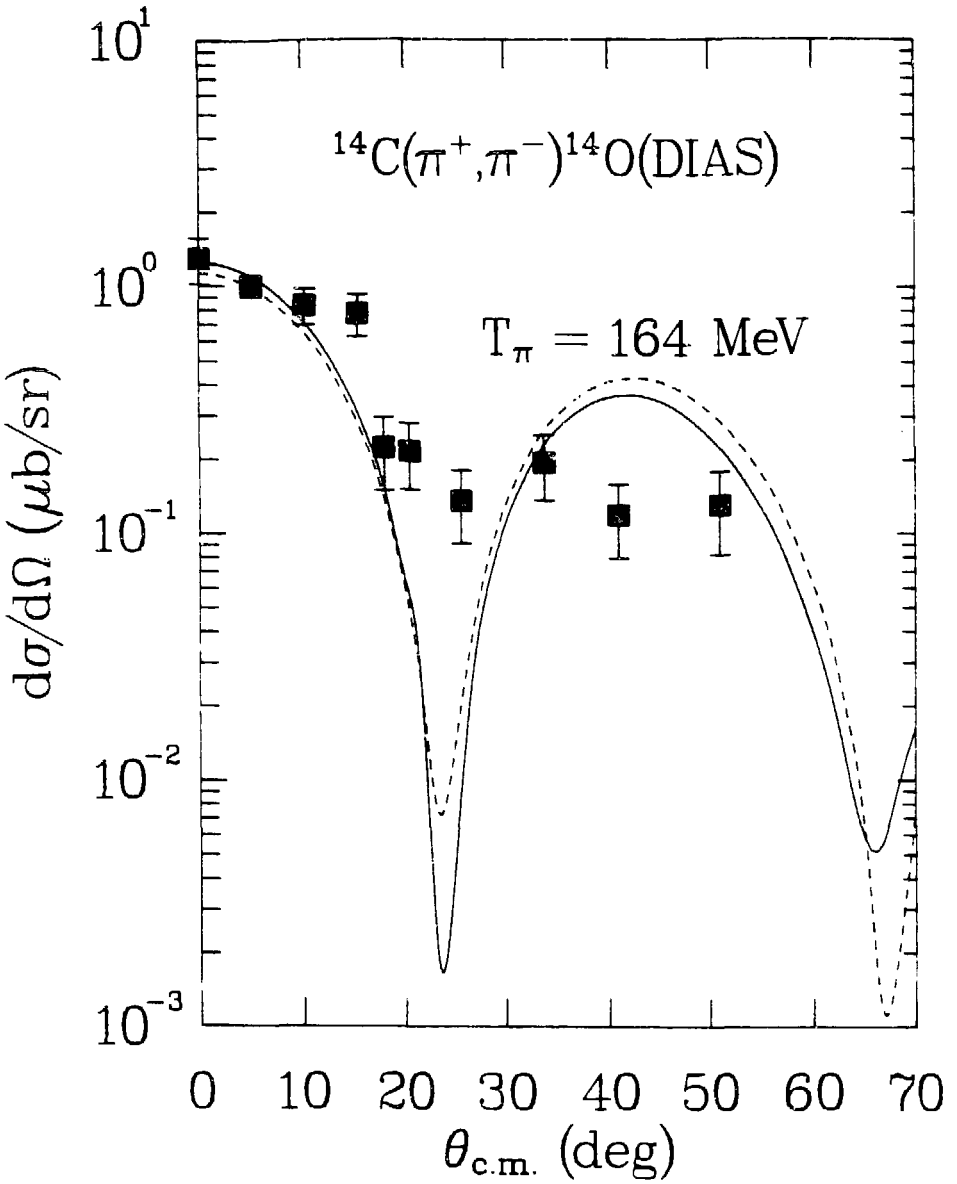

Fig. V-6: Calculations for $^{14}C(\pi^+,\pi^-)^{14}O(DIAS)$ with $\lambda_1^{(2)}$ and ΔE from Eq. V-17, 18, 19. The dashed line is for a Skyrme-III Hartree-Fock density and the solid line is for a Negele-Vautherin DME density [Ne-72].

Contributions from this and other exotic Δ-nuclear effects may be contributing to the rather large second order terms obtained from the phenomenological fits discussed here. The energy dependence of these $\lambda_1^{(2)}$ can be determined by fitting elastic and charge exchange data at several energies. Such an effort could guide theoretical efforts to microscopically describe second order contributions to the π-A interaction.

B. Second Order Optical Potential and Core Excitation

A coupled channels approach to DCX has been applied by Liu to the $^{18}O(\pi^+,\pi^-)^{18}Ne$(DIAS) [Li-83] and $^{42}Ca,^{48}Ca(\pi^+,\pi^-)^{42}Ti,^{48}Ti$(DIAS) reactions [Set-84, Ka-83]. The details of this theory are described in [Li-83], where the $^{18}O(\pi^+,\pi^-)^{18}Ne$(DIAS) excitation function data and angular distribution data at T_π = 164 and 292 MeV are well reproduced by a pion-nucleus interaction that includes the effect of pion absorption. Core-excitation wave functions were used to describe the structure of ^{18}O. In this section the application of this theory to the $^{14}C(\pi^+,\pi^-)^{14}O$(DIAS) data is described [Li-84b].

Through isospin coupling, the charge exchange matrix elements are linearly related to the isoscalar, isovector, and isotensor parts of the π-A strong interaction,

$$U_s = U_0 + U_1(\vec{\phi}\cdot\vec{T}) + U_2(\vec{\phi}\cdot\vec{T})^2.$$

U_0, U_1 and U_2 are also expressed in terms of optical potentials for

$^{14}C(\pi,\pi)^{14}C$ elastic scattering. Thus, the $\pi^{(i)}$-^{14}C (i = +, 0, -) optical potential and the ^{14}C wave functions are the necessary input to the DCX calculations.

The first order optical potentials, $U^{(1)}_{opt,i}$ are proportional to $t_{\pi N}(E)\rho(r)$, where $t_{\pi N}(E)$ is the free π-N t-matrix, and $\rho(r)$ is the nuclear density. Binding energies for core and valence nucleons are taken into account in the determination of the energy E at which $t_{\pi N}$ is evaluated.

The second order terms are more complicated and are determined for a specific second order reaction mechanism, namely the absorption and emission of a pion by a pair of nucleons. The strength of these terms is calculated from a study of π-^{12}C elastic scattering data, and an "isospin scaling model" is used to obtain the $U^{(2)}_{opt,i}$ for π-^{14}C scattering from that of the ^{12}C-system. In principle, the second order terms could be obtained directly from π-^{14}C elastic scattering data, however, such data is limited, existing only for T_π = 162 MeV. This procedure of obtaining the second order potential terms from neighboring nuclei provided good fits to $^{18}O(\pi,\pi)^{16}O$ elastic scattering data in [Li-83]. It is because the ^{14}C, ^{14}N(IAS), and ^{14}O(DIAS) wave functions have identical space-spin parts that only the nuclear structure of ^{14}C(gs) need be known. A p-shell configuration mixed wave function was used [Co-65]:

$$|^{14}C\rangle = |^{16}O\rangle \otimes |2h\rangle$$

$$\text{where} \quad |2h\rangle = -0.4053|(1p^{-1}_{3/2})^2\rangle - 0.9142|(1p^{-1}_{1/2})^2\rangle. \qquad \text{(V-20)}$$

$|(1p_{3/2}^{-1})^2\rangle$ and $|(1p_{1/2}^{-1})^2\rangle$ are harmonic oscillator wave functions. DCX cross sections were calculated with a ^{14}C wave function that included an s-d shell admixture [Fo-82] (not shown in this work), and provided very similar results to those shown in this section.

The excitation function calculations are shown in Fig. V-7. The final result, which includes the ρ^2-dependent interaction based on pion absorption and emission and the wave function of Eq. V-20, agrees with the data for $T_\pi \geq 180$ MeV, and overestimates the cross section by $\approx$50% for lower energies. A test of this calculation is provided by measuring forward angle cross sections for $T_p \leq 100$ MeV. Agreement with the solid curve would indicate that the $^{14}C(\pi^+,\pi^-)^{14}O$(DIAS) and $^{18}O(\pi^+,\pi^-)^{18}Ne$(DIAS) excitation functions have a similar shape, with the ^{14}C cross section peaked at $T_\pi \approx 70$ MeV, while the ^{18}O data are peaked at $T_\pi \approx 120$ MeV. Recently, measurements of $^{14}C(\pi^+,\pi^-)^{14}O$(gs) at $T_\pi = 50$ MeV give $d\sigma/d\Omega(0^o) = 3.9 \pm 0.5$ μb/sr [Le-84], in excellent agreement with the calculation shown in Fig. V-7.

The 164-MeV ^{14}C angular distribution and calculations are shown in Fig. 8. As in the case of ^{18}O [Li-83], the effect of the ρ^2 dependent terms is to move the first minimum from that found in most lowest order calculations to a smaller angle. However, the lack of a minimum in the data is a feature not reproduced by this, (and not explained by any other) calculation. The inclusion of the nuclear structure information of Eq. V-20 raises the overall cross section, and has only a minor effect on the position of the minimum.

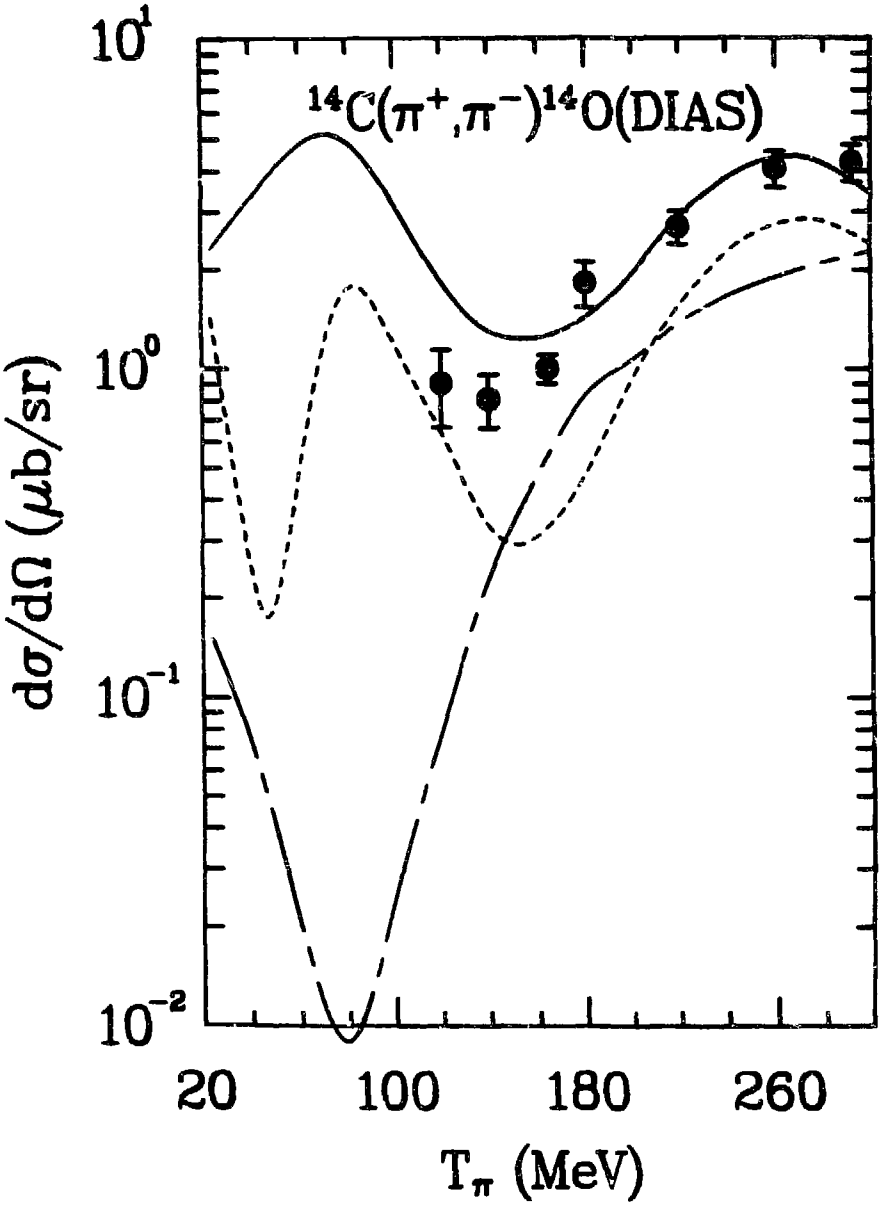

Fig. V-7: DCX coupled channels calculations of L. C. Liu [Li-84]. The long dashed curve includes no second-order optical-potential terms, and uses DME Hartree-Fock wave functions [Ne-72] (no configuration mixing) to describe the nuclear structure of ^{14}C. The short dashed curve includes second-order optical-potential terms and the DME wave functions. The solid curve includes the second-order optical-potential terms and the core-excitation wave function of Eq. V-20.

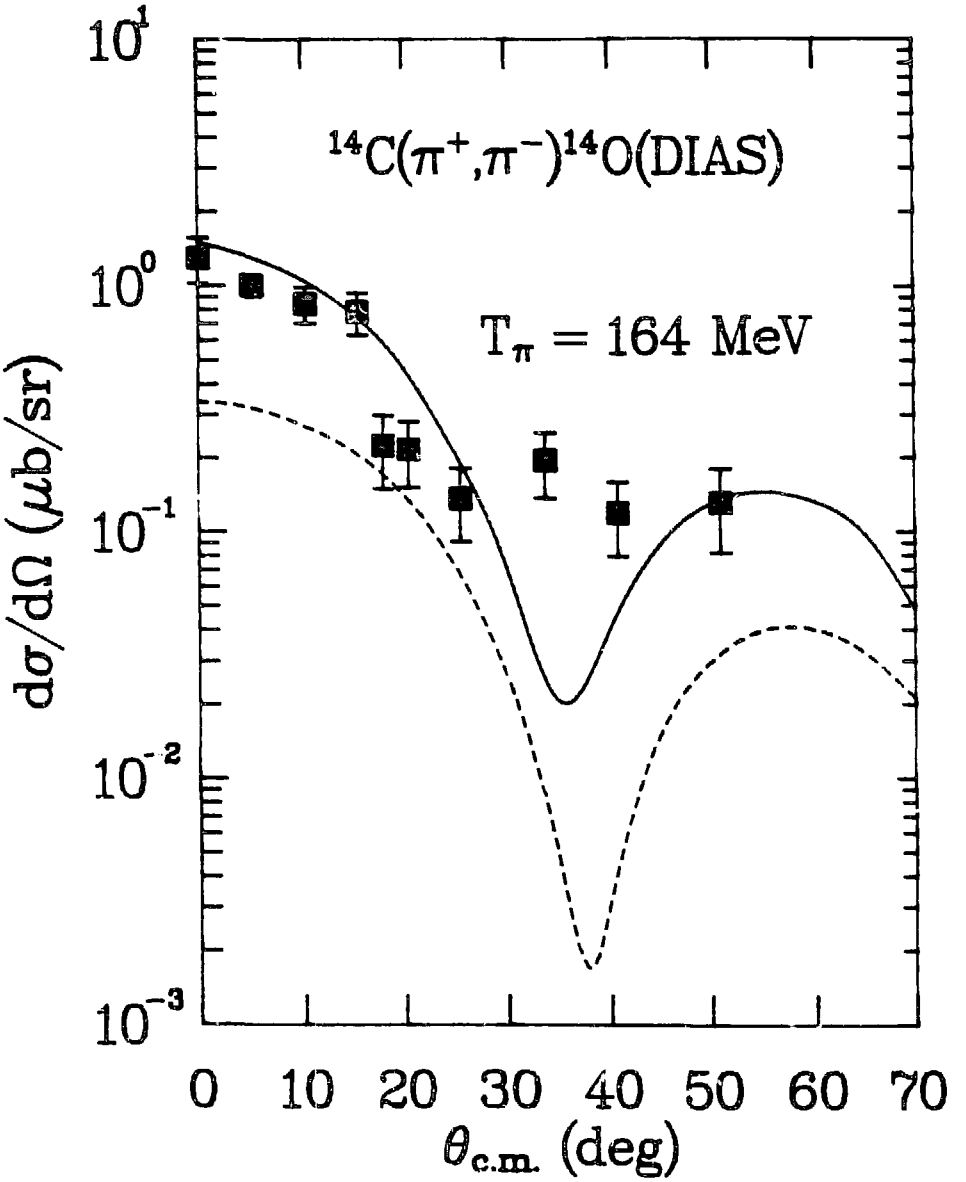

Fig. V-8: At 164 MeV the the decrease of the forward-angle cross is reproduced by the calculation including ρ^2 terms and the core-excitation ^{14}C wave function of Eq. V-20 (solid curve). The dashed curve has the same meaning as in Fig. V-7.

The situation at 292 MeV is shown in Fig. V-9. The ρ^2 terms and nuclear structure have the same general effects on the cross section. The agreement is good, except at 50^{o}, where the datum is one order of magnitude greater than the calculation. It is speculated [Li-84] that this may be due to an inadequate treatment of Fermi motion, which would cause largest error at a momentum transfer comparable to the Fermi momentum, or nuclear structure details not contained in Eq. V-20.

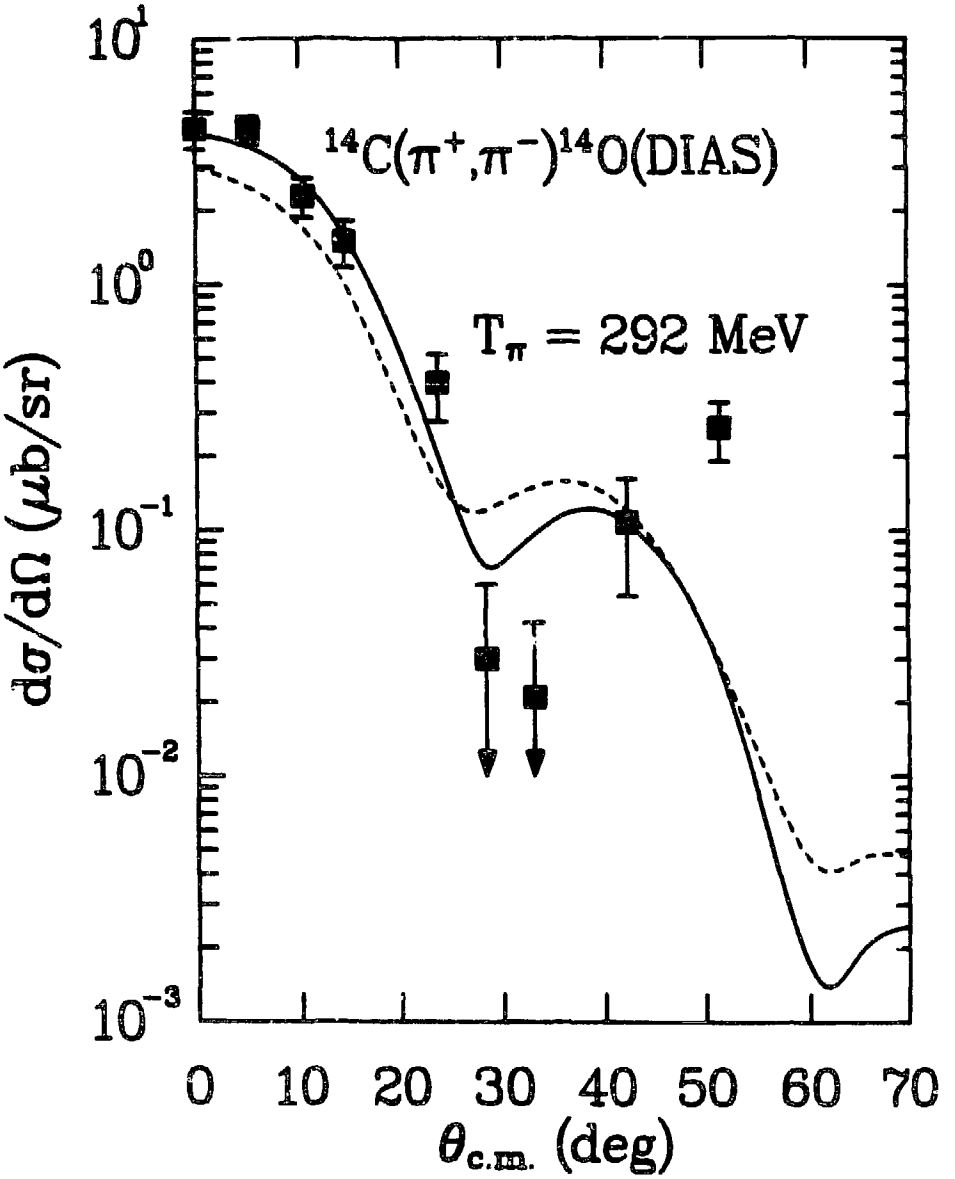

Fig. V-9: Comparison of data and calculations at 292 MeV. The curves have the same meaning as in Fig. V-7.

VI. SUMMARY AND CONCLUSIONS

Over the energy range measured at EPICS ($100 \lesssim T_\pi \lesssim 300$ MeV) there are two types of excitation functions for the DIAS transitions: those which monotonically increase (^{14}C, ^{48}Ti, ^{56}Fe) and those which exhibit local maxima near 140 MeV (^{18}O, ^{26}Mg, ^{42}Ca).

Angular distributions exist only for the T=1 targets ^{14}C, ^{18}O, and ^{26}Mg. At 292 MeV, where the minima appear at $qR \approx 3.5$, the data can be explained by calculations which describe the reaction as sequential charge exchange through the respective intermediate analog states. At 164 MeV the minima are at $qR \approx 1.7$, and the ^{14}C data are roughly constant for larger momentum transfers. These features of the angular distributions are indicative of large second order effects near the Δ_{33} resonance energy.

In Chapter V it was shown that in the model of Johnson and Siciliano, large two nucleon (ρ^2) terms are needed to fit the data. The significance of the results are that one set of isoscalar, isovector, and isotensor parameters are able to describe the mass and angular dependence of SCX and DCX over a wide range of A. The theory's most obvious failure is the ^{14}C angular distribution.

Within the model of Liu, true pion absorption as well as nuclear structure details are responsible for producing the interest-

ing features of the DIAS data. However, here too the ^{14}C 164-MeV angular distribution is not reproduced by the calculations.

The 164-MeV forward angle data show markedly more deviation (χ^2/point = 7.0 versus 2.5) from the $(N - Z)(N - Z - 1)A^{-10/3}$ mass dependence than at 292 MeV. The excitation functions indicate that the transition to a smoother mass dependence occurs for $T_\pi \geq 200$ MeV.

For the nonanalog transitions studied, those to $^{14}O(0^+$, 5.92 MeV) and $^{56}Ni(gs)$ have similar features to $0^+ \rightarrow 0^+$ transitions on T = 0 target nuclei. (The latter transition is related to DCX on a T = 0 target, $^{56}Ni(\pi^-,\pi^+)^{56}Fe(gs)$, through time-reversal symmetry.) The peaking of the nonanalog excitation functions near T_π = 150 MeV, where the DIAS data exhibit their anomalous behavior is a compelling indication that the reaction mechanism responsible for the nonanalog transitions is interfering with the simple sequential charge exchange mechanism for analog DCX. It is interesting to note that near 164-MeV, in the case of $^{14}C,^{56}Fe(\pi^+,\pi^-)$, these nonanalog $\Delta J = 0$ transitions are almost as strongly excited as the DIAS transitions, establishing a connection between the monotonic type of DIAS excitation function and the existence of a strong, low-lying, $0^+ \rightarrow 0^+$ nonanalog transition. No such nonanalog transitions are seen in the $^{18}O(\pi^+,\pi^-)$ and $^{26}Mg(\pi^+,\pi^-)$ spectra. Thus, an accurate theoretical description of analog DCX requires understanding DCX on T = 0 target nuclei, since an approximate description of the T = 1 nuclei studied is a T = 0 core coupled to two neutrons. Such a unified treatment would need to reproduce the observed mass dependences for nonanalog ($A^{-4/3}$) and analog transitions.

The $^{14}C(\pi^+,\pi^-)^{14}O(2^+, 7.77\ MeV)$ data have shown the beginnings of systematic behavior for transitions to 2^+ states. The minimum near 140 MeV and the relatively large cross sections near 300 MeV are common to both the $^{14}C(2^+, 7.77\ MeV)$ data and the $^{18}Ne(2^+, 1.89\ MeV)$ data (see also Appendix B).

The $^{13}C(\pi^+,\pi^-)^{13}O(gs)$ angular distributions vary slowly between 0^o and 50^o. The forward-angle excitation function distinguishes itself from other nonanalog DCX (ground state) to (ground state) transitions in that the excitation function is not peaked near 160 MeV. The transition to the $E_x = 4.21$ MeV state exhibits features common to $\Delta J = 0$ nonanalog DCX reactions. The excitation function is peaked near 160 MeV and the angular distribution at 164 MeV has a simple diffractive shape, with a minimum consistent with the strong absorption radius. These features suggest that $J^\pi = 1/2^-$ for this state.

Measurements of analog DCX angular distributions for $T > 1$ nuclei are needed to investigate the isospin dependence of the reaction, and test the isospin parameterization of the second-order π-nucleus interaction of Johnson and Siciliano. The isospin factors ($\propto T^{-1}$, T^{-2}) in Eq. V-13 can damp second order contributions to the scattering amplitude, which would be manifest in new interference features.

Recent angular-distribution measurements of the $^{18}O(\pi^+,\pi^-)^{18}Ne(gs)$ reaction at six new energies between 100 and 292 MeV (Appendix B) show that the transition to an anomalous angular distribution shape occurs suddenly over a narrow energy range:

$200 \leq T_{\pi} < 230$ MeV. The striking similarity of the $^{18}O(\pi^+,\pi^-)^{18}Ne(gs)$ angular-distribution shape at 200 MeV to that for $^{14}C(\pi^+,\pi^-)^{14}O(gs)$ at 164 MeV, along with the shapes of the excitation functions suggest that the two reactions possess identical features, but are shifted by ~40 MeV with respect to each other.

APPENDIX A

TABULATION OF DATA FOR EXPERIMENT 558

Table A-1: Center-of-mass cross sections for $^{14}C(\pi^+,\pi^-)^{14}O$(DIAS).

T_π = 164 MeV		T_π = 292 MeV		θ_{lab} = 5°	
θ_{lab} (deg)	$d\sigma/d\Omega$ (μb/sr)	θ_{lab} (deg)	$d\sigma/d\Omega$ (μb/sr)	T_π (MeV)	$d\sigma/d\Omega$ (μb/sr)
0	1.38±0.29	0	4.54±0.79	120	0.959±0.257
5	1.06±0.11	5	4.51±0.59	140	0.857±0.160
10	0.893±0.150	10	2.42±0.45	164	1.06±0.11
15	0.828±0.160	14	1.58±0.35	180	1.93±0.31
17.5	0.237±0.079	23	0.424±0.131	220	2.88±0.34
20	0.229±0.069	27.5	0.032±0.032	260	4.34±0.55
25	0.144±0.048	32	0.022±0.022	292	4.51±0.59
33	0.207±0.062	41	0.114±0.057		
40	0.126±0.042	50	0.277±0.076		
50	0.139±0.052				

Table A-2: Center-of-mass cross sections for $^{14}C(\pi^+,\pi^-)^{14}O(0^+, 5.92\ MeV)$.

T_π = 164 MeV		θ_{lab} = 5°	
θ_{lab} (deg)	$d\sigma/d\Omega$ (μb/sr)	T_π (MeV)	$d\sigma/d\Omega$ (μb/sr)
0	0.132±0.066	120	0.215±0.107
5	0.236±0.047	140	0.589±0.134
10	0.352±0.108	164	0.236±0.047
15	0.203±0.087	180	0.259±0.087
17.5	0.187±0.094	220	0.194±0.078
20	0.125±0.042	260	<0.072
25	0.043±0.022	292	<0.061
33	0.057±0.038		
40	0.097±0.039		
50	0.048±0.032		

Table A-3: Center-of-mass cross sections for $^{14}C(\pi^+,\pi^-)^{14}O(2^+, 7.77$ MeV).

T_π = 164 MeV		T_π = 292 MeV		θ_{lab} = 5°	
θ_{lab} (deg)	$d\sigma/d\Omega$ (μb/sr)	θ_{lab} (deg)	$d\sigma/d\Omega$ (μb/sr)	T_π (MeV)	$d\sigma/d\Omega$ (μb/sr)
0	0.124±0.062	0	0.571±0.286	120	0.480±0.144
5	0.123±0.037	5	0.477±0.179	140	0.172±0.074
10	0.154±0.051	10	0.405±0.161	164	0.123±0.037
15	0.110±0.055	14	0.437±0.188	180	0.461±0.126
17.5	0.239±0.103	23	0.328±0.089	220	0.485±0.149
20	0.059±0.040	27.5	0.465±0.116	260	0.475±0.204
25	0.083±0.042	32	0.369±0.083	292	0.477±0.179
33	0.163±0.054	41	0.423±0.105		
40	0.205±0.056	50	0.164±0.070		
50	0.047±0.031				

Table A-4: Center-of-mass cross sections for $^{26}Mg(\pi^+,\pi^-)^{26}Si$(DIAS).

T_π = 164 MeV		θ_{lab} = 5°	
θ_{lab} (deg)	$d\sigma/d\Omega$ (μb/sr)	T_π (MeV)	$d\sigma/d\Omega$ (μb/sr)
0	0.322±0.097	120	0.259±0.078
5	0.242±0.054	164	0.242±0.054
10	0.106±0.040	180	0.206±0.061
15	0.028±0.014		
17.5	≤0.018		
20	≤0.010		
25	0.086±0.032		
33	0.140±0.038		
40	0.164±0.039		
50	0.016±0.008		

Table A-5: Center-of-mass cross sections for $^{56}Fe(\pi^+,\pi^-)^{56}Ni$ at $\theta_{lab} = 5^o$.

T_π(MeV)	$d\sigma/d\Omega$ DIAS, E_x = 9.6 MeV	$d\sigma/d\Omega$(μb/sr) g.s.
140	0.033±0.027	0.075±0.023
164	0.032±0.018	0.053±0.014
220	0.161±0.036	0.014±0.007
260	0.390±0.081	0.014±0.014
292	0.323±0.077	<0.013

Table A-6: Center-of-mass cross sections for $^{13}C(\pi^+,\pi^-)^{13}O(gs)$.

T_π = 164 MeV		T_π = 292 MeV		$\theta_{lab} = 5^o$	
θ_{lab} (deg)	$d\sigma/d\Omega$ (μb/sr)	θ_{lab} (deg)	$d\sigma/d\Omega$ (μb/sr)	T_π (MeV)	$d\sigma/d\Omega$ (μb/sr)
0	0.063±0.021	0	0.184± 0.044	120	0.198±0.034
5	0.141±0.021				
10	0.095±0.016	10	0.187±0.032	164	0.141±0.021
15	0.130±0.019	14	0.135±0.025	180	0.083±0.019
17.5	0.116±0.020	23	0.179±0.019	292	0.185±0.038
20	0.130±0.018	27.5	0.188±0.020		
25	0.102±0.017	32	0.180±0.016		
33	0.104±0.015	41	0.153±0.016		
40	0.127±0.017	50	0.060±0.011		
50	0.065±0.011				

Table A-7: Center-of-mass cross sections for $^{13}C(\pi^+,\pi^-)^{13}O(1/2^-, 4.21$ MeV).

T_π = 164 MeV		θ_{lab} = 5°	
θ_{lab} (deg)	$d\sigma/d\Omega$ (μb/sr)	T_π (MeV)	$d\sigma/d\Omega$ (μb/sr)
0	0.312± 0.080	120	0.030±0.079
5	0.325±0.047	164	0.325±0.047
10	0.297±0.047	180	0.170±0.049
15	0.195±0.043	292	0.022±0.031
17.5	0.177±0.053		
20	0.111±0.046		
25	0.046±0.041		
33	0.029±0.024		
40	0.044±0.023		
50	0.034±0.023		

APPENDIX B

The Energy Dependence of $^{18}O(\pi^+,\pi^-)^{18}Ne(gs)$

This paper (Los Alamos National Laboratory report #LA-UR 84-3373) was submitted to Physical Review Letters in October 1984.

The Energy Dependence of $^{18}O(\pi^+,\pi^-)^{18}Ne(gs)$

Peter A. Seidl, C. Fred Moore, and S. Mordechai[a]
University of Texas at Austin, Austin, TX 78712

R. Gilman, Kalvir S. Dhuga[b], H. T. Fortune, and J. D. Zumbro
University of Pennsylvania, Philadelphia, PA 19104

C. L. Morris
Los Alamos National Laboratory, Los Alamos, NM 87545

J. A. Faucett and G. R. Burleson
New Mexico State University, Las Cruces, NM 88003

ABSTRACT

Eight angular distributions measured for $^{18}O(\pi^+,\pi^-)^{18}Ne(gs)$ across the Δ_{33} resonance show the details of the energy dependence of the reaction. At higher energies, the minimum is at $q = 0.85$ fm^{-1}, in agreement with simple sequential scattering models, but at lower energies it is at $q = 0.5$ fm^{-1}, with the transition occuring over a narrow energy range.

[NUCLEAR REACTIONS: $^{18}O(\pi^+,\pi^-)^{18}Ne$(g.s., $E_x = 1.89$ MeV) $T_\pi = 100$ to 310 MeV, $\theta_{lab} = 5^\circ$ to 40°; measured $\sigma(T_\pi,\theta_{lab})$.]

PACS Numbers: 25.80.Fm

In pion-nucleus scattering, the qualitative (and often quantitative) features of many strong inelastic transitions are well explained within models which take nuclear structure information from data on reactions such as (e,e') and (p,p') data and treat the π-nucleus interaction in the distorted wave impulse approximation.[1] However, this approach significantly underestimates single-charge-exchange (SCX) differential cross sections,[2] and its extension to double-charge-exchange (DCX) reactions fails at Δ_{33} resonance energies.[3] In particular, DCX angular distributions leading to double isobaric analog states (DIAS) at resonance energies have been shown to exhibit forward minima at angles that are, within the simpler models (sequential charge exchange through the free pion-nucleon amplitude), inconsistent with the nuclear size.[4,5] At higher energies, the same reactions exhibit angular distributions that agree with simple calculations.

The anomalous angular distributions have often been interpreted as evidence for interference of the simple DCX amplitude with a second amplitude of similar size. In Ref. 6, it was suggested that this second amplitude arises from whatever reaction mechanism is responsible for the equivalently large differential cross sections observed for (necessarily non-analog) DCX on self-conjugate targets. In Ref. 7, the anomalous position of the minima is attributed to interference with higher-order (two-nucleon, usually called ρ^2) terms in the pion-nucleus optical potential. In that approach, the magnitudes of the isovector and isotensor ρ^2 terms are adjusted to fit the 0° SCX and 5° DCX data, and the resulting parameters provide good predictions of the angular-distribution shapes. The model of Liu[8,9] gives good predictions of both angular distributions and excitation functions by using core-excitation nuclear

wave functions and ρ^2 terms. The latter are obtained from an analysis of π-A elastic scattering data and reflect the effects of true pion absorption.

In this letter, we report six new angular distributions for the reaction $^{18}O(\pi^+,\pi^-)^{18}Ne(gs)$, which, when combined with previous measurements,[4,10] show the change in shape of the angular distributions as a function of energy. This is the most extensive study of DCX on a single nucleus, and identifies the energy regions in which the simple DCX amplitude is adequate to describe the data, and the energy regions in which higher order processes become important.

The measurements were made with the Energetic Pion Channel and Spectrometer (EPICS) at the Clinton P. Anderson Meson Physics Facility (LAMPF). Descriptions of the spectrometer, channel, and the modifications installed for forward-angle DCX measurements have been presented elsewhere.[11] A copper frame with 0.25-mil aluminized mylar windows contained the H_2O ice target which was enriched to 94% isotopic purity $H_2{}^{18}O$. The frame was constructed with a centered horizontal copper bar to enhance cooling of the ice. Physical measurement of the target thickness indicated an areal density of 0.95 ± 0.01 g/cm^2 H_2O, assuming a density of 1.12 g/cm^3. This value agreed well with an areal density obtained by comparing yields for $^1H(\pi^+,\pi^+)$ measured with a CH_2 target (73.68 mg/cm^2) and with the H_2O target, of x_p = 0.93 ± 0.03 g/cm^2 H_2O.

Background muon and electron events were eliminated from pion spectra by a combination of time-of-flight tests, a Freon-12 threshold Cherenkov detector to reject electrons, and a range-nuclear-interaction absorber that was adjusted to identify muon events.[12] No background events under the states of interest were expected from DCX events in the target windows, frame, or contaminants. The Q values for ^{16}O (-28.38 MeV), ^{12}C (-31.96 MeV), and ^{27}Al (-16.38 MeV) are much

more negative than that for ^{18}O (-5.08 MeV). The copper Q values (-7.85 MeV for ^{63}Cu, -3.59 MeV for ^{65}Cu) are similar to that for ^{18}O, but the greater pion energy loss in the copper frame (8.33 MeV) than in the ice (1.32 MeV) removes this background from under the states of interest. (Computer software gates were, however, used to eliminate scattering events occuring in the copper bar.) The data were normalized by measuring yields for $^{1}H(\pi^{+},\pi^{+})$ at $\theta = 40^{o}$ and comparing them to cross sections based on the phase shift fits of Rowe, Saloman, and Landau[13]. Yields measured for $^{1}H(\pi^{+},\pi^{+})$ at $\theta = 20$, 30, and 40^{o} indicated that, within the statistical uncertainty of the yield and uncertainty of the π-p cross sections, the normalization factors are angle independent. The error bars shown in the figures represent the statistical uncertainty of the ^{18}Ne peak areas.

The new $^{18}O(\pi^{+},\pi^{-})^{18}Ne(gs)$ excitation function data are shown in Fig. 1, along with the data from Ref. 4. Where overlap points exist the agreement with previous measurements is, in general, good. The new and old measurements within two MeV of 100, 180, 230, and 292 MeV differ from their means by 1.4 standard deviations.

An excitation function for the $^{18}Ne(2^{+},1.89$ MeV) state is also displayed in Fig. 1. We note that these cross sections are almost independent of energy, except between 130 and 170 MeV, where cross sections are at least a factor of ten smaller, a larger decrease than in the transition to the $^{18}Ne(gs)$ state.

The new ground-state angular distributions are shown in Fig. 2, along with previously measured 164- and 292-MeV data,[4,10] plotted as a function of the momentum transfer, q. The shape of the 230-MeV angular distribution is nearly identical to that of the 292-MeV data, with a broad diffraction minimum at $q = 0.85$ fm^{-1}. The larger-angle data are suggestive of a second maximum a

factor of 20 lower than the 5^{o} datum. At 200 MeV the data are roughly constant for $q > 0.5$ fm^{-1}, and the cross section at the largest angle measured has increased to be only a factor of 10 smaller than the forward-angle values. These features provide a smooth transition in shape between 230 and 180 MeV.

At 180 MeV the minimum is at $q \approx 0.5$ fm^{-1}. The cross sections for $q > 0.5$ MeV are indicative of a relatively large second maximum. The shapes of the angular distribution at 164, 172, and 180 MeV are very similar, and are clearly different from those at higher energies. Below the Δ_{33} resonance, at 120 MeV, the minimum is at a slightly larger momentum transfer. Because of the lower pion flux at lower energies and the limited angular range of the DCX setup ($\theta < 42^{o}$), it was impossible to determine the location of the first minimum of the 100-MeV angular distribution.

In an energy region just above the Δ_{33} resonance (from $200 < T_{\pi} < 230$ MeV) up to at least 292 MeV the ^{18}O angular distribution is normal in the sense that the position of the minimum is consistent with a simple diffractive process. Thus, at these energies the reaction would appear to be dominated by sequential SCX via the intermediate analog state. Figure 3 shows angular distribution calculations for the higher energy region. The curves are from lowest-order calculations with the code PIESDEX[7] using Hartree-Fock[14] (Skyrme-III effective interaction) neutron, proton, and excess neutron densities, and represent sequential charge exchange through the intermediate analog state. The theory correctly predicts angular-distribution shapes at 230 and 292 MeV, and the departure from the dominance of the lowest order reaction mechanism is apparent at 200 and 180 MeV. Not shown are calculations with a ground state density generated from electron scattering parameterizations and a $(d_{5/2})^2$ harmonic oscillator valence neutron density that predict minima at angles a few degrees

larger than the solid curve and similar overall magnitudes. Thus, reasonable variations in the densities do not significantly alter these calculations.

For energies across the Δ_{33} resonance, down to 120 MeV, the angular distributions clearly exhibit forward minima, evidence for additional dynamical effects. The nature of these effects is uncertain, but some possibilities are discussed in Ref. 8 and 15. There is no evidence in our data to indicate whether or not there exists a lower-energy region where the reaction will again agree with lowest-order DCX calculations. Recent measurements[16] of DCX on ^{14}C at 50 MeV would seem to indicate that no such region exists. At 50 MeV, $d\sigma/d\Omega(0^o) = 3.9 \pm 0.5$ μb/sr for the $^{14}C(\pi^+,\pi^-)^{14}O(gs)$ reaction, roughly 20 times that calculated in a sequential charge-exchange calculation in which the intermediate state is the single analog in ^{14}N, and the angular distribution is forward peaked, rather than exhibiting the shallow forward minimum predicted by the calculation.

The shape of the $^{18}O(\pi^+,\pi^-)^{18}Ne(gs)$ 200 MeV angular distribution is similar to the $^{14}C(\pi^+,\pi^-)^{14}O(gs)$ angular distribution[5] at T = 164 MeV, where the cross section is roughly constant for $q > 0.4$ fm^{-1}. The ^{14}C data have been perplexing because all other 164 MeV DCX angular distributions exhibit well-defined, deep, forward minima. It is interesting to speculate that ^{14}C and ^{18}O have similar features shifted by ~40 MeV. This speculation is supported by the shape of the excitation functions, which also exhibit similar shapes, shifted by ~40 MeV with respect to each other. The cause for this shift is unknown.

In conclusion, these new $^{18}O(\pi^+,\pi^-)^{18}Ne(gs)$ data show that the onset of interesting dynamical effects occur over a 30 MeV incident kinetic energy range, which dramatically change the shape of the angular distributions. The completeness of this measurement will hopefully distinguish between varied theoretical approaches to the perplexing DCX problem.

This work has been supported in part by The Robert A. Welch Foundation, The National Science Foundation, and The US Department of Energy.

REFERENCES

a) permanent address: Ben Gurion University of the Negev, Beer-Sheva, Israel.

b) present address: New Mexico State University, Las Cruces, NM 88003.

[1] J. A. Carr, F. Petrovich, D. Halderson, D. B. Holtkamp, W. B. Cottingame, Phys. Rev. C27, 1636 (1983).

[2] A. Doron, J. Alster, A. Erell, S. Gilad, M. A. Moinester, R. A. Anderson, H. W. Baer, J. D. Bowman, M. D. Cooper, F. H. Cverna, C. M. Hoffman, N. S. P. King, M. J. Leitch, J. P. Piffaretti, P. R. Bevington, E. Winkelmann, and C. D. Goodman, Phys. Rev. Lett. 48, 989 (1982); A. Doron, J. Alster, A. Erell, M. A. Moinester, R. A. Anderson, H. W. Baer, J. D. Bowman, M. D. Cooper, F. H. Cverna, C. M. Hoffman, N. S. P. King, M. J. Leitch, J. P. Piffaretti, and C. D. Goodman, Phys. Rev. C26, 189 (1982).

[3] Gerald A. Miller, Phys. Rev. C24, 221 (1981).

[4] S. J. Greene, W. J. Braithwaite, D. B. Holtkamp, W. B. Cottingame, C. F. Moore, G. R. Burleson, G. S. Blanpied, A. J. Viescas, G. H. Daw, C. L. Morris, and H. A. Thiessen, Phys. Rev. C 25, 927 (1982).

[5] Peter A. Seidl, M. D. Brown, Rex R. Kiziah, C. Fred Moore, Helmut Baer, C. L. Morris, G. R. Burleson, W. B. Cottingame, Steven J. Greene, L. C. Bland, R. Gilman and H. T. Fortune, Phys. Rev. C30, 973 (1984).

[6] S. J. Greene, D. B. Holtkamp, W. B. Cottingame, C. F. Moore, G. R. Burleson, C. L. Morris, H. A. Thiessen, and H. T. Fortune, Phys. Rev. C25, 924 (1982); R. Gilman, L. C. Bland, Peter A. Seidl, C. Fred Moore, C. L. Morris, Steven J. Greene, H. T. Fortune, Nuc. Phys. A, (to be published).

[7] Mikkel B. Johnson and E. R. Siciliano, Phys. Rev. C27, 1647 (1983); S. J. reene, C. J. Harvey, P. A. Seidl, R. Gilman, E. R. Siciliano, and Mikkel B. Johnson, Phys. Rev. C (to be published).

[8] L. C. Liu, Phys. Rev. C27, 1611 (1983).

[9] Kamal K. Seth, M. Kaletka, S. Iversen, A. Saha, D. Barlow, D. Smith, and L. C. Liu, Phys. Rev. Lett. 52, 894 (1984).

[10] Kamal K. Seth, S. Iversen, H. Nann, M. Kaletka, J. Hird, and H. A. Thiessen, Phys. Rev. Lett. 43, 1574 (1979).

[11] H. A. Thiessen, J. C. Kallne, J. F. Amann, R. J. Peterson, S. J. Greene, S. L. Verbeck, G. R. Burleson, S. G. Iverson, A. W. Obst, Kamal K. Seth, C. F. Moore, J. E. Bolger, W. J. Braithwaite, D. C. Slater and C. L. Morris, Los Alamos Scientific Laboratory Report No. LA-6663-MS, (1977); S. J. Greene, W. J. Braithwaite, D. B. Holtkamp, W. B. Cottingame, C. F. Moore, C. L. Morris, H. A. Thiessen, G. R. Burleson, and G. S. Blanpied, Phys. Lett. 88B, 62 (1979); G. R. Burleson, G. S. Blanpied, G. H. Daw, A. J. Viescas, C. L. Morris, H. A. Thiessen, S. J. Greene, W. J. Braithwaite, W. B. Cottingame, D. B. Holtkamp, I. B. Moore, and C. F. Moore, Phys. Rev. C22, 1180 (1980); S. J. Greene, PhD thesis, The University of Texas at Austin, Los Alamos National Laboratory Report No. LA-8891-T, (1981).

[12] C. L. Morris, J. F. Amann, R. L. Boudrie, N. Tanaka, S. J. Seestrom-Morris, L. C. Bland, P. A. Seidl, and R. Kiziah, (to be published).

[13] Glenn Rowe, Martin Salomon and Rubin H. Landau, Phys. Rev. C 18, 584 (1978).

[14] M. Beiner, H. Flocard, Nguyen Van Giai, and P. Quentin, Nucl. Phys. A238, 29 (1975).

[15] Mikkel B. Johnson, E. R. Siciliano, H. Toki, and A. Wirzba, Phys. Rev. Lett. 52, 593 (1984); E. Oset, D. Strottman, M. J. Vicente-Vacas, and Ma Wei-Hsing, Nuc. Phys. A408, 461 (1983); T. Karapiperis, M. Kobayashi, and M. Hirata, Phys. Lett. 144B, 23 (1984); Pervez Hoodbhoy, Roger A. Freedman, Gerald A. Miller, and Ernest M. Henley, Phys. Rev. C27, 277 (1983).

[16] M. J. Leitch, E. Piasetzky, H. W. Baer, J. D. Bowman, R. L. Burman, B. J. Dropesky, P. A. M. Gram, F. Irom, D. Roberts, G. A. Rebka, J. N. Knudson, J. R. Comfort, V. A. Pinnick, D. H. Wright, and S. A. Wood, submitted to Phys. Rev. Lett. (1984) and Los Alamos National Laboratory Report LA-UR 84-2754; I. Navon, M. J. Leitch, D. A. Bryman, T. Numao, P. Schlatter, G. Azuelos, R. Poutissou, R. A. Burnham, M. Hasinoff, J. M. Poutissou, J. A. Macdonald, J. E. Spuller, C. K. Hargrove, H. Mes, M. Blecher, K. Gotow, M. Moinester, H. Baer, Phys. Rev. Lett. 52, 105 (1984).

FIGURE CAPTIONS

Fig. 1. Center-of-mass cross sections ($\theta_{lab} = 5^{o}$) for $^{18}O(\pi^{+},\pi^{-})^{18}Ne(gs)$ (crosses from this work and circles from Ref. 4) and $^{18}O(\pi^{+},\pi^{-})^{18}Ne(2^{+}, 1.89\ MeV)$ are plotted versus the pion energy in the lab frame. The $^{18}Ne(2^{+}_{1})$ data from both Ref. 4 and from this work are represented by squares.

Fig. 2. Center-of-mass cross sections for $^{18}O(\pi^{+},\pi^{-})^{18}Ne(0\ MeV)$, are plotted versus the momentum transfer, q. The incident energies in MeV are indicated on the graph. Data for $q = 0.70$ and $1.03\ fm^{-1}$ ($\theta = 30^{o}$ and 45^{o}) at $T_{\pi} = 164$ MeV are from Ref. 10. The datum for $T_{\pi} = 292$ MeV, $q = 1.40$ is from this work, and all remaining data for $T_{\pi} = 164$ and 292 MeV are from Ref. 4.

Fig. 3. Center-of-mass cross sections for $^{18}O(\pi^{+},\pi^{-})^{18}Ne(gs)$ are compared to lowest order PIESDEX calculations.

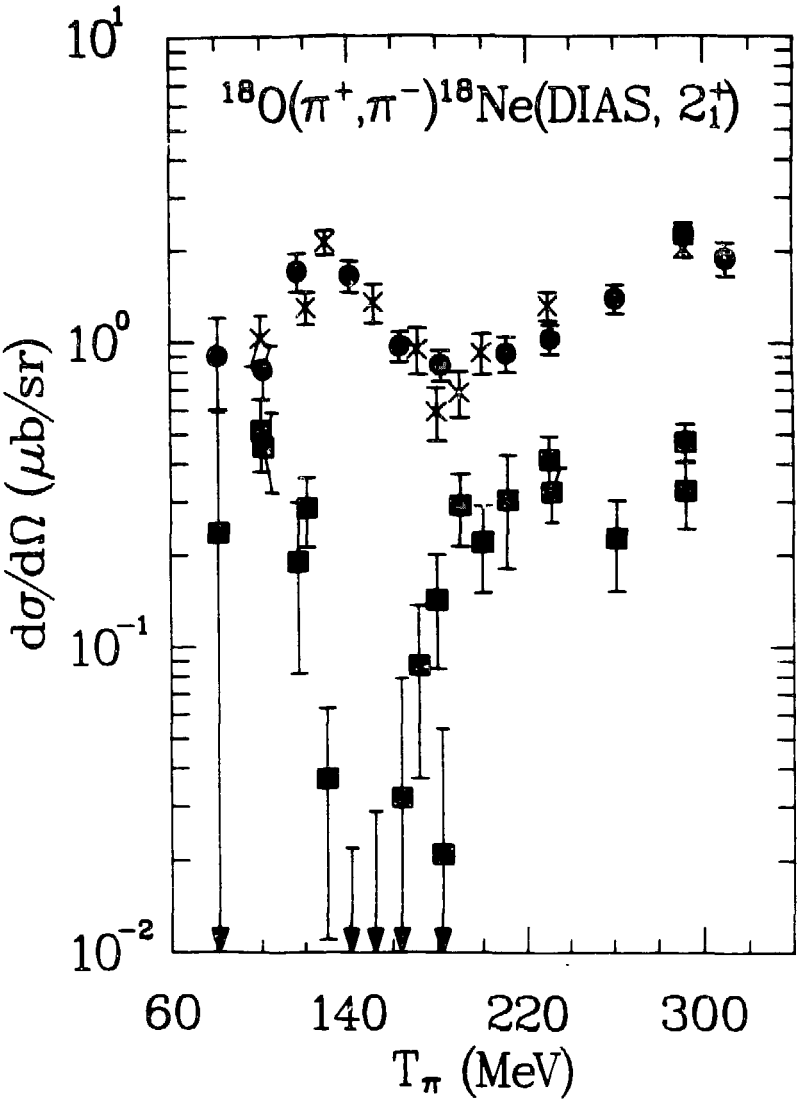
$^{18}O(\pi^+,\pi^-)^{18}Ne(DIAS, 2_1^+)$
$d\sigma/d\Omega$ (μb/sr)
10^1
10^0
10^{-1}
10^{-2}
60
140
220
300
T_π (MeV)

Fig. 1

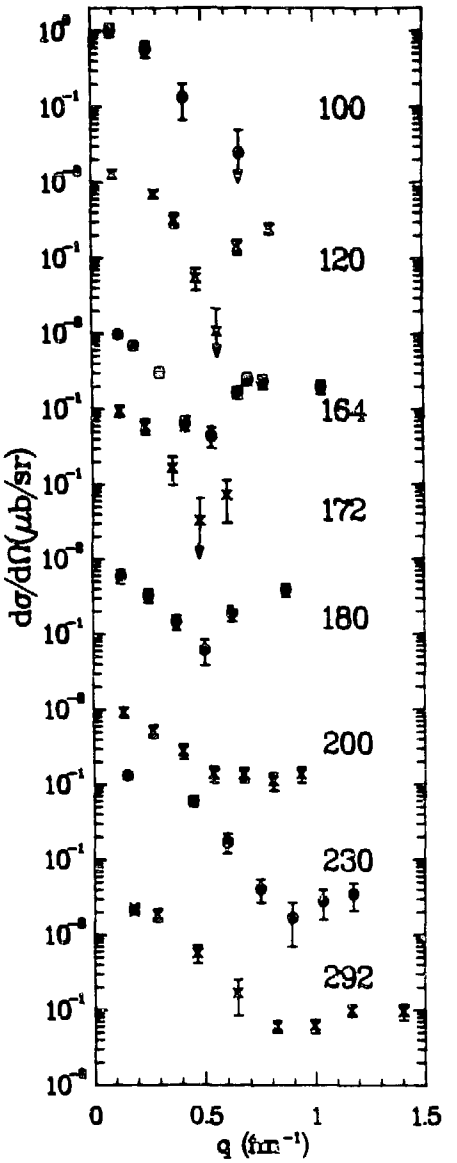

Fig. 2

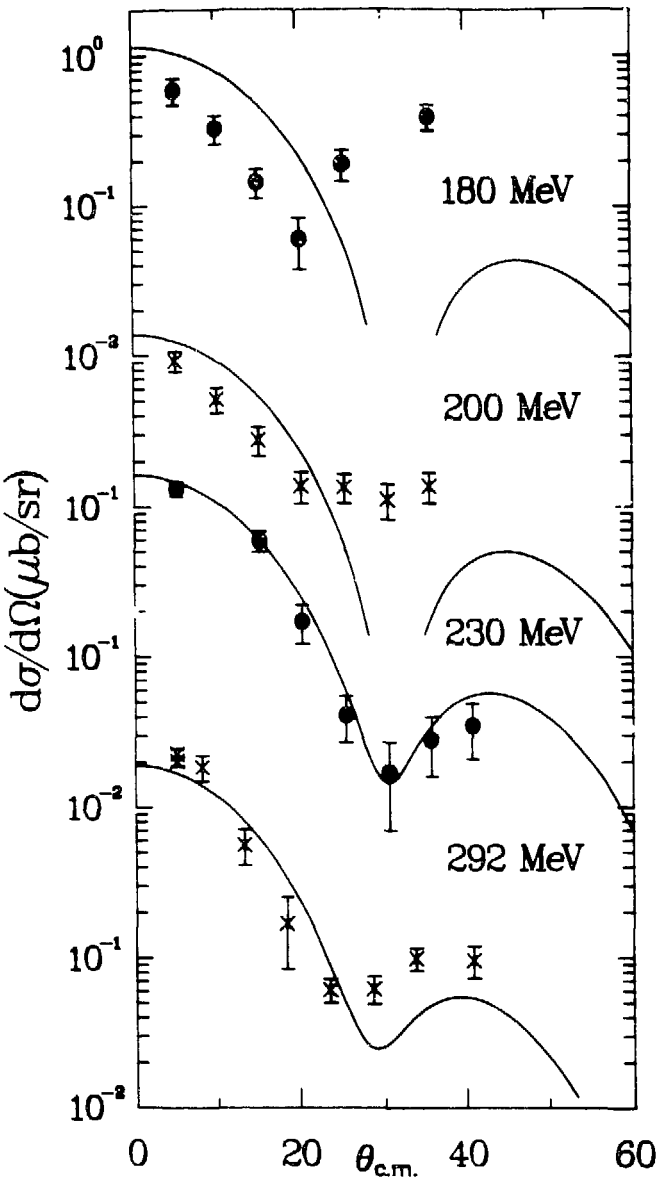

Fig. 3

APPENDIX C

Dissertation Papers

"Pion Double Charge Exchange on T = 1 Nuclei," Peter A. Seidl, Mark D. Brown, Rex R. Kiziah, C. Fred Moore, Helmut Baer, C. L. Morris, G. R. Burleson, W. B. Cottingame, Steven J. Greene, L. C. Bland, R. Gilman, and H. T. Fortune, Phys. Rev. C30, 973 (1984).

"$^{13}C(\pi^+,\pi^-)^{13}O$ Near the Δ_{33} Resonance," Peter A. Seidl, Mark D. Brown, Rex R. Kiziah, C. Fred Moore, Helmut Baer, Christopher L. Morris, G. R. Burleson, W. B. Cottingame, Steven J. Greene, L. C. Bland, R. Gilman, and H. T. Fortune, Phys. Rev. C30, 1076 (1984).

"Observation of Analog and Non-Analog Transitions in the Reaction $^{56}Fe(\pi^+,\pi^-)^{56}Ni$," Peter A. Seidl, Rex R. Kiziah, Mark D. Brown, C. Fred Moore, C. L. Morris, H. Baer, Steven J. Greene, G. R. Burleson, W. B. Cottingame, and H. T. Fortune, Physical Review Letters 50, 1106 (1983).

ACKNOWLEDGEMENTS

Much thanks goes to my advisor, C. Fred Moore, for his support during these past years. To Ron Gilman and Rex Kiziah, who not only gave much help during and after the experiment, but also provided encouragement and stimulating discussions, I express much gratitude.

The experiment would not have been a success without the assistance of Richard Boudrie and the MP-10 staff who have made EPICS such a productive nuclear physics facility. To the collaborators on Experiment 558: Mark Brown, Rex Kiziah, C. Fred Moore, Helmut Baer, Chris Morris, George Burleson, Bill Cottingame, Steve Greene, Les Bland, Ron Gilman, and H. Terry Fortune, I express my thanks. The construction of the new target cells by Joe Van Dyke, and the careful packing of the ^{14}C target by Helmut Baer, made the ^{14}C measurements safe.

I thank H. Terry Fortune and Chris Morris for the fruitful discussions concerning the interpretation of DCX. The calculations of section A of Chapter V were made possible by Mikkel Johnson and Ed Siciliano, who have always made time to answer any questions. I thank Lon Chang Liu for providing the calculations of section B of Chapter V.

I thank Chris Morris and John Zumbro for having carefully read the dissertation.

REFERENCES

[Am-79] J. F. Amann, R. L. Boudrie, H. A. Thiessen, C. L. Morris, and L. E. Smith, IEEE Transactions in Nuclear Science NS-26, 4389 (1979).

[Am-80] R. D. Amado, J.-P. Dedonder, and F. Lenz, Phys. Rev. C21, 647 (1980).

[At-81] L. G. Atencio, J. F. Amann, R. L. Boudrie, C. L. Morris, Nucl. Inst. Meth. 187, 381 (1981).

[Ba-80] Helmut W. Baer, J. D. Bowman, M. D. Cooper, F. H. Cverna, C. M. Hoffman, Mikkel B. Johnson, N. S. P. King, J. Piffaretti, E. R. Siciliano, J. Alster, A. Doron, S. Gilad, M. Moinester, P. R. Bevington, E. Winkelmann, Phys. Rev. Lett. 45, 982 (1980).

[Be-75] M. Beiner, H. Flocard, N. Van Giai, and P. Quentin, Nucl. Phys. A238, 29 (1975).

[Bl-83] L. C. Bland, R. Gilman, M. Carchidi, K. Dhuga, C. L. Morris, H. T. Fortune, S. J. Greene, P. A. Seidl and C. Fred Moore, Phys. Lett. 128B, 157 (1983).

[Bo-79] R. L. Boudrie, J. F. Amann, C. L. Morris, H. A. Thiessen, and L. E. Smith, IEEE Transactions in Nuclear Science NS - 26 (1979).

[Bu-78] R. L. Burman, M. P. Baker, M. D. Cooper, R. H. Heffner, D. M. Lee, R. P. Redwine, J. E. Spencer, T. Marks, D. J. Marlbrough, B. M. Preedom, R. J. Holt, and B. Zeidman, Phys. Rev. C17, 1774 (1978).

[Bu-80] G. R. Burleson, G. S. Blanpied, G. H. Daw, A. J. Viescas, C. L. Morris, H. A. Theissen, S. J. Greene, W. J. Braithwaite, W. B. Cottingame, D. B. Holtkamp, I. B. Moore, and C. F. Moore, Phys. Rev. C22, 1180 (1980).

[Bu-n.d.] G. R. Burleson, and J. F. Amann, computer program CROSS (unpublished) n.d.

[Ca-73] J. R. Carter, D. V. Bugg, and A. A. Carter, Nucl. Phys. B58, 378 (1973).

[Ch-69] D. T. Chivers, E. M. Rimmer, B. W. Allardyce, R. C. Witcomb, J. J. Domingo, and N. W. Tanner, Nucl. Phys. A126, 129 (1969).

[Co-65] S. Cohen, and D. Kurath, Nucl. Phys. 73, 1 (1965).

[Co-72] D. R. F. Cochran, P. N. Dean, P. A. M. Gram, E. A. Knapp, E. R. Martin, D. E. Nagle, R. B. Perkins, W. J. Schlaer, H. A. Thiessen, and E. D. Theriot, Phys. Rev. D6, 3085 (1972).

[Co-78] P. Couvert, G. Bruge, R. Beurtey, A. Boudard, A. Chaumeaux, M. Garcon, D. Garreta, P. C. Gugelot, G. A. Moss, S. Platchkov, J. P. Tabet, Y. Terrien, J. Thirion, L. Bimbot, Y. Le Bornec, and B. Tatischeff, Phys. Rev. Lett. 41, 530 (1978).

[de-74] C. W. de Jager, H. de Vries, and C. de Vries, At. Data Nucl. Data Tables 14, 479 (1974).

[Do-82] A. Doron, J. Alster, A. Erell, M. A. Moinester, R. A. Anderson, H. W. Baer, J. D. Bowman, M. D. Cooper, F. H. Cverna, C. M. Hoffman, N. S. P. King, M. J. Leitch, J. P. Piffaretti, and C. D. Goodman, Phys. Rev. C26, 189 (1982).

[Ei-74] R. A. Eisenstein and G. A. Miller, Computer Phys. Comm. 8, 130 (1974).

[Ei-80] J. Eisenberg and D. Koltun, Theory of Meson Interactions with Nuclei, (John Wiley and Sons, New York, 1980).

[Ev-72] D. Evers, W. Assmann, K. Rudolph and S. J. Skorka, Nucl. Phys. A198, 268 (1972).

[Fo-82] H. T. Fortune, and G. S. Stephans, Phys. Rev. C25, 1 (1982).

[Gi-83] R. Gilman, et. al., EPICS experiment # 780, (1983).

[Gi-84a] R. Gilman, H. T. Fortune, Kalvir S. Dhuga, Peter H. Kutt, L. C. Bland, Rex R. Kiziah, C. Fred Moore, Peter A. Seidl, C. L. Morris, and W. B. Cottingame, Phys. Rev. C29, 2395 (1984).

[Gi-84b] R. Gilman, L. C. Bland, Peter A. Seidl, C. Fred Moore, C. L. Morris, Steven J. Greene, H. T. Fortune, submitted to Phys. Rev. C (1984).

[Gr-79] S. J. Greene, W. J. Braithwaite, D. B. Holtkamp, W. B. Cottingame, C. F. Moore, C. L. Morris, H. A. Theissen, G. R. Burleson, and G. S. Blanpied, Phys. Lett. 88B, 62 (1979).

[Gr-81] S. J. Greene, PhD thesis, The University of Texas at Austin (1981); and Los Alamos National Laboratory Report # LA-8891-T, (1981).

[Gr-82a] S. J. Greene, W. J. Braithewaite, D. B. Holtkamp, W. B. Cottingame, C. F. Moore, G. R. Burleson, G. S. Blanpied, A. J. Viescas, G. H. Daw, C. L. Morris, and H. A. Theissen, Phys. Rev. C 25, 927 (1982).

[Gr-82b] S. J. Greene, D. B. Holtkamp, W. B. Cottingame, C. F. Moore, G. R. Burleson, C. L. Morris, H. A. Thiessen, and H. T. Fortune, Phys. Rev. C25, 924 (1982);

[Gr-83] S. J. Greene, W. B. Cottingame, G. R. Burleson, L. C. Bland, R. Gilman, H. T. Fortune, C. L. Morris, D. B. Holtkamp, and C. Fred Moore, Phys. Rev. C27, 2375 (1983).

[Gr-84] S. J. Greene, C. J. Harvey, P. A. Seidl, R. Gilman, E. R. Siciliano, and M. B. Johnson, (accepted by Phys. Rev. C).

[Ha-84] Carol J. Harvey, H. W. Baer, J. A. Johnstone, C. L. Morris, S. J. Seestrom-Morris, D. Dehnhard, D. B. Holtkamp, and S. J. Greene, (submitted to Phys. Rev. C).

[In-78] Q. Ingram, E. Boschitz, L. Pflug, J. Zichy, J. P. Albanese, and J. Arvieux, Phys. Lett. 76B, 173 (1978).

[Ir-83] F. Irom, J. R. Comfort, R. Jeppesen, J. J. Kraushaar, R. A. Ristinen, W. Tew, J. L. Ullmann, H. W. Baer, J. D. Bowman, M. D. Cooper, E. Piasetzky, U. Sennhauser, A. Erell, M. A. Moinester, E. R. Siciliano, Phys. Rev. C28, 2565 (1983).

[Ja-75] F. James and M. Roos, Computer Phys. Comm. 10, 343 (1975).

[Jo-80] M. B. Johnson, Phys. Rev. C22, 192 (1980).

[Jo-83a] M. B. Johnson and E. R. Siciliano, Phys. Rev. C27, 730 (1983).

[Jo-83b] M. B. Johnson and E. R. Siciliano, Phys. Rev. C27, 1647 (1983).

[Jo-84] M. B. Johnson, E. R. Siciliano, H. Toki, and A. Wirzba, Phys. Rev. Lett. 52, 593 (1984).

[Ka-83] M. O. Kaletka, PhD thesis, Northwestern University; and Los Alamos National Laboratory Report # LA-9947-T (1983).

[Le-84] M. J. Leitch, E. Piasetzky, H. W. Baer, J. D. Bowman, R. L. Burman, B. J. Dropesky, P. A. M. Gram, F. Irom, D. Roberts, G. A. Rebka, J. N. Knudson, J. R. Comfort, V. A. Pinnick, D. H. Wright, and S. A. Wood, submitted to Phys. Rev. Lett. (1984) and Los Alamos National Laboratory Report LA-UR 84-2754.

[Li-81] L. C. Liu, Phys. Rev. C23, 814 (1981).

[Li-83] L. C. Liu, Phys. Rev. C27, 1611 (1983).

[Li-84] L. C. Liu, private communication, (1984).

[Mi-81] G. A. Miller, Phys. Rev. C24, 221 (1981).

[Mi-84] Gerald A. Miller, "Searching for Six-Quark Cluster Components of Nuclear Wave Functions with the Pion-Nucleus Double-Charge-Exchange Reaction", University of Washington, unpublished, (1984).

[Mo-80] C. L. Morris et al., Phys. Rev. Lett. 45, 1233 (1980).

[Mo-82a] C. L. Morris, H. T. Fortune, L. C. Bland, R. Gilman, S. J. Greene, W. B. Cottingame, D. B. Holtkamp, G. R. Burleson and C. Fred Moore, Phys. Rev. C 25, 3218 (1982).

[Mo-82b] C. L. Morris, Nucl. Inst. Meth. 196, 263 (1982).

[Mo-83] see, for example, C. L. Morris et. al., Phys. Rev. C28, 2165 (1983); J. A. Carr et. al., Phys. Rev. C27, 1636 (1983); S. J. Seestrom-Morris et. al., Phys. Rev. C26, 594 (1982); Kenneth G. Boyer et. al., Phys. Rev. C24, 598 (1981); Christopher L. Morris et. al., Phys. Rev. C24, 231 (1981); D. F. Geesaman et. al., Phys. Rev. C23, 2635 (1981); S. Iversen et. al., Phys. Lett. 82B, 51 (1979).

[Mo-84] C. L. Morris, J. F. Amann, R. L. Boudrie, N. Tanaka, S. J. Seestrom-Morris, L. C. Bland, P. A. Seidl, R. Kiziah, (to be published).

[MP-80] "LAMPF Users Handbook", Clinton P. Anderson Meson Physics Facility, MP-DO-1-UHB (Rev.), (1980).

[Na-74] H. Nann and W. Benenson, Phys. Rev. C 10, 1880 (1974).

[Ne-72] J. W. Negele, and D. Vautherin, Phys. Rev. C5, 1472; C11, 1031 (1975).

[Ol-80] C. Olmer, D. F. Geesaman, B. Zeidman, S. Chakravarti, T.-S. I. Lee, R. L. Boudrie, R. H. Siemssen, J. F. Amann, C. L. Morris, H. A. Theissen, G. R. Burleson, M. J. Devereux, R. E. Segal, and L. W. Swensen, Phys. Rev. C21, 254 (1980).

[Ra-83] W. D. M. Rae, A. Etchegoyen, N. S. Godwin and B. A. Brown, OXBASH, The Oxford-Buenos Aires Shell Model Code, 1983, (unpublished).

[Ro-78] G. Rowe, M. Salomon and R. H. Landau, Phys. Rev. C 18, 584 (1978).

[Se-80] K. K. Seth, in "Intermediate-Energy Nuclear Chemistry Workshop", Los Alamos National Laboratory, Report no. LA-8835-C (1980).

[Se-81] S. J. Seestrom-Morris, PhD dissertation, University of Minnesota (1981); Los Alamos National Laboratory Report # LA-8916-T.

[Se-84] P. A. Seidl, R. R. Kiziah, M. K. Brown, C. Fred Moore, C. L. Morris, H. Baer, S. J. Greene, G. R. Burleson, W. B. Cottingame, L. C. Bland, R. Gilman and H. T. Fortune, Phys. Rev. C30, 973 (1984).

[Sen-83] U. Sennhauser, E. Piasetzky, H. W. Baer, J. D. Bowman, M. D. Cooper, H. S. Matis, H. J. Ziock, J. Alster, A. Erell, M. A. Moinester, and F. Irom, Phys. Rev. Lett. 51, 1324 (1983).

[Set-84] Kamal K. Seth, M. Kaletka, S. Iversen, A. Saha, D. Barlow, D. Smith, and L. C. Liu, Phys. Rev. Lett. 52, 894 (1984).

[Sl-76] D. C. Slater, Los Alamos National Laboratory, unpublished.

[Th-70] H. A. Theissen et al., Los Alamos Scientific Laboratory Report No. LA-4534-MS (1970); H. A. Theissen, J. C. Kallne, J. F. Amann, R. J. Peterson, S. J. Greene, S. L. Verbeck, G. R. Burleson, S. G. Iverson, A. W. Obst, K. K. Seth, C. F.

Moore, J. E. Bolger, W. J. Braithewaite, D. C. Slater and C. L. Morris, Los Alamos Scientific Laboratory Report No. LA-6663-MS, 1977 (unpublished).

[Wa-79] J. B. Walker, and G. A. Rebka, Jr., Los Alamos National Laboratory, Report # LA-7731-MS (1979).

☆ U.S. GOVERNMENT PRINTING OFFICE:1985—576-034 / 20022